

STAVEBNÍ OBZOR

ČÍSLO 3/2016

Obsah čísla:

<p>THE EFFECT OF DEGRADATION PROCESSES ON THE SERVICEABILITY OF BUILDING MATERIALS OF HISTORIC BUILDINGS <i>Witzany Jiří, Čejka Tomáš, Kroftová Klára, Šmidtová Markéta</i></p>
<p>IN-SITU TEST EXPERIMENTAL RESEARCH ON LEAKAGE OF LARGE DIAMETER PRE-STRESSED CONCRETE CYLINDER PIPE (PCCP) <i>Jianjun Luo, Liping Gao</i></p>
<p>THREE-PARAMETER CREEP DAMAGE CONSTITUTIVE MODEL AND ITS APPLICATION IN HYDRAULIC TUNNELLING <i>Luo Gang, Chen Liang</i></p>
<p>OPTIMIZATION OF THE TEMPERATURE CONTROL SCHEME FOR ROLLER COMPACTED CONCRETE DAMS BASED ON FINITE ELEMENT AND SENSITIVITY ANALYSIS METHODS <i>Huawei Zhou, Yihong Zhou, Chunju Zhao, Zhipeng Liang</i></p>
<p>GROUTING METHODS FOR THE REHABILITATION AND REINFORCEMENT OF MASONRY STRUCTURES DAMAGED BY CRACKS <i>Čejka Tomáš, Zigler Radek, Kroftová Klára, Šmidtová Markéta</i></p>
<p>COMPARATIVE ASSESSMENT OF RICE HUSK ASH, POWDERED GLASS AND CEMENT AS LATERITIC SOIL STABILIZERS <i>Adebisi Ridwan, Taiwo Kanmodi and Olufikayo Aderinlewo</i></p>
<p>FINITE ELEMENT MODELLING AND ANALYSIS OF CONCRETE CONFINED BY STIRRUPS IN SQUARE RC COLUMNS <i>Xiang Zeng</i></p>
<p>RESEARCH ON DYNAMIC SIMILARITY MODEL TEST OF DAMAGE DETECTION FOR TRANSMISSION TOWER <i>Zhou Ling, Li Ying-tao, Yang Chao-shan, Deng Zhi-ping, Chen Jin</i></p>
<p>EXPERIMENTAL RESEARCH INTO DYNAMIC PROPERTIES OF MASONRY BARREL VAULTS NON-REINFORCED AND REINFORCED WITH CARBON COMPOSITE STRIPS <i>Zigler Radek, Witzany Jiří, Makovička Daniel, Urushadze Shota, Pospíšil Stanislav, Kubát Jan and Kroftová Klára</i></p>

THE EFFECT OF DEGRADATION PROCESSES ON THE SERVICEABILITY OF BUILDING MATERIALS OF HISTORIC BUILDINGS

Witzany Jiří¹, Čejka Tomáš¹, Kroftová Klára², Markéta Šmidtová¹

¹ CTU in Prague, Faculty of Civil Engineering, Department of Building Structures, Prague, Thákurova 7, Czech Republic; witzany@fsv.cvut.cz, cejka@fsv.cvut.cz, smidmar@fsv.cvut.cz

² CTU in Prague, Faculty of Civil Engineering, Department of Architecture, Prague, Thákurova 7, Czech Republic; klara.kroftova@fsv.cvut.cz

ABSTRACT

The article presents an analysis of degradation processes and partial results of an experimental research into materials and structures exposed to the effects of external environments with an emphasis on the effects of moisture and chemical degradation processes on major mechanical properties of sandstone.

KEYWORDS

degradation process, moisture, sandstone, mechanical properties

INTRODUCTION

An inseparable part of the restoration of historic and heritage buildings is the assessment of residual service life of materials and structures. The starting point for the determination of the presumed service life and durability of building materials and structures, or residual service life of materials and structures of historic buildings is study of degradation processes and effects and conditions which cause them. Based on the study of degradation processes and their causes, reliable preventive measures can be designed. The growing aggressiveness of the external environment highlights the importance of degradation processes, preceding the appearance of failures of buildings and the loss of their serviceability.

Degradation, according to ČSN EN 1990 and ČSN ISO 13822 standards, is a process affecting serviceability, including reliability, over time due to

- naturally existing chemical, physical and biological effects
- repetitive loading which can cause fatigue
- common or adverse environmental effects
- wear caused by the type of utilisation
- incorrect operation or maintenance.

EFFECTS AND IMPACTS CAUSING DEGRADATION PROCESSES

Environmental effects and impacts which cause degradation processes can be superposed only with difficulty as these phenomena change the major properties of materials and structures over time. Study of the relationship of monitored material parameters to a certain time-variable external effect requires the observance of the stability of all the other characteristics of the respective external environment. This allows obtaining a theoretical image of the influence of this effect on the behaviour

of a material or structure, but not a real image when the other effects co-act simultaneously and mutually interact with each other. This fact must be kept in mind when applying various laboratory measurements and tests which usually require rather complicated interpretation and they frequently have only limited usage.

The assessment of the time duration of a degradation phenomenon requires the determination of its start and finish. A greater part of degradation processes running in nature reach a state of equilibrium after some time, i.e. a state when the degradation process has stopped running – the “sources” of on-going processes have been exhausted, external conditions have changed, etc. – without reaching the complete degradation of the respective member, material or building as a whole, while the other degradation processes keep running until the complete degradation (destruction) of the “work” [1].

In processes (phenomena) resulting in permanent degradation, the state of equilibrium can be established. In phenomena causing transient degradation, on the contrary, the state of equilibrium can only be established with difficulty as the magnitude of degradation due to exposure to the atmosphere with permanently on-going changes in the intensity of climatic factors is constantly changing.

The establishment of the state of equilibrium for phenomena with transient degradation requires the assessment of the state of equilibrium as the state when the magnitude of degradation fluctuates around a roughly constant value. This state is called the state of dynamic equilibrium.

Due to the effect of climatic factors, structures and materials are exposed to degradation which, in terms of the recovery ability, can be either of permanent (irreversible), temporary (transient) or reversible nature [2].

The degradation of structures or materials considered as permanent degradation is such degradation which does not fade away even if the magnitude of the decisive external factor which induced it has fallen below the critical value and the external critical factor has stopped inducing further degradation.

Irreversible changes in the properties of building materials are almost exclusively connected with long-term phenomena depending on the length of their duration, and in their consequence e.g. after a change of external parameters back to the starting, initial state, the building material does not regain the original, initial properties, or the parameter values describing these properties after some time.

The degradation considered as transient degradation is such degradation that will fade away as soon as the magnitude of the decisive external factor has fallen below the critical value. It will fade away either spontaneously or due to the action of another external factor or by the co-action of several other external factors, without the addition of any energy or without the effect of any other intervention. These are relaxation degradation phenomena in which induced degradation fades away as soon as the external factor stops inducing the degradation, i.e. with a change in the weather or climate (external) conditions.

The degradation of structures and materials considered reversible degradation is such degradation which can fade away as soon as the magnitude of the decisive external factor has fallen below the critical value, but only due to some energy which will be added to the exposed material or structure (not due to the effect of the energy of some other external or several other external factors), or if some intervention has been performed on the exposed structure or material.

Reversible changes in the properties of building materials are almost exclusively connected with short-term processes (warming, cooling, wetting, drying) and the dependence of property changes of e.g. a building material on the monitored parameter runs following a hysteresis loop of closed shape.

Naturally exposed structures or materials may simultaneously exhibit degradation of different types in terms of its regeneration ability due to the effect of several or even one external factor. The most common case in the simultaneous appearance of permanent and transient degradation.

By its nature, each degradation phenomenon is a complex set of series of partial phenomena and processes which in their total make up the substance of the degradation process. For example, degradation caused by water vapour sorption is a phenomenon whose substances in different climate conditions or in different materials are various partial phenomena with different relevance such as diffusion, adsorption, capillary condensation, chemisorption, molecular flow, capillary elevation, swelling, etc. Therefore, the explanation of various degradation processes, their mechanisms and velocity is very difficult and often requires a long-term monitoring.

Practical experience gained from existing buildings shows that, together with reliable diagnostic methods used for building surveys, the characteristics of materials and structures must be investigated as changing variables, time- and environment-dependent. The knowledge of time-dependent behaviour of materials is the issue of reliability and durability of buildings.

MECHANISMS OF DEGRADATION PROCESSES

The mechanisms of **degradation processes**, their intensity and the velocity of their time pattern are related to the material structure, particularly the pore system, surface areas, etc. [2]. These parameters affect, in a decisive way, mainly transport processes in materials, primarily the moisture content (in the liquid as well as gaseous phase), which is the principal carrier of various aggressive substances transported into the internal structure of building materials and structures, which, as a rule, change their chemical, physical and mechanical characteristics due to their action. In this perspective, it is obvious that the **properties of building materials** should be understood as **time-variable parameters** dependent on the environment. At the same time, the structural non-homogeneity of the vast majority of building materials characterised by a **multi-phase structure and discontinuous changes in properties** at the interphase of individual phases must be respected.

The research to-date manifests that the study of **structural parameters** in particular can be the starting point for finding accurate models of the behaviour and properties of building materials, or functions describing the development and dependence of these properties on changes in external conditions. The main agents of the external environment include, above all, **temperature and moisture effects, radiation, chemical and biological effects**.

Part of the design and restoration of buildings in terms of reliability and durability is the analysis of the **mutual interaction of the external and internal environment** with the "structure (building) and its parts", **mutual interaction of individual parts of the "building", materials** and layers at the interface of their mutual contact and the design of preventive measures against undesirable consequences of this interaction. Insufficient and inaccurate analysis of the consequences of mutual interaction of parts of a building, together with the underestimation of the significance of cyclic non-force temperature and moisture effects, are a frequent cause of mechanical damage and degradation of building materials before and after the restoration of the building.

The non-homogeneity of the majority of building materials, dispersion of their physical and mechanical, chemical and mineralogical properties, non-constant temperature and moisture pattern over the member's cross section, different dilatometric characteristics of individual layers in multi-layer members, non-sliding mounting of a member in the structure and mutual interaction of members bound within a certain (e.g. load-bearing) system are the causes of internal stresses. The upper or the lower temperature or moisture limit defining, in a simplified way, the range of both effects which do not have a substantial influence on the mechanical or other physical properties varies for different groups of building materials.

Temperature and moisture have a decisive influence on major characteristics of building materials, e.g. concrete, in the phase of their formation and in relation to the physical and chemical reactions and processes running in this phase.

CHEMICAL DEGRADATION PROCESSES

An extensive group of degradation processes are chemical degradation processes accompanied by elevated moisture contents of building materials and structures, mainly historic buildings with ineffective or non-functional damp-proofing systems. Chemical corrosion of building materials is a process or a series of processes during which the action of aggressive environments produces a chemical reaction leading to the decrease in major physical and mechanical properties of materials below values necessary for their serviceability.

Chemical degradation processes are characterised by a change in the pore system due to chemical reactions of dissolved salts with building material components, mainly binders. Chemical degradation processes are caused, above all, by the reaction of chemically less stable components of building materials with solutions of weak acids, etc. Chemical degradation processes, the formation of salts, etc. affect **dilatometric** and some other significant properties (porosity, hygroscopicity, water absorption, modulus of elasticity, strength, electrical conductivity, electric potential, etc.). An inseparable part and condition of chemical degradation processes is moisture which, in most cases, is the “carrier” of stable solutions of acids, freely dissociated gases, the condition for the growth and production of metabolisms of microorganisms, etc.

In a general case, in terms of transport phenomena, the interaction pattern between solid mater and a liquid can be, in a simplified way, divided into the following phases:

- a) transport of effective components to the phase interface,
- b) reaction at the phase interface,
- c) transport of products from the phase interface.

In the case of building materials, it is also necessary to take into consideration the fact that a porous material is involved. For phases a) and b), the mass transport through the pore system must be also considered. Furthermore, the dissimilarity of the acting medium and hence the dissimilarity of on-going chemical reactions must be taken into account.

DEGRADATION PROCESSES – SEDIMENTARY ROCKS

The most commonly used sedimentary rocks – stone types – for masonry structures – strip foundations, walls, pillars and vaults – are arenaceous marl, sandstone and limestone. Experimental research [3, 4] has manifested the severe effect of moisture, the mineralogical composition and porosity (number, distribution and type of pores) on the intensity of chemical degradation processes and their effect on the mechanical properties of rocks.

Since the beginning of the 15th century, **sandstone** has belonged to the main building materials. The milestone in using arenaceous marl is the period of the end of the 14th and the start of the 15th century, when arenaceous marl was gradually replaced with sandstone. The obvious reason was higher resistance of sandstone to weathering. The collective term – building sandstone – includes several rock types of sedimentary origin, non-identical chemical composition, age and physical characteristics (water absorption, porosity, frost resistance). They are mostly quartz, fine-grained, medium to coarse-grained sandstones of all categories with grading from 0.5 to 2 mm (arkoses with increased contents of clays and kaolinite binder are also present). The highest-quality sandstones in our territory are sandstones quarried in the Božanov locality (compressive strength of 63 MPa, water absorption of 9.2%, 15.5% porosity), which are used for the reconstruction of prominent historic buildings. The specific cause of serious failures of sandstone is the swelling of clay minerals (kaolite, montmorillonite) where the percentage of clays in some types of sandstone is 10 to 25%, in arkoses of up to 75 % [5, 6].

The major physical characteristic which significantly determines the successive time pattern of degradation processes is the porosity of building materials, which changes over time and affects their water absorption.

Building materials and thus whole structures possess some infiltration capacity. Clastic sediments – sandstones have very favourable conditions for infiltration. **Sandstones** differ by their

grain size (coarse-grained, fine-grained), the size and distribution of pores (from macropores of 10^{-7} to micropores of 10^{-9}) and are **non-homogenous by their microstructure**.

Tab 1. Comparison of water absorption of sandstones from original localities and building blocks from Charles Bridge

	Water absorption w_t [%]	Water absorption w_t [%]
Stone type	Quarried raw material	Building stone in structure
Quartz kaolinite sandstone	6.1	9.5
Iron sandstone	6.0	11.1

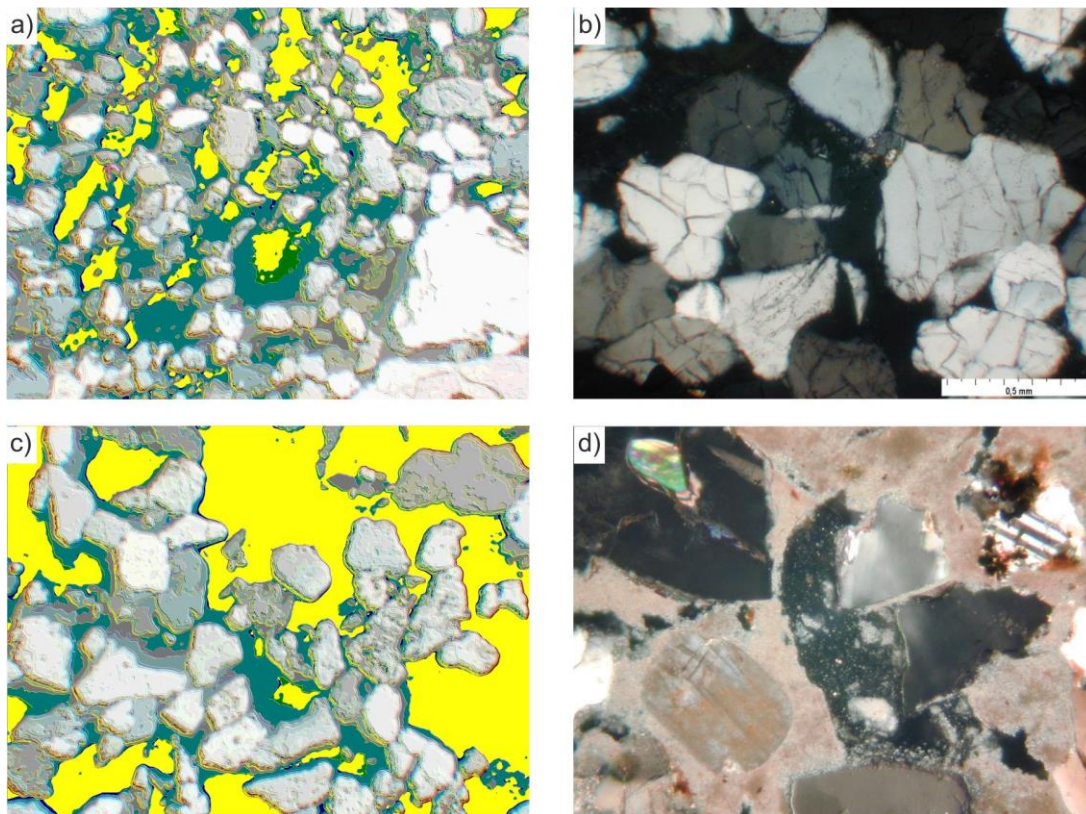


Fig. 1 - a) Pore system of quartz-kaolinite sandstone – initial raw materials, b) Structure and mineral composition of quartz-kaolinite sandstone – initial raw materials. Polarized light microscopy, XPL. Photo by Gregerová, c) Pore system of quartz-kaolinite sandstone – building stone of Charles Bridge, d) Structure and mineral composition of quartz-kaolinite sandstone – building stone of Charles Bridge with carbonate-sulphate binder. Polarized light microscopy, XPL. Photo by Gregerová

The microstructure of sandstone blocks is weakened by the effect of polarization pressures (2-50MPa, Winkler 1975). The original face masonry blocks used in the structure of Charles Bridge (14th century), for example, presently differ by their carbonate-sulphate binder from primary sandstone sources s.l. It has been manifested that sulphates are found to a depth

of ca 1-2mm and below them calcite can be identified in the binder to a depth of max. 5cm (see Figure 2). The results of long-term experimental research [7, 8] of degradation processes on sandstone blocks of Charles Bridge prove a serious effect of these processes – of physical, chemical and mineralogical nature accompanied usually by the effect of elevated moisture.

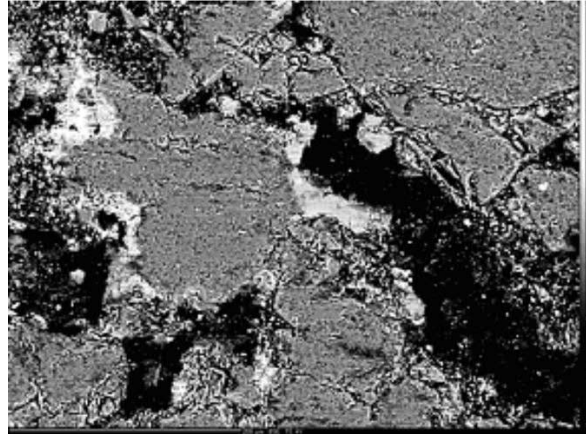


Fig. 2 - Overall distribution of Ca manifesting its presence in carbonate-sulphate binder. Electron microscopy - Cameca SX 100, photo by R. Čopjaková

The action of degradation processes e.g. on the building stone of Charles Bridge in the final phase results in the disintegration of the structure of sandstones s.l. and mechanical disintegration of rocks (building blocks). The exfoliation is most intensively manifested on the face of sandstone blocks s.l. (see Figures 3 and 4).

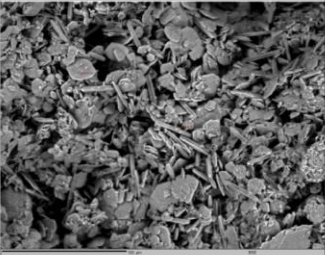
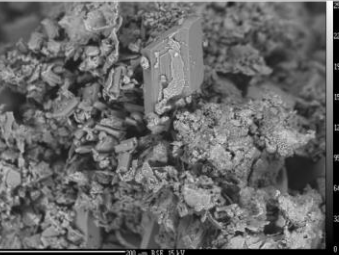
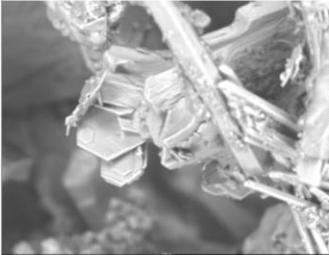
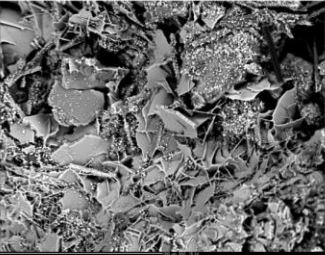
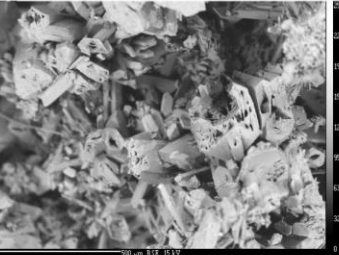
Arch and place	Summer 2003	Winter 2004	Summer 2004
III-5 C	 <p>Crystals trona $Na_3(HCO_3)(CO_3) \cdot 2(H_2O)$. Cameca, fig. R. Čopjaková.</p>	 <p>The gypsum crystals and chlorite Na-chlorite with a fine coating of clay minerals. Cameca, fig. R. Čopjaková.</p>	 <p>Gypsum crystals covered with clay minerals. Cameca, fig. R. Čopjaková.</p>
IV -3-D	 <p>Detail jarosite (sulfate K and Fe). Cameca, fig. R. Čopjaková.</p>	 <p>Crystals alunogen. Cameca, fig. R. Čopjaková.</p>	 <p>Corrosion of gypsum. Cameca, fig. R. Čopjaková.</p>

Fig. 3 - Gradual change in the mineralogical composition of efflorescence in the annual cycle in selected sampling places of Arch III and IV of Charles Bridge

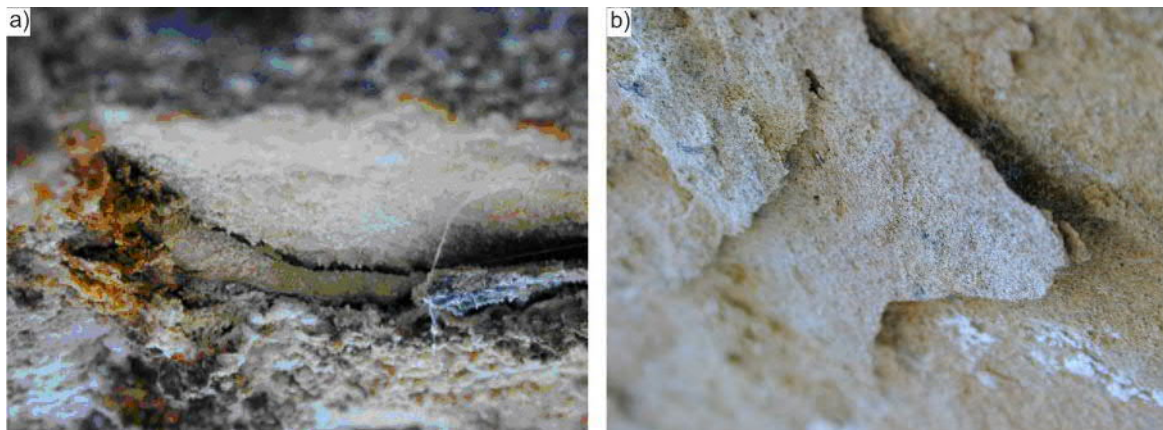


Fig. 4 - a) Example of plate exfoliation of sandstone (cm), b) Example of exfoliation of sandstone laminas (mm). Photo by P. Pospíšil

Degradation processes disintegrating the structure of sandstones in surface layers also result in changes in the physical and mechanical properties of the whole rock mass volume of freestone masonry (Table. 2).

The results of laboratory analyses also confirm the severe effect of moisture changes on the strength of freestone masonry.

Tab. 2 - Compressive strength of sandstone in saturated state and dry state tested on test pieces 50 mm in diameter and the softening coefficient (according to Cikrle)

Test piece	Locality	Initial raw material		Building stone of Charles Bridge				Softening coefficient KZ_c
		Compressive strength $R_{c,n}$ saturated [MPa]	Compressive strength R_c dry [MPa]	Compressive strength $R_{c,n}$ Saturated [MPa]		Compressive strength R_c dry [MPa]		
				individual	mean	individual	Mean	
B 1	Božanov	51.7	57.0		33.9	47.4	44.1	0.77
B 3	Božanov			33.9		40.8		
Z 1	K. Žehrovice	55.4	70.2	41.6	45.6	58.0	58.5	0.78
Z 3	K. Žehrovice			51.9		61.2		
Z 5	K. Žehrovice			43.2		56.4		

Note: The falling values of the softening coefficient document the decrease in the compressive strength (quality) of building stone exposed to elevated moisture contents.

Experimental research (MSM6840770001, GAČR 103/02/0990/A, DF12P010VV037) conducted at the authors' workplace has manifested a significant effect of moisture on the physical and mechanical properties of porous materials.

Figures 5 to 8 present partial results of experimental research which document the effect of moisture on the compressive strength and modulus of elasticity of fine-grained and coarse-grained sandstone.

Fine-grained sandstone

The correlation of the ultimate compressive strength f_{ubexp} with the percentage of moisture content by weight w_{hm} (Figure 5) showed a nearly identical pattern in all specimens of fine-grained sandstone characterised by a gradual decrease in the ultimate compressive strength in compression f_{ubexp} with the growing moisture content by weight w_{hm} , where in some specimens of fine-grained sandstone this decrease was more prominent in the interval of 0-50% saturation.

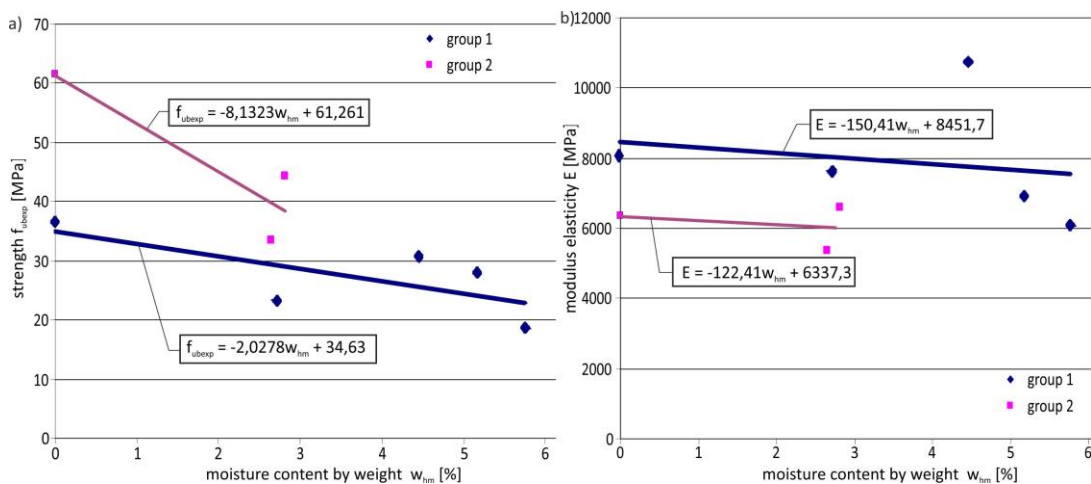


Fig. 5 - Correlation of the ultimate compressive strength f_{ubexp} (a) and the static modulus of elasticity in compression E (b) with the moisture content by weight w_{hm} of groups of fine-grained sandstone specimens [10]

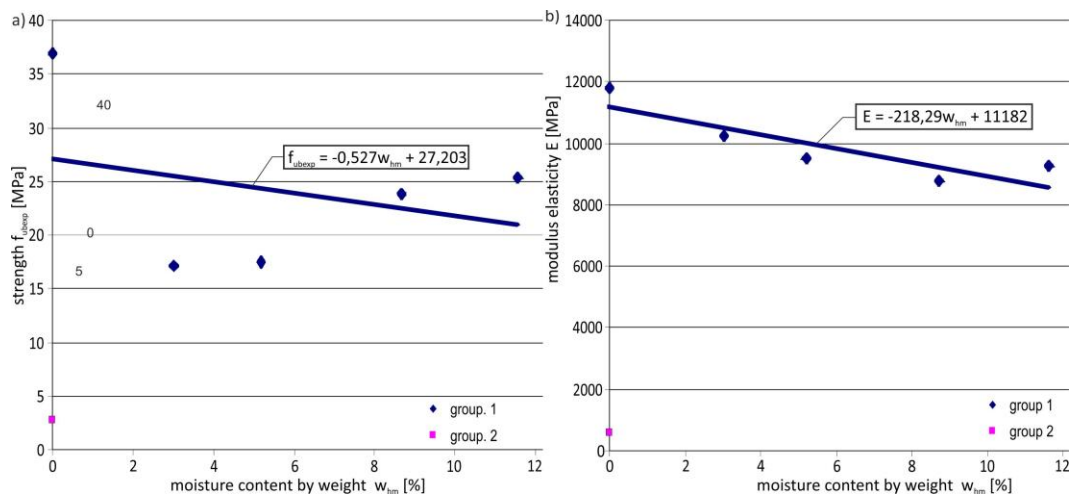


Fig. 6 - Correlation of the ultimate compressive strength f_{ubexp} (a) and the static modulus of elasticity in compression E (b) with the moisture content by weight w_{hm} of groups of coarse-grained sandstone [10]

The correlations of the static modulus of elasticity in compression E with the saturation of pores are, with some exceptions, characterised by a relatively low dependence of the values of the static modulus of elasticity in compression E on the saturation of pores (Figure 5). In the interval of

0 - 100% saturation, in specimens with the values of the static modulus of elasticity E higher than $2 \cdot 10^3$ MPa, this change does not exceed ca 20 - 30% of the static modulus of elasticity in compression E of a dry specimen.

Coarse-grained sandstone

The correlation of the ultimate strength f_{ubexp} with the percentage of the moisture content by weight w_{hm} of a coarse-grained sandstone specimen (Figure 6) is characterised by an initial decrease in the ultimate strength in compression f_{ubexp} with the growing moisture content by weight and a subsequent increase in the ultimate compressive strength f_{ubexp} , where at full saturation of pores the ultimate strengths in compression f_{ubexp} of coarse-grained sandstone reach lower values compared to the ultimate strength in compression f_{ubexp} of dry specimens. The lowest values of the ultimate compressive strength f_{ubexp} of coarse-grained sandstone were identified at saturation $w_{hm} \in (5 - 8)$ %. This decrease accounted for ca 50% compared to the ultimate strength of dry specimens.

The dependence of the static modulus of elasticity in compression E of coarse-grained sandstone on the saturation of pores (Figure 6) is characterised by a relatively small decrease in the static modulus of elasticity in compression E at greater saturation of pores. At 100% pore saturation ($w_{hm} = 11.8\%$), there was a decrease in the value of the static modulus of elasticity in compression E of coarse-grained sandstone by ca 20% compared to the value of the static modulus of elasticity in compression E of a dry specimen of coarse-grained sandstone.

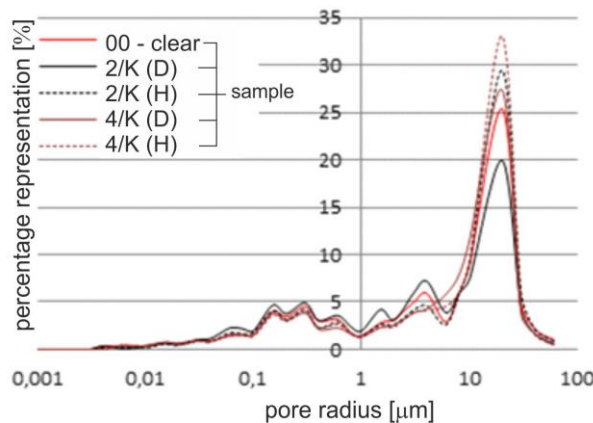


Fig. 7 - Change in the pore distribution of sandstone specimens from Ostroměř loaded by the H₂O solution – specimen 00 – original pure sandstone, specimen 2 – after 14 loading cycles using water, specimen 4 - after 41 loading cycles using water [11]

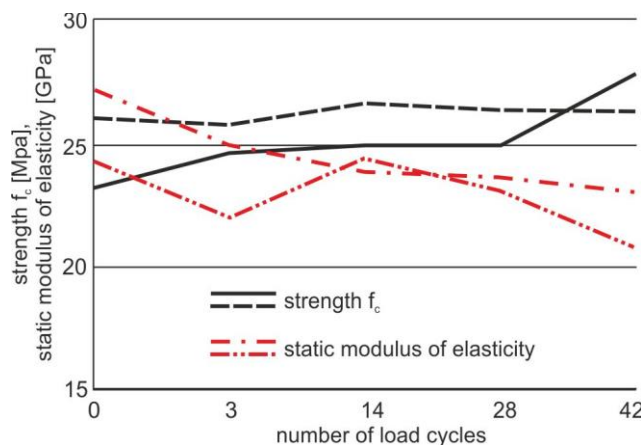


Fig. 8 - Correlation of the uniaxial compressive strength R_c [MPa], the static modulus of elasticity E_b [GPa] of sandstone from Ostroměř locality with the number of loading cycles using 0.5% and 3% NaCl solutions and distilled water [11]

Figure 7 presents the experimentally identified dependence of the pore distribution in sandstone on the number of loading cycles using water (DP SN). Figure 8 shows the dependence of the uniaxial compressive strength R_c [MPa], the static modulus of elasticity E_b [GPa] of sandstone on the number of loading cycles using distilled water.

CONCLUSION

Experimental research has manifested that the determination of the degree and extent of degradation processes of historical building materials, mainly sedimentary rocks, is the basis for not only the identification of their residual service life, but also for the design of rehabilitation – conservation and restoration – methods used during the restoration of historic and heritage buildings.

ACKNOWLEDGEMENTS

The article was written with support from the NAKI DG16P02M055 project "Research and development of materials, processes and techniques for restoration, preservation and strengthening of historic masonry structures, surfaces and systems for preventive care of heritage buildings exposed to anthropogenic and natural risks" of the Ministry of Culture of the Czech Republic.

REFERENCES

- [1] Witzany, J., Stařecký, I., Michalko, O., Toman, J.: Degradation Processes of Building Materials and Structures. A report for MIT CR. FCE CTU, 1992. (in Czech)
- [2] Witzany, J.; Čejka, T.; Wasserbauer, R.; Zigler, R. 2010 FDR – Failures, Degradation, Reconstructions, 1st edition. in Czech, CTU Publishing House, Praha. ISBN 978-80-01-04488-9 (in Czech).
- [3] Witzany, J.; Čejka, T.; Zigler, R. Load-bearing capacity determination of historic masonry structures In: Advanced Materials Research. 2014. ISBN 978-3-03835-083-5.
- [4] Witzany, J.; Čejka, T.; Zigler, R. The effect of moisture on significant mechanical characteristics of masonry In: Structural Stability and Ductility. 24.09.2009 - 25.09.2009. Vilnius, LT.
- [5] Witzany, J. et al.: Chemical and Biochemical Degradation of Charles Bridge, Analysis of the Resistance and Safety of the Stone Bridge Structure in Floods, Investigation of Foundation Masonry and Bridge Pier Foundations, Stavební obzor, 12, 2003, No. 6, p. 161–180, ISSN 1210-4027.
- [6] Witzany, J. - Wasserbauer, R. - Gregerová, M. - Pospíšil, P. - et al.: Comprehensive Assessment of a Theoretical and Experimental Investigation of Charles Bridge 1994 to 2004, Part 2. In Stavební obzor. 2005, vol. 14, No. 4, pp. 65-82. ISSN 1210-4027. (in Czech)
- [7] Grant GAČR 103/06/1801 "Reliability Analysis of the Properties of Building Materials and Structures with a Focus on their Time-related Changes and Time-variable Effects", in Czech, 2006- 2008, senior researcher prof. Ing. Jiří Witzany, DrSc.
- [8] Research Plan MSM 6840770001 "Reliability, optimization and durability of building materials and structures", senior researcher prof. Ing. Jiří Witzany, DrSc., 2005-2011
- [9] Research Project NAKI DF12P01OVV037 project "Progressive non-invasive methods of the stabilisation, conservation and strengthening of historic structures and their parts with composite materials based on nanofibres", 2012 – 2015, senior researcher prof. Ing. Jiří Witzany, DrSc.
- [10] Čejka, T.: Experimental In-situ Research of Moisture Effect on Mechanical Properties of Historic Masonry Structures, Habilitation thesis, FCE CTU, Praha 2009.
- [11] Neubergova, S.: Analysis of selected degradation factors' influence on physical and mechanical properties of natural stone; Doctoral dissertation, FCE CTU, Praha 2015.

IN-SITU TEST EXPERIMENTAL RESEARCH ON LEAKAGE OF LARGE DIAMETER PRE-STRESSED CONCRETE CYLINDER PIPE (PCCP)

Jianjun Luo¹, Liping Gao¹

¹ Tunnel and Underground Engineering Research Center of Ministry of Education, Beijing Jiaotong University, Beijing, 100044, China; email, jj_luo@126.com

ABSTRACT

In recent years, a big number of large diameter pre-stressed concrete cylinder pipe (PCCP) lines have been applied to the Mid-route of the South-to-North Water Transfer Project. However, the leakage problem of PCCP causes annually heavy economic losses to our country. In such a context of situation, how to detect leaks rapidly and precisely after pipes appear cracks in water supply system has great significance. Based on the study and analysis of the characteristic structure of large diameter PCCP, a new leak detection system using fiber Bragg grating sensors, which can capture signals of water pressure change, is proposed. The feasibility, reliability and practicability of the system could be acceptable according to data achieved from in-situ tests. Moreover, the leak detection system can monitor in real-time of dynamic change of water pressure. The equations of the leakage quantity and water pressure have been presented in this paper, which can provide technical guidelines for large diameter PCCP lines maintenance.

KEYWORDS

Large diameter pre-stressed concrete cylinder pipe; Leakage; In-situ Test; Fiber Bragg Grating

INTRODUCTION

PCCP, as a new kind of composite pipe which fully utilizes tensile characteristic of steel and compression performance of concrete, is widely used at home and abroad for its long service life, good seismic performance, easy installation, low operating cost, etc. Lots of large diameter PCCP lines have been adopted in the Mid-route of the South-to-North Water Transfer Project for its advantages. However, PCCP could leak water for some reasons, such as differential settlement or deformation of pipes and seal rubber grommet of pipes aging or losing effectiveness. It is not hard to understand that leakage problem brings great property damage to China. Experimental researches on leakage of PCCP lines have been still rare until now, not mentioning large diameter PCCP in-situ tests. Mature automatic leak detection techniques of large diameter PCCP have not been applied widely in China. Furthermore, there are no formal codes for leak detection for reference. The common technologies for leak detection include Acoustic Emissions, Fiber Optic Sensing, Liquid Sensing and Vapor Sensing. The Acoustic Emissions is the only technology applied in the long pipelines. Acoustic Emissions has faults, for instance, its incapable of in-time monitoring. Considering this, the paper introduces a new leak detection system for large diameter PCCP pipelines based on fiber Bragg grating sensing technology. Sensitivity and reliability of the system are evaluated by in-situ tests. Meanwhile, the relationship between leakage and pressure is also presented and it will provide effective guidelines for PCCP pipelines.

METHODS

Materials for this research: Optical fibre; sensor; large diameter PCCP pipeline; signal modulation mediation instrument.

Method used: Field experiments.

1. A BRIEF INTRODUCTION TO THE PRINCIPLE FOR IN-SITU TESTS OF PCCP PIPELINES

1.1. The principle for real-time leak detection monitoring of PCCP pipelines

The layout of pipes and equipment for the field test are shown in Figure 1-1. Water pressure in the circular cavity formed by rubber ring 1 and rubber ring 2 will change if the bell and spigot faucet for PCCP is broken. The change of water pressure will help realize real-time monitoring for leak detection. And following will be how the system works.

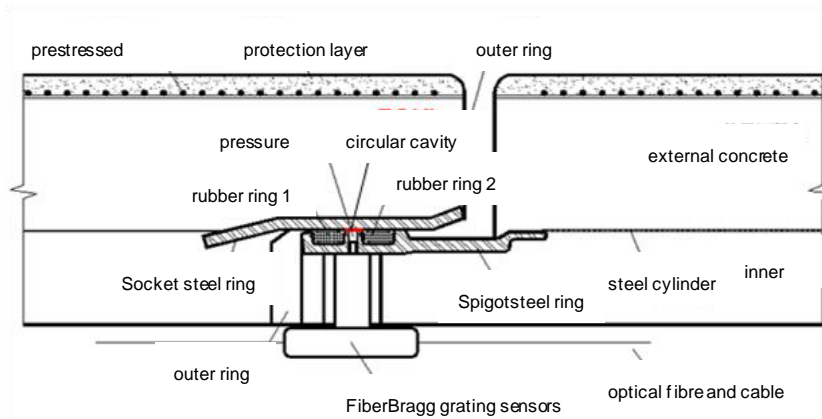


Fig. 1-1 - The layout of pipes and equipment for the field test

Fiber Bragg grating sensors are placed on the pressure hole through the nipple, meanwhile, the other pressure hole is blocked by a bolt. Water will not flow into the circular cavity in a normal circumstance, water pressure is zero now. However, water pressure will not be zero if there is something wrong with rubber ring 1 or rubber ring 2 leading water flowing into the circular cavity through one of the twin rubber rings. The pressure change will be sensed in real-time by the fiber Bragg grating sensor placed on the pressure hole. The fiber Bragg grating will transform water pressure signals to the fiber Bragg grating demodulator and the computer can transform, paralyze and process signals. These signals will eventually be transformed into the data of water pressure change used to judge whether a pipe leaks or not, and also seepage discharge could be calculated. The installation position of the fiber Bragg Grating is fixed. So, pipe leaks can be located precisely based on the position.

1.2. In situ-test

The main indigenous equipment for the field test includes two PCCP pipelines, fiber Bragg grating demodulator, fiber Bragg grating, computer for the test, pressure hole pump and water injection equipment. The detailed procedure is described below. First, form pressure holes using the pressure hole pump. Second, correct the leak detection system. Finally, detect the pipes.

2. EXPERIMENT RESULTS AND ANALYSIS OF IN-SITU TESTS

2.1. Pre-pump for pressure hole test

In order to ensure the tightness of rubber rings at the sealing of pipes and fiber Bragg grating in normal conditions, pre-pump for pressure hole test is proceeded. The test is done on the cylindrical container where are placed with fiber Bragg grating sensors using pressure pump artificially. The pressure is controlled to about 0.8 MPa. Three pump tests and unpump tests together.

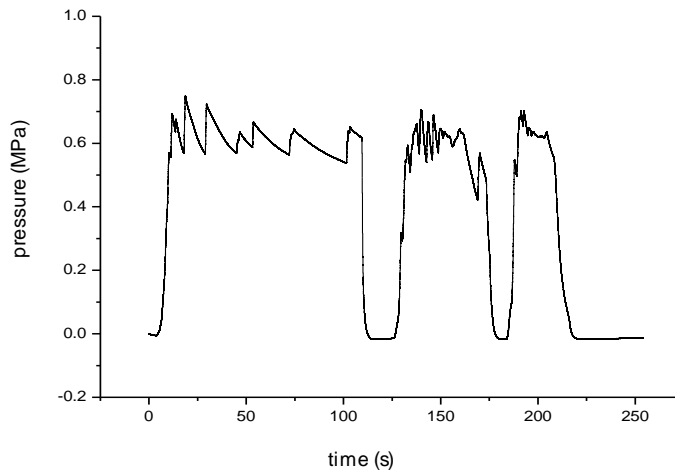


Fig.2-1 - The curve of pressure in pump hole

There are no water leakage points in process of pressure exerting. It indicates that the rubber rings are in their good sealing performances. The water pressure change sensed by the fiber Bragg grating is almost the same as the water pressure change displayed at pressure pump. It shows that the fiber Bragg grating sensors are reliable in measuring water pressure change. The test confirms the system’s reliability.

2.2. Leak detection system correction test

The rubber ring 1 and rubber ring 2 are destroyed wilfully before the test. During the test, exert pressure on water in the pipe to needed value using the electric pump

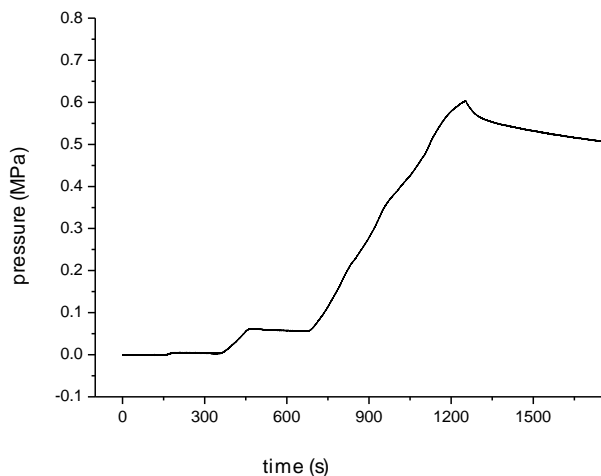


Fig.2-2 The change of water pressure measured by the fiber Bragg grating sensors

The leakage phenomenon at the bell and spigot faucet for PCCP could be found outside the pipe in the process of exerting pressure. When the water pressure elevates to about 0.6 MPa, the electric pump stops working. In the next stage, the water pressure decreases slowly all the time. It indicates that the water flows through twin rubber rings to outside. The whole change of water pressure is captured by the fiber Bragg grating sensors (See Figure 2-2), and this process is almost the same as that of the pipe. Thus, it is concluded that the system is valid.

2.3. Leak detection test

Based on the two tests above confirming the reliability and validity of the system, the test is adjusted in order to get the relationship between the leakage quantity and the water pressure. The test mainly focuses on the cylindrical container. The layout of the fiber Bragg grating and several function holes are shown in Figure 2-3. There are two blastholes, an adjust hole and three weep holes, and all holes are new formed in the cylindrical container.

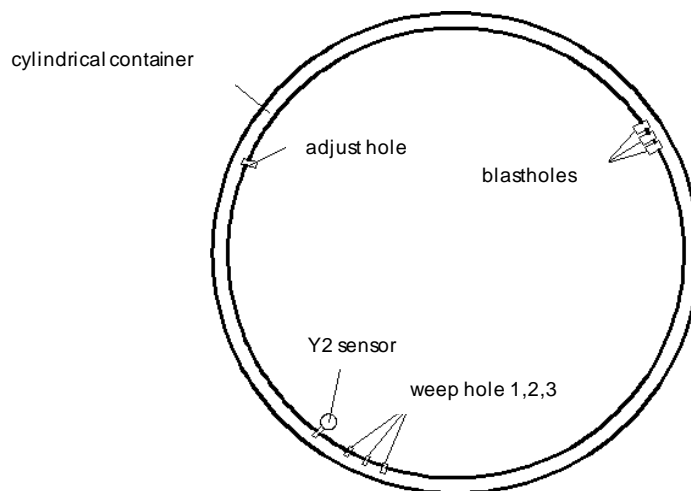


Fig.2-3 Schematic location diagram of the sensor and the functional holes

As the electric pump works, water will flow from the blasthole into the cylindrical container, as Figure 2-4 shows. The water coming from a blasthole will drain out of the weep hole through the adjust hole and Y2 sensor. There is a screw, the depth can be controlled to change and adjust the pressure in the adjust hole, as Figure 2-5 shows. The Y2 sensor is placed in the pressure hole above weep holes to measure water pressure of water of the weep hole, as Figure 2-6 shows. The Y3 sensor is placed on a tee union which is connected with a pressure hole neighbouring with a blasthole to measure water pressure of water of the blasthole, as Figure 2-7 shows.



Fig.2-4 blasthole



Fig.2-5 adjust hole

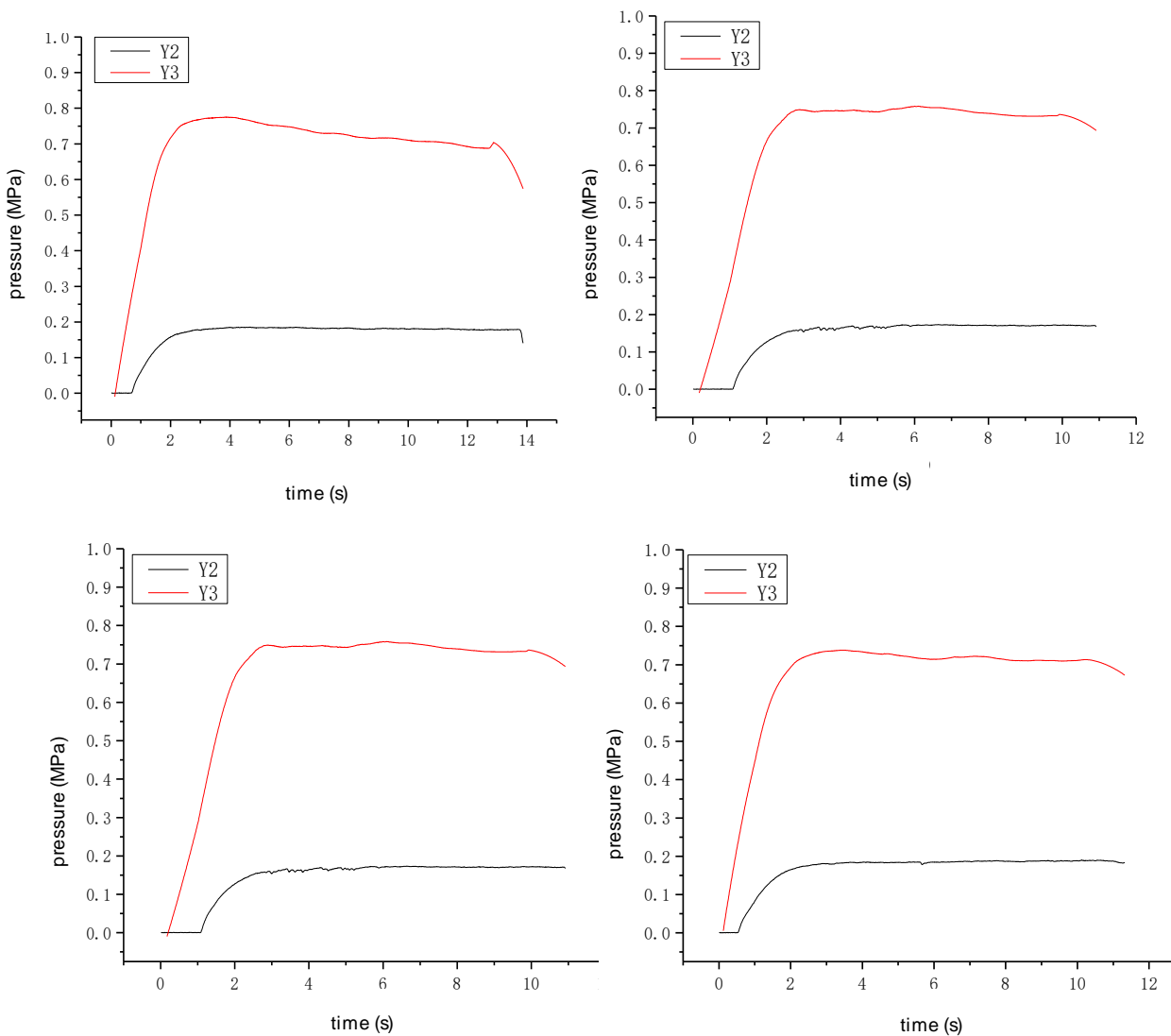


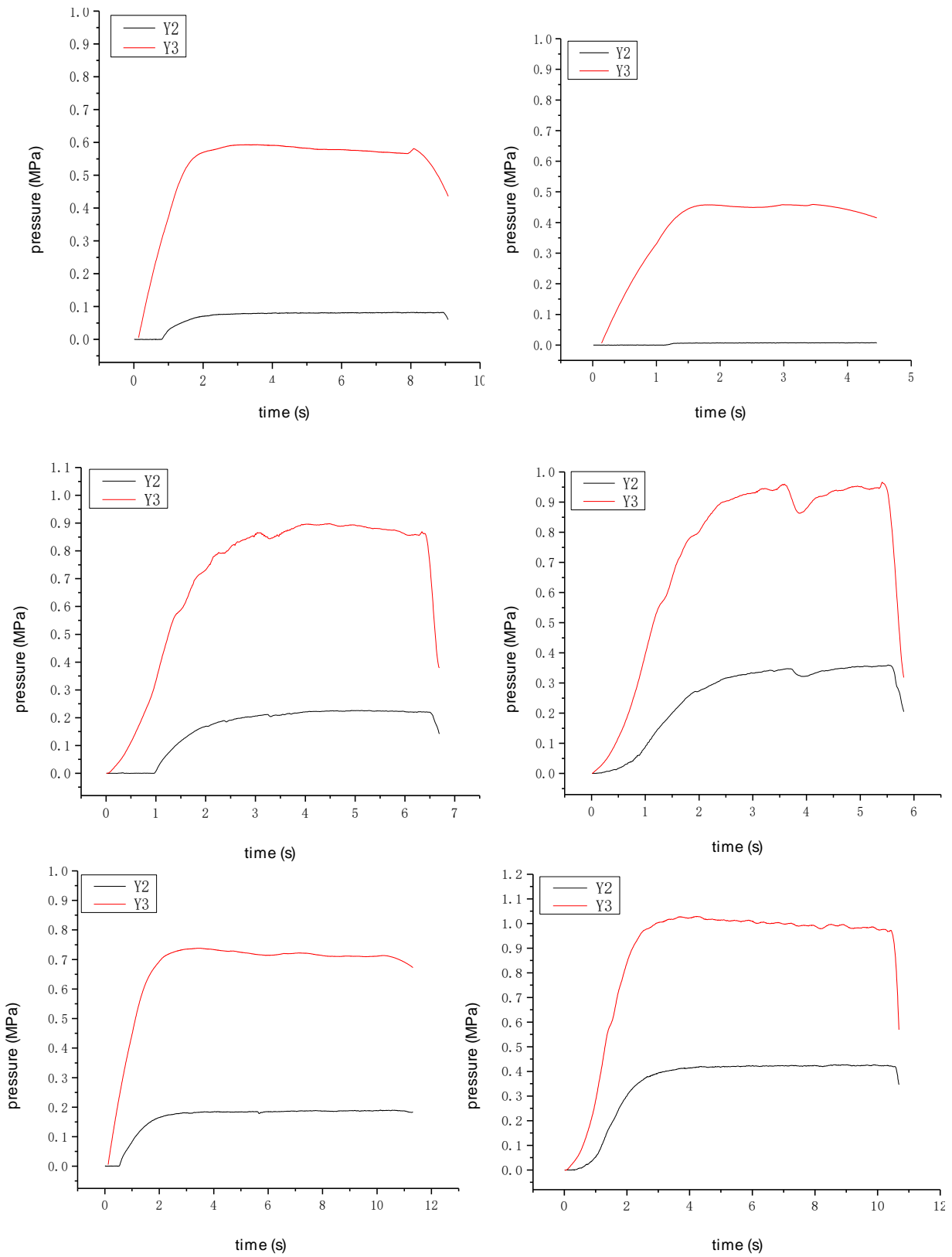
Fig.2-6 Y2 sensor



Fig.2-7 Y3 sensor

Adjust water pressure of blastholes to measure water leakage and flow rate in the pipe at the blastholes and the weep holes, and 11 groups of experimental data are got, as Figure 2-8 show.





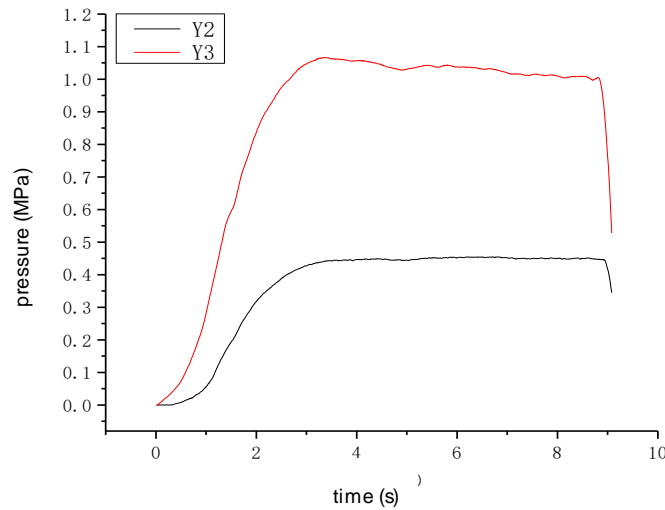


Fig.2-8 water pressure in the pipe varying with time

The water pressure got at the blastholes and weep holes, time, leakage and leakage rate are shown in Table 1.

Tab. 1 - Relationship of inlet pressure, outlet pressure, time, leakage and leakage rate

Name of experiment	inlet pressure [MPa]	outlet pressure [MPa]	Time[s]	Leakage[ml]	leakage rate [ml·s ⁻¹]
1.Screw in 10 buttons nut	0.75	0.18	13.96	1500	112
2.Screw in 8 buttons nut	0.74	0.17	10.72	1125	108
3.Screw in 6 buttons nut	0.79	0.13	11.84	1300	113
4.Screw in 4 buttons nut	0.73	0.15	9.37	1020	110
5.Screw in 2 buttons nut	0.58	0.08	9.03	900	100
6.Don't screw in the nut	0.46	0.007	4.42	500	98
7.Tighten the nut	0.9	0.22	6.94	875	126
8.Screw in 2 buttons nut in the weep hole 1	0.95	0.35	5.74	1350	235
9.Screw in 4 buttons nut in the weep hole 1	0.98	0.21	9.55	900	103
10.Tighten the nut in the weep hole 1	0.99	0.42	10.64	1400	132
11.Insert the screwdriver in the weep hole 1	1	0.45	8.88	1600	180

After an analysis of data of Table 1, the relationship between the water pressure at the blastholes in the pipe and the leakage quantity can be described into a curve (1) shown as Figure 2-9, the equation between two variables is described as following:

$$Q=112.93-81.10 p+102.98 p^2 \tag{1}$$

Where Q represents leakage rate in a unit of ml/s; p represents water pressure at the blastholes in a unit of MPa.

In the same way, we could get another curve describing the water pressure at the weep holes in the pipe and leakage quantity (2) shown as Figure 2-10, the equation between two variables is described as following:

$$Q=96.20+37.01 p+334.22 p^2 \tag{2}$$

Where Q represents leakage rate in a unit of ml/s; p represents water pressure at the weep holes in a unit of MPa.

Through the two equations above, we can calculate leakage rate based on the water pressure sensed by the fiber Bragg grating sensors.

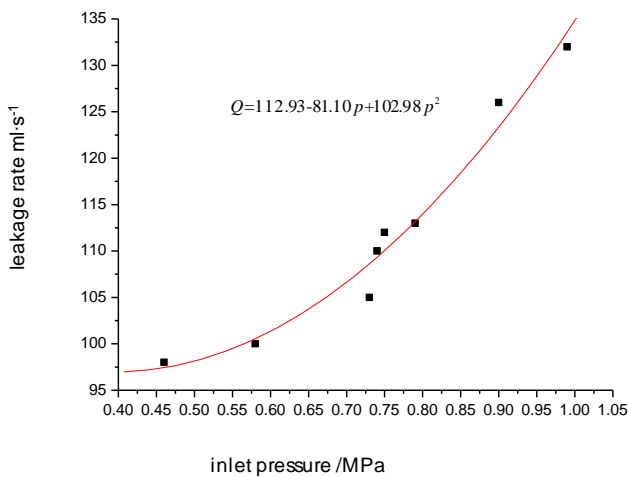


Fig.2-9 the diagram for pipeline leakage rate and inlet pressure

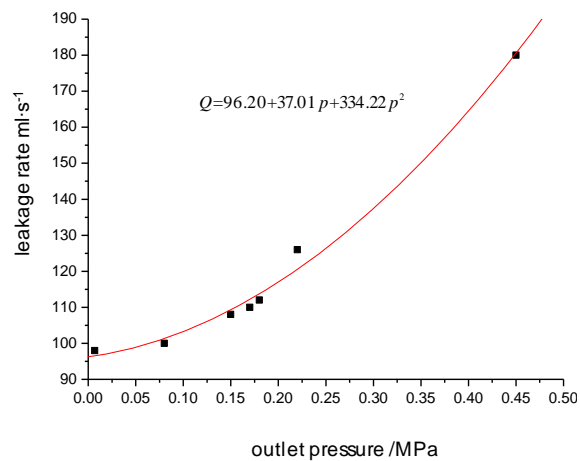


Fig.2-10 the diagram for pipeline leakage rate and outlet pressure

3. MONITOR CONTROL STANDARD FOR REAL-MONITOR OF LEAKS OF PCCP PIPES

There are two aspects for the control standards. One aspect is detecting water leaks of Pipe lines. The other is standard for how to judge water leak state.

1) Finding out water leaks

As the spot in which the sensors are placed is totally fixed, it's convenient to find out where water leaks precisely based on the places and where the sensors are fixed. Water will leak out of the pipes when the pressure sensed by the sensors is over zero.

2) Based on the principle of the system, three cases for judging leaks are listed below:

a. As water pressure sensed by the sensors is over zero and increases gradually to the pressure value of the pipe, we can make a conclusion that rubber ring 1 fails, rubber ring 2 is still at work, the pipe is in order, and no water leaks out.

b. As water pressure sensed by the sensors is over zero and increases gradually to the pressure value of the pipe, however, decreases gradually and final reduces to a certain value, we can judge that the rubber ring 1 and the rubber ring 2 are both out of order. At the same time, the tube leaks and is out of work. Water leak flow rate and leak quantity can be calculated through the relationships between the pressure in the pipe and the water leak quantity since the water pressure is easily sensed by the Grating Sensors.

c. As water pressure sensed by the sensors is over zero and increases gradually to a certain value which is much less than the water pressure in the pipe and there is no pressure reducing trend, the rubber ring 2 is out of work and the rubber ring 1 is still okay. The pipe is at work and no water leak takes place.

CONCLUSION

Based on the study on the analysis of large diameter PCCP itself characteristic structure, the authors propose a new leak detection system using fiber Bragg grating sensors which can capture signals of water pressure change. The feasibility, reliability and practicability of the system could be accepted according to the data achieved from in-situ tests. The creativity will provide some experience for operations of PCCP pipelines, meanwhile, provide reference for monitor regulations of leak detection.

- 1) A new real-time monitoring leak detection system and technology is presented, whose reliability and feasibility is tested through in-situ tests.
- 2) Leak equipment, detectors and software system for in-time leak detection are invented. The reliability and feasibility is tested through in-situ tests.
- 3) The paper establishes the way and the system to locate possible leaks fast and accurately.
- 4) The paper establishes codes and procedures for leak detection of large diameter of PCCP lines.
- 5) The relationship between the water pressure in PCCP and the leak quantity is first presented by in-situ tests. Leak quantity can be calculated through data achieved from leak detection system.

ACKNOWLEDGEMENTS

The paper is supported by the 11th Five-Year" National Science and technology support project (2006BAB04A04).

REFERENCES

- [1] SHEN Jie, 2010. Experimental study on structure safety performance and theoretical analysis for large caliber PCCP. Nanjing Hydraulic Research Institute.
- [2] CHEN Yuchun, OUYANG Yue, XU Zhonghui, SHI Hongmei, 2008. Application of PCCP pipeline to emergency water supply project (Beijing Section) for Beijing-Shijiazhuang Section in Mid-route of South-to-North Water Transfer Project. *Water Resources and Hydropower Engineering*, vol.39(5):51-55.(in Chinese)
- [3] TENG Haiwen, ZHANG Xiaojie, DAI Chunsheng, 2013. Analysis of effect of prestressed steel wire on the performance of PCCP. *Special Structures*, vol.30(5):37-40.(in Chinese)
- [4] HUSHao-wei, 2011. The structure bearing theory and practice of safety evaluation of PCCP. China Water Power Press, pp. 1-19.(in Chinese)
- [5] MEI Songjun, KUANG Ke, QU Yonggang, 2012. Anti-leakage Emergency Treatment Measures of Joint Internal Slit of Prestressed Concrete Pipe. *China Water & Wastewater*, vol.28(14):1-5.(in Chinese)
- [6] CHEN Yong, WEN Xiaoying, LI Shenlong, LI Chen, 2012. Analysis on Key Technical Problems in Application of Large-diameter Prestressed Concrete Cylinder Pipe. *China Water & Wastewater*, vol. 28(8):1-5.(in Chinese)



-
- [7] ZHONG Depai, 2011. Joints Leak Analysis and Processing of the Prestressed Concrete Cylinder Pipe. Journal of Guangdong Technical College of Water Resources and Electric Engineering, vol. 9(3):5-8.(in Chinese)
- [8] HU Shao-wei, SEHN Jie, WANG Dong-li, et al, 2010. The structure analysis and experimental research of large diameter pre-existing cracks concrete cylinder pipe. Journal of Hydraulic Engineering, vol.7:876-882.(in Chinese)
- [9] LING Qi, ZHOU Linhu, LIU Guanglin, CUI Gang, 2014. Study on the in situ leakage detection of the long-distance water transmission pipe with large diameter. Water & Wastewater Engineering, vol. 40(2):112-116.(in Chinese)
- [10] RI You, Hongbo Gong, 2012. Steel-cylinder yielding analysis of PCCP with broken wires. Advanced Materials Research, 503-504, pt.1819-1823,
- [11] CLARK B.L., 2014. From Underground to the Forefront of Innovation and Sustainability, Proceedings of the Pipeline 2014 Conference, HDR|Schiff, Claremont, CA, United States, pp. 256-266.
- [12] Ri You, Hongbo Gong, 2012. Failure analysis of PCCP with broken wires. Applied Mechanics and Materials, vol. 193-194, pt.2, pp.855-862
- [13] Ojdovic, R., Bracken, M. Marciszewski, J., 2015. Evaluation of Acoustic Wave Based PCCP Stiffness Testing Results. Proceedings of the Pipelines 2015 Conference. Recent Advances in Underground Pipeline Engineering and Construction, Baltimore, MD, USA, pp.1150-1158.

THREE-PARAMETER CREEP DAMAGE CONSTITUTIVE MODEL AND ITS APPLICATION IN HYDRAULIC TUNNELLING

Luo Gang¹, Chen Liang²

¹ School of Highway, Chang'an University, Xi'an, Shanxi, 710064; China; e-mail: Luogang@chd.edu.cn

² Guangxi Communications Investment Group Co, Nanning, Guangxi, China, 530029, e-mail: clng9716@163.com

ABSTRACT

Rock deformation is a time-dependent process, generally referred to as rheology. Especially for soft rock strata, design and construction of tunnel shall take full account of rheological properties of adjoining rocks. Based on classic three-parameter HK model (generalized Kelvin model), this paper proposes a three-parameter H-K damage model of which parameters attenuate with increase of equivalent strain, provides attenuation equation of model parameters in the first, second and third stage of creep deformation and introduces equivalent strain threshold value. When the equivalent strain is greater than the threshold value, the third stage of accelerating creep will be conducted. The three-parameter H-K damage model is used for numerical calculation of finite difference method FLAC^{3D} and deformation features of soft rock with time under high ground stress are described based on diversion tunnel project of Jinping Hydropower Station, of which model parameters can be obtained by back analysis according to measured site data and BP neural network.

KEYWORDS

Rheology; three-parameter H-K damage model; time-dependent deformation

1. INTRODUCTION

As shown from a large number of indoor tests and field tests, rock force deformation is a time-dependent process [1-3]. Especially for soft rock and loose rock mass with filling and fractured zone, the deformation possesses time effect. Elastic-plastic theory cannot describe and predict the process while rheological theory can better overcome this shortcoming. For force and deformation of cavern adjoining rocks in the tunnel and underground engineering, rheologic model shall be taken to reasonably interpret instability or even collapse during the construction of unsupported hole, deformation of adjoining rocks, continuously increased support structure deformation pressure ageing effect of lining and adjoining rock and other phenomena in the real-time engineering works [4-5].

Rheological properties of rocks become increasingly prominent in the construction of tunnel, slope and other fields. Especially under the condition of soft rock geology, long-term stability of engineering is closely related to rheological properties of rocks. Therefore, study

on rheological model of rock gets more attention. Through Kelvin, H-K, H | M and other viscoelastic models, classical linear elements (Hooke body) and viscous elements (Newtonian) provide preliminary understanding of rheological properties and identify them in a number of test results [6].

Many scholars proposed a modified rheological model based on test result to describe creep deformation of rocks, such as viscoelastic plastic damage model [7-8] providing an equation of rock strength parameters (c, ϕ) with the time. Constitutive relation of the viscoelastic plastic damage model is obtained based on standard thermal dissipation potential by the principle of strain and energy equivalence. Other scholars also conducted a study for this point [9-11]. The viscoelastic plastic damage model is proposed based on creep test results of rock specimen to reflect accelerating creep in the third stage, but it can be used to indicate more complex conditions now. Based on the three-parameter H-K damage model, this paper introduces the equation of model parameters attenuating with equivalent strain to propose a new modified H-K model and apply the model to numerical calculation of FLAC^{3D} and analyses creep deformation characteristics of soft rocks under high ground strain in the diversion tunnel engineering of Jinping II Hydropower Station.

2. THREE-PARAMETER H-K DAMAGE MODEL

2.1. Classic three-parameter H-K damage model

Classic three-parameter H-K damage model consists of elastomer and viscous body, as shown in Figure 1. G^E is shear modulus of elastic element; G^K and η^K are respectively shear modulus and viscosity factor of Kelvin body. Constitutive equation of the model is shown in (1), (2) and (3).

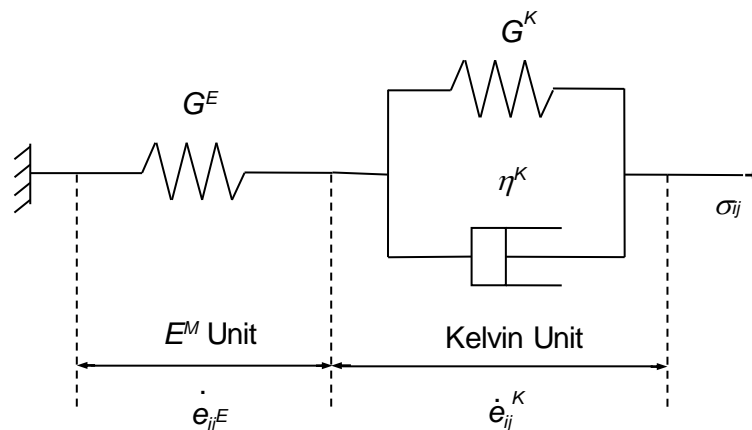


Fig. 1. - Classic Three-parameter H-K Damage Model

$$\dot{e}_{ij} = \dot{e}_{ij}^E + \dot{e}_{ij}^K \quad (1)$$

$$S_{ij} = 2\eta^K \dot{e}_{ij}^K + 2G^K e_{ij}^K \quad (2)$$

$$\dot{\epsilon}_{ij}^E = \frac{\dot{S}_{ij}}{2G^E} \quad (3)$$

In the above equation, ϵ_{ij} and S_{ij} are respectively deviatoric strain tensor and deviatoric stress tensor. Superscript E and K respectively indicate elastomer and Kelvin body. The three-parameter H-K model is a typical viscoelastic model without consideration of plastic deformation. It can better describe the first and second stage of creep deformation. With infinite time increase, the strain will tend to a stable value. But the model cannot reflect the third stage of accelerating creep.

2.2 Three-parameter H-K damage model

A number of rheological tests indicate the following characteristics of ϵ - t curve for rock creep deformation:

(1) Instantaneous application of stress σ will cause an instantaneous elastic deformation ($\epsilon_0 = \sigma/E$).

(2) When the stress level is lower than long-term intensity ($\sigma < \sigma_s$), strain growth rate gradually declines to 0. In case of $t \rightarrow \infty$, the strain will tend to a fixed value and materials will not have yield and damage but are only subject to the first stage (deceleration) and the second stage (stabilization) of creep.

(3) When the stress level is greater than or equal to long-term strength ($\sigma \geq \sigma_s$), the strain will increase infinitely with time and will not converge to a fixed value, materials will follow yield and destruction and the creep will enter the third stage (acceleration) after the first and second stage.

As shown from the above characteristics, creep deformation is generally divided into three stages. As shown in Figure 2, it is a nonlinear process. For relatively hard rocks, three-stage deformation is not significant. Especially when the material stress exceeds long-term strength, deformation time of the third-stage is short, that is, rocks are quickly destroyed; relatively soft rocks follow significant three-stage deformation characteristics. Three stages of creep deformation can be described by viscous elastic mechanics or visco-plasticity. When the viscous elastic mechanics is used for description without consideration of yield and plastic deformation, OA section is elastic deformation and AD section is three stages of creep deformation, as shown in Figure 2; when visco-plasticity is used for description with stress value greater than yield strength, OA section includes elastic deformation and plastic deformation. If the stress value fails to exceed the yield strength, the PA section will only include elastic deformation.

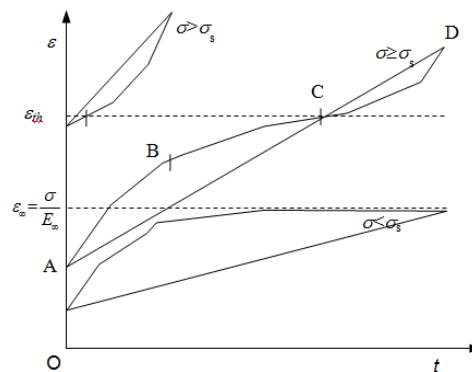


Fig. 2. - Creep Characteristic Curve of Three-parameter H-K Damage Model

According to the above characteristics, classic viscoelastic model can reflect elastic deformation and creep deformation in the first and second stages. For example, Burgers model and Xiyuan model can better indicate elastic deformation, decelerated creep and steady creep when the stress is greater than long-term strength. But they cannot describe accelerated creep deformation or indicate deformation convergence when the stress is smaller long-term strength. Three-parameter H-K (generalized Kelvin) viscoelastic model can properly indicate deformation convergence when the stress is smaller long-term strength, but it cannot describe characteristics of accelerated creep when the stress is greater than long-term strength.

Based on shortcomings of existing model, this paper proposes the three-parameter H-K damage model to introduce the damage equation of model parameters (G and η). In fact, relevant rheological test has proven that elastic modulus, compressive strength and other parameters of rocks attenuate with the time under a certain level of stress. When numerical calculation is conducted, it is difficult to determine the range of the rocks of which parameters attenuate with the time in the loading or unloading. Therefore, it is more appropriate that rock parameters attenuate with the strain and the strain itself is time-dependent in the creeping. If rock parameters attenuate due to strain, they will be also time-dependent. Therefore, attenuation of rock parameters under strain is defined as follows:

$$A_1(\varepsilon) = A_\infty + (A_0 - A_\infty)e^{-w_1(\varepsilon - \varepsilon_0)} = A_0 \left[k + (1 - k)e^{-w_1(\varepsilon - \varepsilon_0)} \right] \quad (\varepsilon < \varepsilon_{thr}) \quad (4)$$

$$A_2(\varepsilon) = A_1(\varepsilon_1) \left[2 - e^{w_2(\varepsilon - \varepsilon_1)^v} \right] \quad (\varepsilon \geq \varepsilon_{thr}) \quad (4)$$

Where, A indicates model parameter which can be shear modulus or coefficient of viscosity; $A_1(\varepsilon)$ indicates parameter change in the first and second stage of creep, $A_2(\varepsilon)$ indicates parameter change in three stages of creep, A_0 is an initial parameter value, A_∞ is a long-term parameter value, k is defined as attenuation ratio, namely $k = A_\infty / A_0$, ε_0 is the strain generated from elastic deformation, ε_1 is the strain in the first and second stage of creep, w_1 and w_2 are specific parameters and v is exponential quantity of ε .

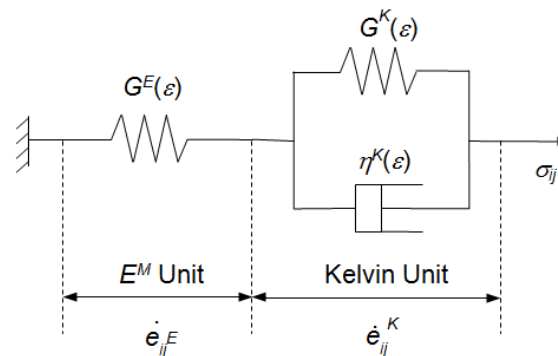


Fig. 3. - Three-parameter H-K Damage Model

As shown from the three parameters damage model H-K schematic shown in Figure 3, and the creep characteristic curve of three-parameter H-K damage model shown in Figure 2. strain threshold ε_{thr} , ε_{thr} is applied when it is equal to the strain generated during its long-term strength. When the strain exceeds the threshold, it will enter the third stage of accelerating creep, then the attenuation of rock parameters accelerates (formula (5)). To apply the equivalent strain ε_{eq} in the three-dimensional condition, namely, consider the six strain components into a linear stress. To substitute ε_{equ} by ε in formula (4) and (5), among which, the equivalent strain is as below:

$$\varepsilon_{equ} = \sqrt{\frac{2}{9}[(\varepsilon_1 - \varepsilon_2)^2 + (\varepsilon_2 - \varepsilon_3)^2 + (\varepsilon_3 - \varepsilon_1)^2]} = \sqrt{\frac{2}{3}(\varepsilon_1^2 + \varepsilon_2^2 + \varepsilon_3^2)} \quad (5)$$

Finite difference program FLAC3D did not give the principal strain, so it can be calculated by the following formula:

$$\varepsilon_{equ} = \frac{\sqrt{2}}{3} \sqrt{(\varepsilon_x - \varepsilon_y)^2 + (\varepsilon_y - \varepsilon_z)^2 + (\varepsilon_x - \varepsilon_z)^2 + 6(\gamma_{xy}^2 + \gamma_{xz}^2 + \gamma_{yz}^2)} \quad (6)$$

In the above formula, ε_1 、 ε_2 、 ε_3 refer to major principal strain, ε_x 、 ε_y 、 ε_z 、 γ_{xy} 、 γ_{xz} 、 γ_{yz} are the principal stress respectively.

In FLAC3D (Itasca Consulting Group, 1997), the calculation process parameters can be achieved through its built-in attenuation FISH language, each computing a time step (step or cycle), based on the equivalent strain increment model units and combined type (4) and (5) to calculate new creep parameters, then correct each unit cell parameters of the model until the calculated creep set time is reached. Stop the calculation when the parameters of accelerated decay to zero, which means it enters into the state of failure.

2.3 Example of three-parameter damage model

1/4 of tunnel dimension is taken as a calculation model with tunnel radius of 7m, horizontal coordinate range $x = 0$ to 60m, vertical coordinate range $z = 0$ to 60m and longitudinal coordinate range $y = 0$ to 1m. It can be divided into 1,556 nodes and 740 units. The model has restrictions imposed all round and takes initial ground stress σ_{zz} of 40MPa and lateral pressure coefficient of 1 to simulate deep tunnel. Calculation model and monitoring point arrangement are shown in Figure 4. For model parameters, see Table 1. The calculation shall not consider influence of support and volumetric strain, that is, the

calculation shall take volume modulus of 0, plane strain model and complete stress release without consideration of tunnel face influence.

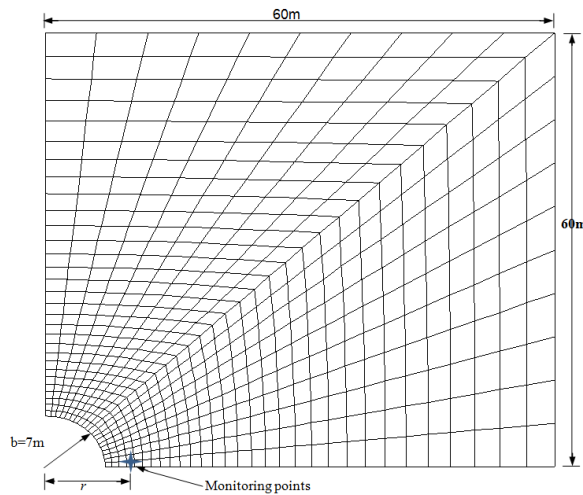


Fig. 4. Calculation Model

Tab 1. - Parameter Calculation

$G^M(\text{MPa})$	$G^K(\text{MPa})$	$\eta^K(\text{MPa Day})$	$\sigma_{zz}(\text{MPa})$	λ
3000	1000	20000	40	1

Attenuation of parameters in the first and second stage of creep deformation is calculated according to Formula (4) to get changing curve of tunnel side wall ($r=7\text{m}$) displacement with the time, as shown in Figure 5 and Figure 6. In case of $k=0$ and $w_1=0$, it is a viscoelastic solution of typical three-parameter model almost matched with results of analytic solution [12-13]; in case of $k=0.5$, it is a modified three-parameter viscoelastic damage model solution, indicating the displacement significantly grows with increase of w_1 value; in case of $w_1=50$, the displacement will quickly grow with reduction of k value and its growth rate will become larger when k value is smaller. According to the above calculation results, the calculation result considering damage (k and w_1 are not 0) is larger than that without consideration of damage under the condition of fixed model parameters.

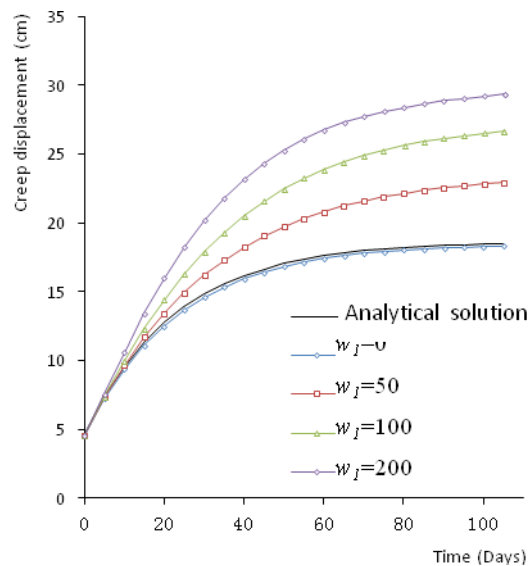


Fig. 5. - Calculation Result of Tunnel Side Wall Displacement ($r = 7m, k = 0.5$)

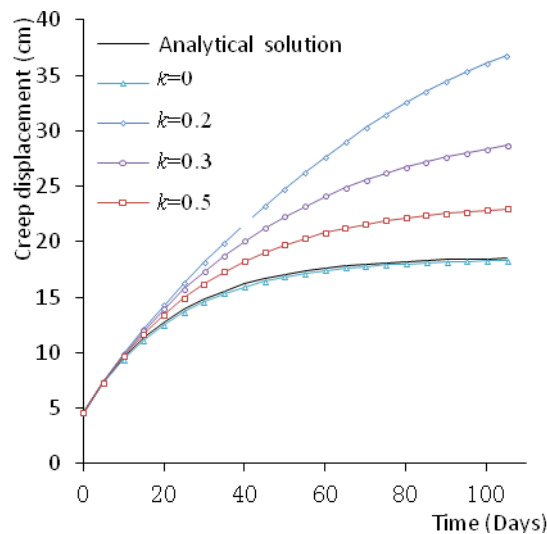


Fig. 6. - Calculation Result of Tunnel Side Wall Displacement ($r = 7m, w_1=50$)

According to the third stage of creep deformation calculation in formula (5), polt of side wall displacement is as shown in Figure 7. In the computing process, parameters acceleration could be judged by whether the equivalent strain of element (unit body) calculations exceeds the threshold ($\epsilon_{equ} > \epsilon_{thr}$). When creep into the third stage, the parameters w_2 and v influence the curves. As what could be seen from the figure, the smaller the w_2 , the faster the attenuation of parameters, which lead to obviously increased displacement.

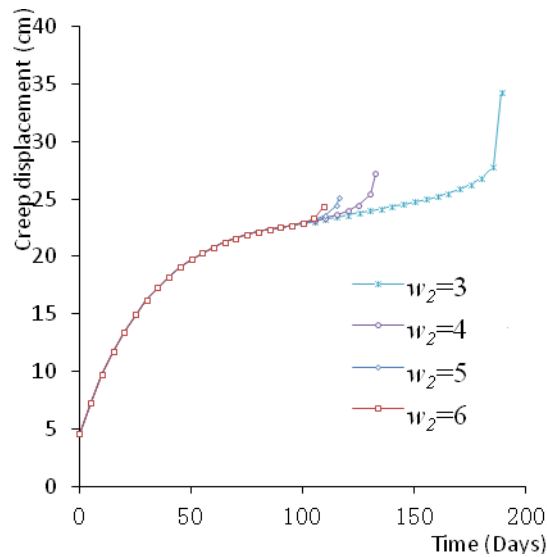


Fig. 7. - Calculation Result of Tunnel Side Wall Displacement ($r=7m$, $k=0.5$, $w_1=50$ and $\varepsilon_{thr}=0.038$)

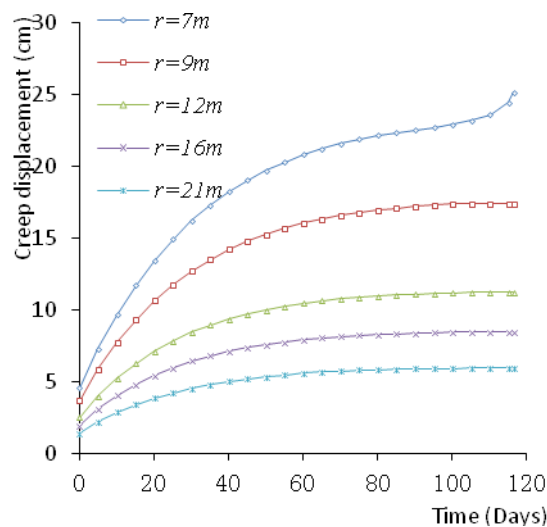


Fig. - 8. Calculation Result of Tunnel Side Wall Displacement

Figure 8 shows a different radial distance, changes of the adjoining rock displacement versus time, $r=7m$ shows the tunnel sidewall position, the elastic displacement of the apparent instantaneous maximum sidewall position, and through the three stages of creep deformation, first to destroy, indicating the stress suffered by a large rock in its long-term strength, strain over the threshold; whereas with increasing radial distance, instantaneous elastic displacement of rock decreases, and emerged with a timetable the first and second stages of creep deformation, indicating that rock is less than its long-term strength to withstand the stress and strain has not exceeded the threshold

3. RHEOLOGICAL ANALYSIS AND DISCUSSION

3.1 Divert tunnel of Jinping II Hydropower Station

Divert tunnel of Jinping II Hydropower Station was excavated to chlorite schist strata with a burial depth of about 1,500m in 2008. Under the influence of extreme-high geostress and low rock strength, the tunnel suffered large deformation and indicated time-dependent characteristics during the construction. Therefore, the three-parameter H-K damage model is used for describing and interpreting time-dependent deformation of the tunnel during the construction. Large deformation section of the diversion tunnel had the secondary excavation expansion in 2010. In this paper, rheological deformation of the tunnel before secondary excavation expansion is taken as the object of study.

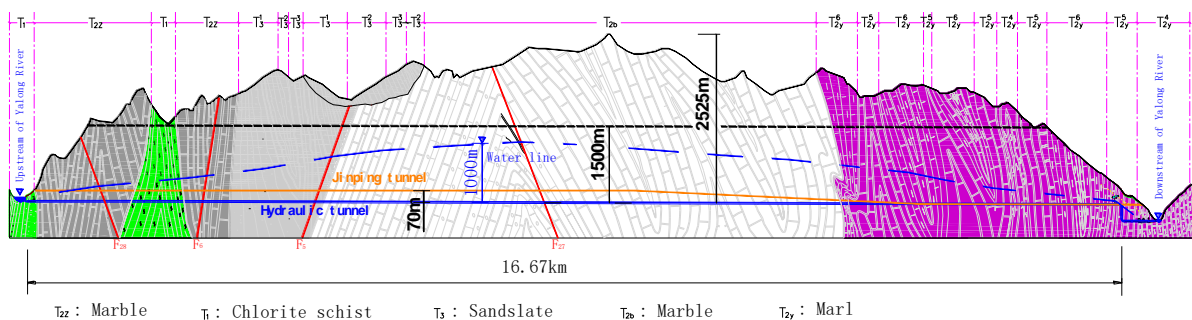


Fig. 9. - Geological Longitudinal Profile of Diversion Tunnel

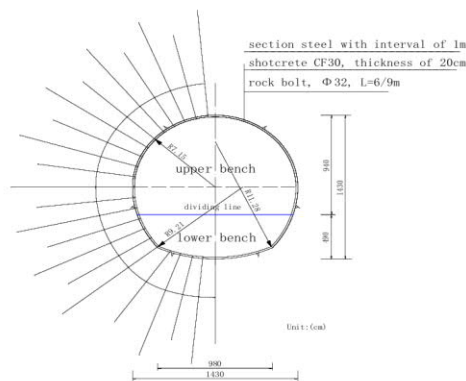


Fig. 10. - Cross Dimensions of Diversion Tunnel

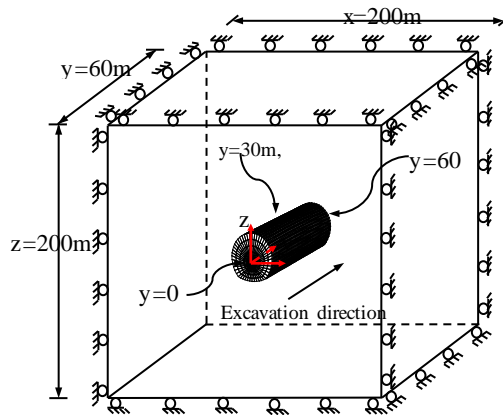


Fig. 11. - Model Boundary

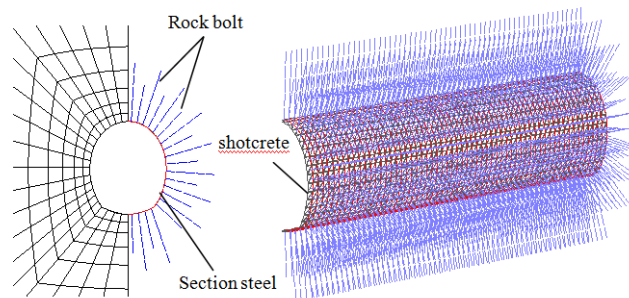


Fig. 12. - Support Model

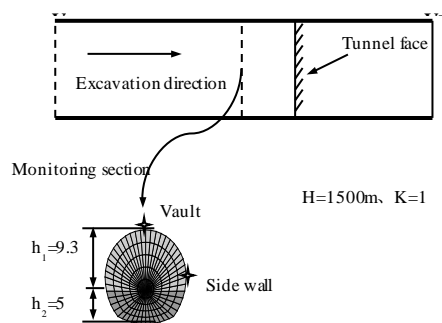


Fig. 13. - Monitoring Point Layout

Figure 9 demonstrates the geological section of water tunnel (Line1), Figure 10 indicates the fault plane dimensions, and computing model and monitors are arranged as shown from Figure 11 to 13. As the bench cut is adopted, and dig down the steps of the excavation was yet to be made before secondary evacuation, so the roof arch and side wall are set as the watch points. The depth of Analog excavation is 1m. To apply support including rock bolt, Steel arch and pneumatically placed concrete right after evacuation, and to simulate steel arch by beam elements, and to simulate pneumatically placed concrete by shell element, and to simulate rock bolt by cable element. Parameters of supporting structure and adjoining rocks are shown as Tables 2 and 3 as below.

Tab. 2. - Simulation Parameters of Support Structure

H20 Profile Steel		System Anchor Bolt		CF30 Shotcrete	
Elasticity modulus $E(\text{GPa})$	200	Elasticity modulus $E(\text{GPa})$	200	Elasticity modulus $e(\text{GPa})$	21.44
Poisson 's ratio μ	0.29	Cross-sectional area $A(\text{cm}^2)$	8.042	Density $P(\text{kg/m}^3)$	2500
Cross sectional area $A(\text{cm}^2)$	64.28	Tensile strength $F_t(\text{KN})$	241.3	Poisson 's ratio μ	0.2
Moment of inertia $I_y(\text{cm}^4)$	1600	Anchoring agent cohesion $C_g(\text{KN/m})$	200	Thickness $t(\text{cm})$	20
Moment of inertia $I_z(\text{cm}^4)$	4770	Anchoring agent stiffness $k_g(\text{MPa/m})$	17.5		
Polar moment of inertia $J(\text{cm}^4)$	6370	Anchoring agent outer perimeter (m)	0.1507		

Tab. 3. - Parameters of adjoining rock

$\rho(\text{kg/m}^3)$	$K(\text{MPa})$	$G^M(\text{MPa})$	$G^K(\text{MPa})$	$\eta^K(\text{MPa Day})$	k	w_1
2610	6000	1500	N/A	N/A	N/A	N/A

Note: adjoining rock failure is not considered and no value is assigned for w_2 , v and ϵ_{thr}

3.2 Rheological deformation characteristics

An analogue calculation is conducted for different deformation sections of K1+675, K1+760 and K2+665. Calculation results are only used for selecting time-dependent deformation. Calculated value is compared with measured data, as shown in Figure14 to Figure16. Curves in the figures show compliance of calculated value with measured data, indicating the three-parameter damage model has high adaptability. Model parameters are determined by the artificial neural network back analysis [14]. For lack of the space, specific methods are not detailed in the paper. GK, K, k and w_1 are parameters to be determined. To ensure balanced distribution of training samples, form design method can be used for the back analysis [15] to design normal analysis test plan. According to uniform design table of U30(304), design test combination, four factor levels and 30 sets of test data; particle swarm optimization method can be taken before BP network training to optimize initial weights and thresholds of BP network in order to improve network training effect. Creep parameters are obtained based on BP network back analysis, as shown in Table 4.

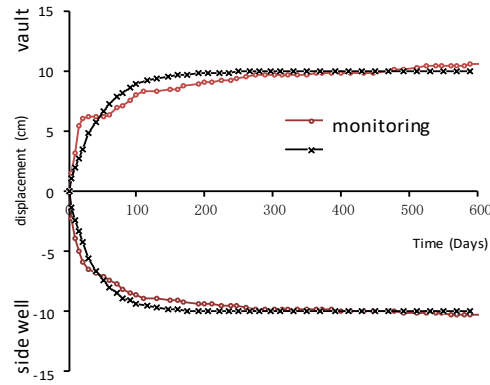


Fig. 14. - Comparison between Measured Data and Calculated Value (K1+675)

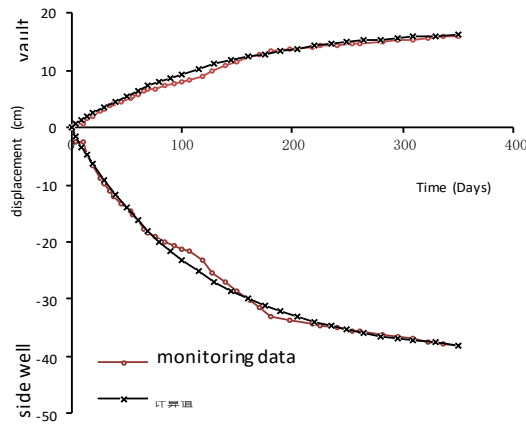


Fig. 15. - Comparison between Measured Data and Calculated Value (K1+760)

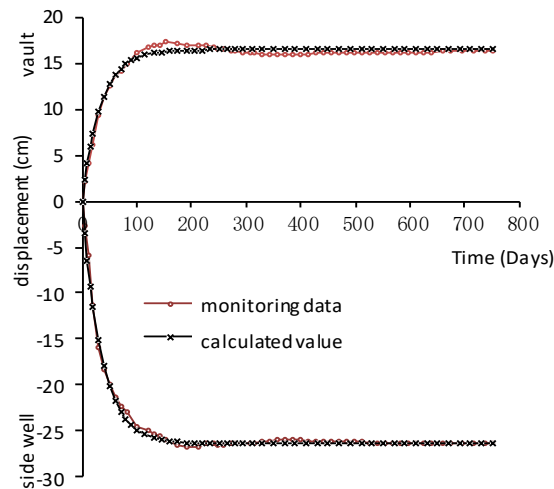


Fig. 16. - Comparison between Measured Data and Calculated Value (K2+665)

Tab. 4. - Model Parameters

location	$G^k(\text{MPa})$	η^k (MPa Day)	k	w_1
K1+675	1426	52083	0.12	2.93
K1+760	575	72337	0.30	4.15
K2+665	691	23726	0.36	5.37

4. CONCLUSION

According to classic three-parameter H-K damage model (generalized Kelvin model), it will be difficult to determine unit range of model parameter attenuation in the large-scale numerical calculation if model parameters are set to tem-dependent attenuation. Therefore, this paper proposes a three-parameter damage model subject to model parameter attenuating with strain increase and gives an attenuation equation respectively for parameters in the first, second and third stage of creep deformation. In addition, strain threshold ε_{thr} is introduced. ε_{thr} is the strain generated when the rock stress is equal to long-term strength. When the rock strain is smaller than the threshold, only the first and second stage of creep deformation will occur. When the rock strain is larger than the threshold, the accelerated creep deformation will occur. Influences of attenuation parameters k , w_1 , w_2 and v on the creep deformation are respectively discussed in the example. The three-parameter H-K damage model is used for numerical calculation of finite difference method.

FLAC3D and deformation features of soft rock with time under high ground stress are described based on diversion tunnel project of Jinping Hydropower Station. It shows high compliance of calculated value with measured data, indicating the three-parameter damage model has high adaptability. Model parameters are obtained by back analysis based on measured data and BP neural network. The model proposed in this paper can properly describe three stages of soft rock creep deformation, reasonably interpret large deformation of soft rocks and predict the large deformation to some extent.

REFERENCES

- [1] Yang, C.H., Daemen, J.J., Yin, J.H., 1999. Experimental investigation of creep behavior of salt rock. *International Journal of Rock Mechanics and Mining Sciences*. 36(3), 233-242.
- [2] Li, Y.S., Xia, C.C., 2000. Time-dependent tests on intact rocks in uniaxial compression. *International Journal of Rock Mechanics and Mining Sciences & Geomechanics Abstracts*. 37(3), 467-475.
- [3] Enrico, M., Tsutomu, Y., 2001. A non-associated viscoplastic model for the behaviour of granite in triaxial Compression. *Mechanics of Materials*. 33(5), 283-293.
- [4] Shalabi, F.I., 2004. FE analysis of time-dependent behavior of tunneling in squeezing ground using two different creep models. *Tunnel. Underground Space Technol.* 20, 271-279.
- [5] Tsai, L.S., Hsieh, Y.M., Weng, M.C., Huang, T.H., Jeng, F.S., 2008. Time-dependent deformation behaviors of weak sandstones. *Int. J. Rock Mech. Mining Sci.* 45, 144-154.
- [6] Sun, J., 1999. *Rheological behavior of geomaterials and its engineering application*. Beijing: China Architecture and Building Press.

- [7] Itasca Consulting Group, 1997. *FLAC3D, Fast Lagrange Analysis of Continua in 3 Dimensions*, Version 3.0, User Manual. Minneapolis.
- [8] Guan, Z.C., Jiang, Y.J., Yoshihiko, T., Huang, H.W., 2007. A new rheological model and its application in mountain tunnelling. *Tunnelling and Underground Space Technology*. 23(3), 292-299.
- [9] Pellet, F., Hajdu, A., Deleruyelle, F., Besnus, F., [10] 2005. A viscoplastic model including anisotropic damage for the time dependent behaviour of rock. *Int. J. Numer. Anal. Meth. Geomech.* 29 (9), 941–970.
- [10] Shao, J., Chau, K., Feng, X., 2006. Modeling of anisotropic damage and creep deformation in brittle rocks. *Int. J. Rock Mech. Min. Sci.* 43 (4), 582–592.
- [11] Bhandari, A., Inoue, J., 2005. Continuum damage mechanics for hysteresis and fatigue of quasi-brittle materials and structures. *Int. J. Numer. Anal. Meth. Geomech.* 29 (11), 1087–1107.
- [12] Goodman, R.E., 1989. *Introduction to Rock Mechanics*, second ed. Wiley, New York.
- [13] Ahmad, F., Farshad, M.T., Ahmadreza, H., Arash, V., 2010. Analytical solution for the excavation of circular tunnels in a visco-elastic Burger's material under hydrostatic stress field. *Tunnelling and Underground Space Technology*. 25(4), 297-304.
- [14] Guan, Z.C., Jiang, Y.J., Yoshihiko, T., 2008. Rheological parameter estimation for the prediction of long-term deformations in conventional tunneling. *Tunnelling and Underground Space Technology*. 24(3), 250-259.
- [15] Fang, K.T, Ma, C.X, 2001. *Orthogonal design and uniform design*. Beijing: Science Press.

OPTIMIZATION OF THE TEMPERATURE CONTROL SCHEME FOR ROLLER COMPACTED CONCRETE DAMS BASED ON FINITE ELEMENT AND SENSITIVITY ANALYSIS METHODS

Huawei Zhou^{1,2}, Yihong Zhou^{1,2,3*}, Chunju Zhao^{2,3}, Zhipeng Liang⁴

- ¹ School of Water Resources and Hydropower Engineering, Wuhan University, Wuhan, 430072, China
- ² College of Hydraulic and Environmental Engineering, China Three Gorges University, Yichang, 443002, China
- ³ Hubei Key Laboratory of Construction and Management in Hydropower Engineering, China Three Gorges University, Yichang 443002, China
- ⁴ College of Mechanical and Power Engineering, China Three Gorges University, Yichang, 443002, China

ABSTRACT

Achieving an effective combination of various temperature control measures is critical for temperature control and crack prevention of concrete dams. This paper presents a procedure for optimizing the temperature control scheme of roller compacted concrete (RCC) dams that couples the finite element method (FEM) with a sensitivity analysis method. In this study, seven temperature control schemes are defined according to variations in three temperature control measures: concrete placement temperature, water-pipe cooling time, and thermal insulation layer thickness. FEM is employed to simulate the equivalent temperature field and temperature stress field obtained under each of the seven designed temperature control schemes for a typical overflow dam monolith based on the actual characteristics of a RCC dam located in southwestern China. A sensitivity analysis is subsequently conducted to investigate the degree of influence each of the three temperature control measures has on the temperature field and temperature tensile stress field of the dam. Results show that the placement temperature has a substantial influence on the maximum temperature and tensile stress of the dam, and that the placement temperature cannot exceed 15 °C. The water-pipe cooling time and thermal insulation layer thickness have little influence on the maximum temperature, but both demonstrate a substantial influence on the maximum tensile stress of the dam. The thermal insulation thickness is significant for reducing the probability of cracking as a result of high thermal stress, and the maximum tensile stress can be controlled under the specification limit with a thermal insulation layer thickness of 10 cm. Finally, an optimized temperature control scheme for crack prevention is obtained based on the analysis results.

KEYWORDS

Concrete dam, Temperature control parameters, Finite element method, Numerical simulation, Sensitivity analysis

INTRODUCTION

During the construction of a roller compacted concrete (RCC) dam, large quantities of concrete are employed to form a monolithic mass concrete structure [1]. Heat generated by the hydration of cement leads to a rising temperature in the dam body, and, owing to its massiveness, several years are required for a concrete dam to attain a stable temperature after a peak temperature

is reached [2]. Such variations in the temperature of concrete dams usually lead to cracking, which greatly impacts the quality and safety of concrete dams. To address this substantial problem, various concrete temperature control measures, such as water-pipe cooling, concrete pre-cooling, surface heat preservation, and thin layer placement, are typically employed in the construction process. Nevertheless, thermal cracking still often occurs due to an ineffective combination of these measures.

Numerous studies have been published regarding temperature control scheme design for RCC dams based on numerical analysis methods, which have proven to be effective for the verification of temperature control measures. Chen et al. [3] developed a three-dimensional (3-D) finite element relocating mesh method (TDFERMM) for conducting computational simulation analysis of the temperature and thermal stress distributions in an RCC dam. Malkawi et al. [4] conducted a coupled thermal-structural analysis using both a two-dimensional (2-D) and a 3-D finite element method (FEM). Xie et al. [5] simulated different types of impervious layers with different thicknesses using TDFERMM for the third grader RCC dam. A 2-D finite element code was developed and verified by Noorzai et al. [6] for the thermal and structural analysis of RCC dams. Jaafar et al. [7] studied the impact of concrete placement schedules on the thermal response of RCC dams with a finite element based computer code. Chen et al. [8] developed a thermal algorithm based on the composite element method (CEM) for massive concrete structures containing lift joints. Teixeira et al. [9] conducted computational studies using a hybrid finite element formulation for cement hydration in concrete structures. Su et al. [10] calculated the temperature stress for high RCC arch dams mixed with MgO based on FEM. Gaspar et al. [11] proposed a probabilistic thermal model to propagate the uncertainties of some of the physical properties of RCCs, and analyzed the influence of parameters with random characteristics. These studies have mainly focused on improving the simulation method employed for computing the temperature and temperature stress fields of concrete dams, whereas few scholars have considered methods for achieving an optimized employment of various temperature control measures.

Various temperature control measures have been widely used in the construction process of concrete dams for crack prevention, although the degrees to which the different measures influence the temperature and temperature stress fields are not equivalent. Establishing the governing factors by which these measures influence the temperature control effect is critical for achieving an effective combination of these measures in the construction organization design and management of a concrete gravity dam.

In this study, a sensitivity analysis of three temperature control measures, selected as concrete placement temperature, water-pipe cooling time, and thermal insulation layer thickness, is performed based on 3-D FEM simulation of the equivalent temperature field and temperature stress field of a model dam. Seven temperature control schemes are defined according to variations in three temperature control measures: concrete placement temperature, water-pipe cooling time, and thermal insulation layer thickness. The purpose of this study is to determine the degree to which the three temperature control measures influence the temperature and temperature tensile stress fields of an RCC dam, and to obtain an optimized temperature control scheme for crack prevention.

METHODOLOGY

Calculation theory of temperature field

The equation of heat conduction considering the effect of water-pipe cooling can be expressed as follows [12].

$$\frac{\partial T}{\partial \tau} = a \left(\frac{\partial^2 T}{\partial x^2} + \frac{\partial^2 T}{\partial y^2} + \frac{\partial^2 T}{\partial z^2} \right) + \frac{Q}{c\rho} \quad (1)$$

where T is the concrete temperature ($^{\circ}\text{C}$); τ is the time (h); a is the thermal diffusivity coefficient of concrete, given as $a = \lambda / c\rho$ (m^2/h); Q is the heat generation rate per volume ($\text{kJ}/(\text{m}^3 \cdot \text{h})$); λ is the thermal conductivity coefficient ($\text{kJ}/(\text{m} \cdot \text{h} \cdot ^{\circ}\text{C})$); c is the specific heat ($\text{kJ}/(\text{kg} \cdot ^{\circ}\text{C})$); and ρ is the material density (kg/m^3).

The initial condition is given in terms of standard Cartesian coordinates and time as follows.

$$T(x, y, z, 0) = T_0(x, y, z) \tag{2}$$

Three boundary conditions must be considered during calculation of the temperature field. The first boundary condition is that the surface temperature is a function of time, which is given as

$$T_s(\tau) = f(\tau) \tag{3}$$

The second boundary condition is that the heat flux across the surface is a known function of time, and is given as

$$-\lambda \frac{\partial T}{\partial n} = f(\tau) \tag{4}$$

The adiabatic boundary condition $\partial T / \partial n = 0$ can be obtained by substituting $f(\tau) = 0$ into Eq. (4).

The third boundary condition is that the concrete surface is in contact with the air, which can be expressed as

$$-\lambda \frac{\partial T}{\partial n} = \beta(T_s - T_a) \tag{5}$$

where $T_0(x, y, z)$ is the initial temperature; T_s the surface temperature; n is the surface external normal direction; β is the surface conductance ($\text{kJ}/(\text{m}^2 \cdot \text{h} \cdot ^{\circ}\text{C})$); and T_a is the air temperature.

Calculation theory of temperature stress with FEM

The elastic modulus and creep of concrete both vary with respect time, and an incremental method is used with τ divided into a series of time increments $\Delta\tau_n$ ($\Delta\tau_n = \tau_n - \tau_{n-1}$, $n=1, 2, 3, \dots$), as shown in Figure 1.

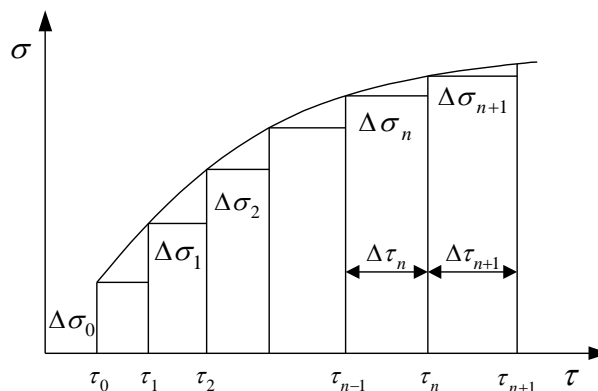


Fig. 1. - Incremental method for calculating the stress

The total strain increment within $\Delta\tau_n$ is

$$\{\Delta\varepsilon_n\} = \{\varepsilon(t_n)\} - \{\varepsilon(t_{n-1})\} = \{\Delta\varepsilon_n^e\} + \{\Delta\varepsilon_n^c\} + \{\Delta\varepsilon_n^T\} + \{\Delta\varepsilon_n^s\} + \{\Delta\varepsilon_n^s\} \tag{6}$$

where $\{\Delta\varepsilon_n^e\}$ is the elastic strain increment; $\{\Delta\varepsilon_n^c\}$ is the creep strain increment; $\{\Delta\varepsilon_n^T\}$ is the temperature strain increment; $\{\Delta\varepsilon_n^g\}$ is the self-grown volume strain increment; and $\{\Delta\varepsilon_n^s\}$ is the dry-shrinkage strain increment.

The relationship between $\{\Delta\sigma_n\}$ and $\{\Delta\varepsilon_n^e\}$ is

$$\{\Delta\sigma_n\} = [D]\{\Delta\varepsilon_n^e\} \quad (7)$$

where $\{\Delta\sigma_n\}$ is the stress increment within the time $\Delta\tau_n$; $[D]$ is the elastic matrix.

The following equation can be obtained by substituting Eq. (6) into Eq. (7).

$$\{\Delta\sigma_n\} = [D](\{\Delta\varepsilon_n\} - \{\Delta\varepsilon_n^c\} - \{\Delta\varepsilon_n^T\} - \{\Delta\varepsilon_n^g\} - \{\Delta\varepsilon_n^s\}) \quad (8)$$

The element nodal forces increment $\{\Delta F_n\}$ within $\Delta\tau_n$ is given by

$$\{\Delta F_n\} = \iiint [B]^T \{\Delta\sigma_n\} dx dy dz \quad (9)$$

where $\{\Delta F_n\}$ is the nodal force increment within $\Delta\tau_n$; $[B]$ is the transition matrix of element; T represents the transpose of the matrix. Substituting $\{\Delta\sigma_n\}$ expressed by Eq. (8) and $\{\Delta\varepsilon_n\} = [B]\{\Delta\delta_n\}$ into the above equation yields

$$\iiint [B]^T [D] [B] \{\Delta\delta_n\} dx dy dz = \{\Delta F_n\} + \iiint [B]^T [D] (\{\Delta\varepsilon_n^c\} + \{\Delta\varepsilon_n^T\} + \{\Delta\varepsilon_n^g\} + \{\Delta\varepsilon_n^s\}) dx dy dz \quad (10)$$

where $\{\Delta\delta_n\}$ is the displacement increment of element nodal.

If only considering the temperature load, the following equations are obtained when the exterior loads $\{\Delta F_n\}$ are equal to zero.

$$[K]^e = \iiint [B]^T [D] [B] dx dy dz \quad (11)$$

$$\{\Delta P_n^c\}^e = \iiint [B]^T [D] \{\Delta\varepsilon_n^c\} dx dy dz \quad (12)$$

$$\{\Delta P_n^T\}^e = \iiint [B]^T [D] \{\Delta\varepsilon_n^T\} dx dy dz \quad (13)$$

$$\{\Delta P_n^g\}^e = \iiint [B]^T [D] \{\Delta\varepsilon_n^g\} dx dy dz \quad (14)$$

$$\{\Delta P_n^s\}^e = \iiint [B]^T [D] \{\Delta\varepsilon_n^s\} dx dy dz \quad (15)$$

where $[K]^e$ is the element stiffness matrix; $\{\Delta P_n^c\}^e$ is the nodal load increment due to creep strain; $\{\Delta P_n^T\}^e$ is the nodal load increment due to temperature change; $\{\Delta P_n^g\}^e$ is the nodal load increment due to self-grown volume strain; and $\{\Delta P_n^s\}^e$ is the nodal load increment due to dry-shrinkage strain.

The following overall equilibrium equation can be established.

$$[K]^e \{\Delta\delta_n\}^e = \{\Delta P_n^c\}^e + \{\Delta P_n^T\}^e + \{\Delta P_n^g\}^e + \{\Delta P_n^s\}^e \quad (16)$$

Solution of Eq. (10) yields $\{\Delta\delta_n\}$, and then the stress increment $\{\Delta\sigma_n\}$ can be determined. Such that the total stress at time t_n can be obtained by accumulating stress increments of the time intervals.

$$\{\sigma_n\} = \{\Delta\sigma_1\} + \{\Delta\sigma_2\} + \dots + \{\Delta\sigma_n\} = \sum_{i=1}^n \Delta\sigma_i \quad (17)$$

Sensitivity analysis method

To determine the most sensitive temperature control measures, and to optimize the temperature control scheme, a sensitivity analysis (SA) method is applied in this research as follows.

(1) Selection of influence factors and analysis indicators. Prior to conducting a sensitivity analysis, influence factors that tend to have the greatest impact on the temperature control of a concrete dam should be selected. Three temperature control measures are selected here as influence factors: concrete placement temperature, water-pipe cooling time, and thermal insulation layer thickness. Two distinct evaluations are selected as analysis indicators: the maximum temperature T^{\max} and the maximum tensile stress O^{\max} .

(2) Calculate the sensitivity indicators. The extent to which analysis indicators change owing to changes in the influence factors are taken as sensitivity indicators, where a sensitivity indicator represents the independent influence of each influence factor (IF). The general principle for evaluating the influence of an IF on the temperature control effect is based on the change in T^{\max} (ΔT_{IF}^k) and the change in O^{\max} ($\Delta\sigma_{IF}^k$) of the k -th IF ($k = 1, 2, 3$) according to the following formulas.

$$\Delta T_{IF}^k = \left| \frac{T_i^{\max} - T_j^{\max}}{IF_i^k - IF_j^k} \right| \quad (18)$$

$$\Delta\sigma_{IF}^k = \left| \frac{\sigma_i^{\max} - \sigma_j^{\max}}{IF_i^k - IF_j^k} \right| \quad (19)$$

Here, indices i ($i = 1, 2, 3, 4, 5, 6, 7$) and j ($j = 1, 2, 3, 4, 5, 6, 7$) denote the temperature control schemes that are being compared; T_i^{\max} and T_j^{\max} represent the maximum temperatures obtained for the corresponding temperature control schemes; σ_i^{\max} and σ_j^{\max} represent the maximum tensile stresses obtained for the corresponding temperature control schemes; and IF_i^k and IF_j^k are the values of the k -th IF of the corresponding temperature control schemes.

(3) Analyze the calculation results. The greater the values of ΔT_{IF}^k and $\Delta\sigma_{IF}^k$, the greater the sensitivity level of the corresponding IF .

CASE STUDY

Calculation model and coordinate system

A typical overflow dam monolith of an RCC gravity dam located in southwestern China is taken as the research object. The foundation elevation of the dam is 3,328 m and the crest elevation is 3,421 m. The height of the block is 93 m and the width is 20.5 m. The depth of the dam foundation is 100 m, the length from the heel to the upstream boundary is 100 m, and the length from the toe to the downstream boundary is 100 m as well.

The computational model and coordinate system of the dam monolith are shown in Figure 2. Eight-node hexahedral isoparametric elements are employed in the numerical model. The total number of elements is 20,190. The direction along which the river flows represents the positive x-axis direction and the vertical upward direction represents the positive z-axis direction. The remaining positive y-axis direction is placed to form a standard right-hand Cartesian coordinate system.

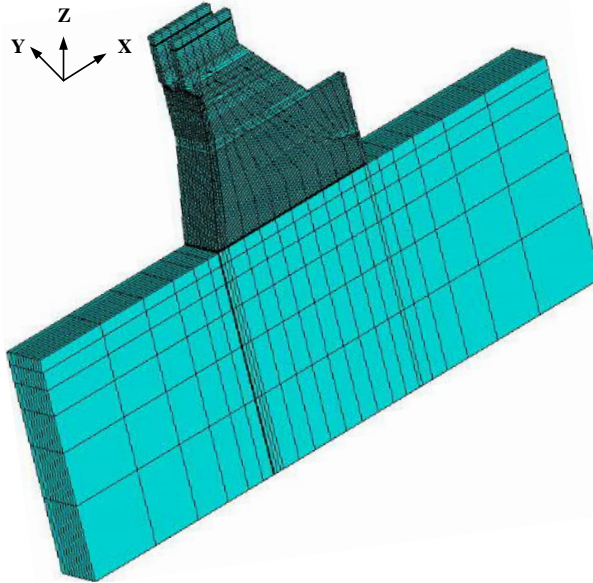


Fig. 2. - 3D FEM model

Basic parameters

Climate and material properties

Table 1 lists the air temperature and rock ground temperature of the dam site employed in the calculations. The annual and monthly average air temperatures are selected to obtain a cosine function that can approximate the air temperature of each day. The air temperature fitting function can be expressed as follows.

$$T_a = 8.6 + 8.5 \times \cos[2\pi \times (\tau - 210) / 365] \quad (20)$$

The material parameters of concrete mixtures for the dam monolith are listed in Table 2. The primary material properties of the dam and rock ground are listed in Table 3. Five types of concrete are employed in the dam block model, as shown in Figure 3. The adiabatic temperature rise of the concrete is a significant parameter in the simulation process. The adiabatic temperature rise of the five types of concrete and the corresponding calculation formulas are listed in Table 4, which were obtained under laboratory conditions. The equivalent surface heat transfer coefficients of the dam with 5 cm and 10 cm thick heat preservation quilts are 9.16 kJ/(m²·h·°C) and 4.38 kJ/(m²·h·°C), respectively.

Tab. 1. - The monthly average temperature values employed in the calculations

Month	1	2	3	4	5	6	7	8	9	10	11	12	Annual average
Air temperature (°C)	-0.7	2.6	6.5	10	12.9	14.5	16.2	15.8	12.9	8.9	3.6	-0.6	8.6
Rock ground temperature (°C)	0.3	4.8	9.8	13.6	17.3	18.8	19.8	19.9	15.8	11.7	5.5	0.2	11.5

Tab. 2. - The material parameters of concrete mixtures

Concrete	Gradation	Water-Cement Ratio	Material Dosage (kg/m ³)							
			Water	Cement	Fly Ash	Sand	Boulder	Mid Stone	Small Stone	
C ₉₀ 20 (distorted concrete)	2	0.45	531	708	472					
C ₉₀ 20 (RCC)	2	0.50	102	102	102	757	0	807	538	
C ₉₀ 15 (RCC)	3	0.53	92	69.4	104.2	691	440	587	440	
C ₉₀ 20 (NC)	3	0.55	125	159.1	68.2	589	433	577	433	
C ₂₈ 40 (NC)	2	0.35	135	318.8	56.3	545	0	801	534	

Tab. 3. - The thermal and structural properties of the dam and rock ground employed in the calculations

Materials		Temperature diffusivity (m ² /h)	Temperature conductivity (kJ/(m·h·°C))	Specific heat (kJ/(kg·°C))	Linear expansion coefficient (10 ⁻⁶ /°C)	Density (kg/m ³)	Standard elastic modulus (GPa)
Concrete	C ₉₀ 20 (distorted concrete)	0.0037	8.18	0.926	9.01	2345	21.4
	C ₉₀ 20 (RCC)	0.0038	8.10	0.921	8.95	2350	22.0
	C ₉₀ 15 (RCC)	0.0038	8.30	0.912	9.06	2400	20.5
	C ₉₀ 20 (NC)	0.0037	8.36	0.955	9.18	2390	23.4
	C ₂₈ 40 (NC)	0.0039	8.55	0.934	9.40	2345	22.0
Rock ground		0.0038	8.10	0.902	8.5	2700	20

Tab. 4. - The adiabatic temperature rises and the corresponding calculation formulas

Concrete	Adiabatic temperature rise of concrete at different ages (°C)								Fitting calculation formulas
	1 d	3 d	5 d	7 d	10 d	14 d	21 d	28 d	
C ₉₀ 20 (distorted concrete)	10.6	15.9	19.2	21.6	24.0	25.5	27.1	27.5	$\theta(\tau) = 30.0d / (d + 2.5)$
C ₉₀ 20 (RCC)	6.0	11.2	14.3	16.3	18.8	20.4	21.5	22.0	$\theta(\tau) = 24.9d / (d + 3.4)$
C ₉₀ 15 (RCC)	4.5	8.6	11.2	13.4	15.6	17.1	18.2	18.8	$\theta(\tau) = 21.8d / (d + 4.3)$
C ₉₀ 20 (NC)	11.5	18.5	22.3	24.5	25.8	26.2	26.7	27.1	$\theta(\tau) = 28.5d / (d + 1.4)$
C ₂₈ 40 (NC)	20.5	29.5	34.1	36.8	37.5	38	38.2	38.4	$\theta(\tau) = 39.7d / (d + 0.8)$

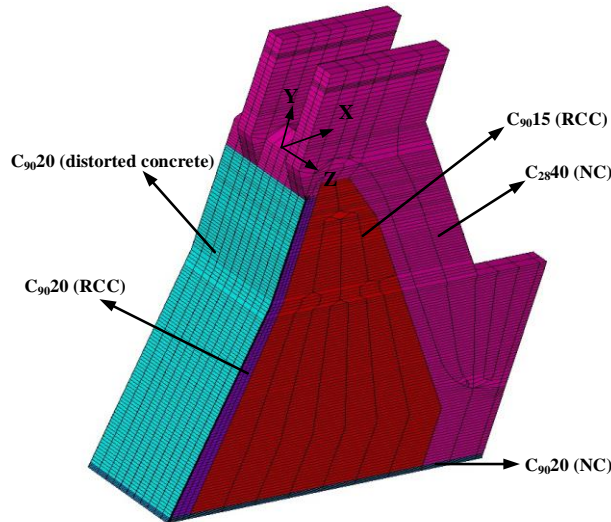


Fig. 3. - Material partition figure of the 3-D FEM dam block model

Temperature control criteria

According to the specification developed in China given in Design Specification for Concrete Gravity Dams (SL319-2005), the allowable temperature stress of concrete under the condition of uniform cooling can be estimated according to the concrete ultimate tensile strain by the following equation:

$$\gamma_0 \sigma \leq \varepsilon_p E_c / \lambda_{d3} \tag{21}$$

where σ is the allowable tensile stress of concrete (MPa); ε_p is the standard value of the concrete ultimate tensile strain; E_c is the standard value of the concrete elastic modulus (GPa); γ_0 is the structure importance coefficient, which is set as 1.0; and λ_{d3} is the structure coefficient under the serviceability limit states, which is set as 1.5.

The detailed parameters and the values of σ for the five types of concrete at a given age are listed in Table 5. The maximum temperature of a concrete dam should be less than or equal to the specification limit of 29 °C.

Tab. 5: Allowable tensile stresses of the five types of concrete

Concrete Parameters	C9020 (distorted concrete)	C9020 (RCC)	C9015 (RCC)	C9020 (NC)	C2840 (NC)
Standard elastic modulus E_c (GPa)	21.4	22.0	20.5	23.4	22.0
Ultimate tensile strain ε_p (10^{-4})	0.88	0.88	0.90	0.78	1.20
Structural or safety coefficient λ_{d3}	1.5	1.5	1.5	1.5	1.5
Allowable tensile stresses σ (MPa)	1.29	1.29	1.40	1.07	1.76

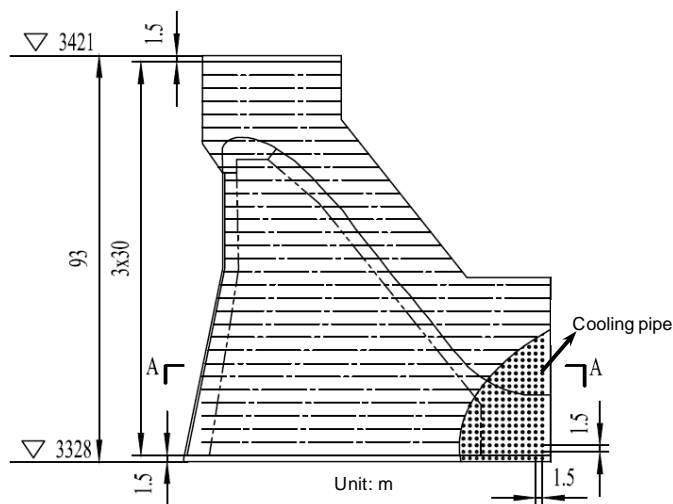
Boundary conditions and calculation schemes

The bottom surface of the rock ground is added the annual average ground temperature load, and it is fully constrained. The upstream and downstream surfaces and left and right surfaces of the rock ground are thermally adiabatic, and are considered in the second boundary condition. Vertical constraints are also applied. The dam surface, which is exposed to air, is regarded as the third boundary condition in this calculation.

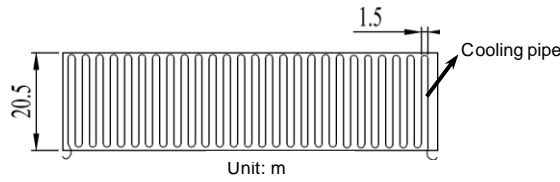
The HDPE pipe was used in this project to cool the concrete. Layout of water cooling pipes is shown in Figure 4. Basic material parameters of the pipe are listed in Table 6. The water temperature is 10 °C for all 7 schemes. Equivalent thermal diffusivity coefficients a' of concrete are used in the calculation process of this study. The equation of a' can be expressed as follows [12]:

$$a' = 1.947(a_1 b)^2 a \tag{22}$$

where $a_1 b$ is the characteristic root of non-metallic cooling pipe which can be obtained from the Table 23-2-1 in the reference [12], a is the thermal diffusivity coefficient of concrete.



(a) Longitudinal profile of the cooling pipes layout



(b) Layout of the cooling pipes in cross section A-A

Fig. 4. - Layout of water cooling pipes

Tab. 6. - Basic material parameters of the HDPE cooling pipe

Parameters	Thermal diffusivity coefficient (W/(m ² ·°C))	Pipe spacing (m×m)	Single pipe length (m)	Diameter (mm)	Thickness of the pipe wall (mm)
Value	≥0.45	1.5×1.5	≤250	32	2

The elastic modulus of different concrete mixtures was not constant during the simulation process. Hyperbolic type function was used to calculate the concrete elastic modulus at any age in this study. The equation can be expressed as follows [12].

$$E(\tau) = E_c \tau / (q + \tau) \tag{23}$$

where τ is the concrete age (d); $E(\tau)$ is the concrete elastic modulus at age τ ; E_c is the standard value of the concrete elastic modulus (GPa); q is a constant.

R is the solar heat absorbed by concrete surface (W/m²); β is the surface conductance (kJ/(m²·h·°C)); α_s is the absorption coefficient, given as 0.65 for concrete surface; S is the solar heat radiation on the concrete surface per unit area per unit time (kJ/(m²·h)).

To analyse the degrees to which the concrete placement temperature, water-pipe cooling time, and thermal insulation layer thickness influence the temperature control effect during the construction of an RCC gravity dam, seven comparison schemes are proposed in this paper, which are listed according to their scheme number in Table 7. The initial placement time is set as July 1 of the first year in the simulation process. 32 lifts are contained and the interval time of adjacent placing layers is 10 d and the lift thickness is 3 m. The total simulation time is 791 d. Because the monthly average air temperature from early October to the end of April of the following year is below 10 °C, the surface heat preservation measure should be applied during this period.

Impact of solar radiation on the concrete temperature equals to air temperature increased ΔT_a , which is given as

$$\Delta T_a = \frac{R}{\beta} = \frac{\alpha_s S}{\beta} \tag{24}$$

where R is the solar heat absorbed by concrete surface (W/m²); β is the surface conductance (kJ/(m²·h·°C)); α_s is the absorption coefficient, given as 0.65 for concrete surface; S is the solar heat radiation on the concrete surface per unit area per unit time (kJ/(m²·h)).

In this study, average β value of five kinds of concrete is adopted. $\beta = (\beta_1 + \beta_2 + \beta_3 + \beta_4 + \beta_5) / 5 = (8.18 + 8.10 + 8.30 + 8.36 + 8.55) / 5 = 8.3$. S is obtained with monitoring equipment, given as $38.3 \text{ kJ}/(\text{m}^2 \cdot \text{h})$. So, an increase in ambient temperature of 3°C is obtained based on Eq. 24. It is used to simulate the influence of solar radiation on the temperature field of the concrete surface during the construction of the RCC gravity dam.

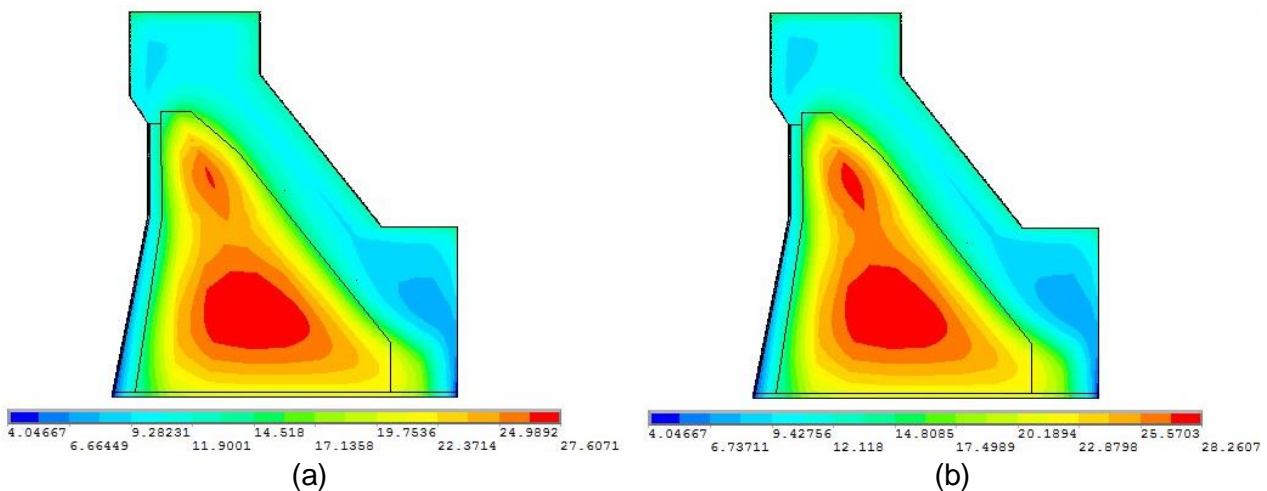
Analysis type I consists of schemes 1, 2, and 3, which are designed for conducting the sensitivity analysis of the placement temperature. Analysis type II consists of schemes 1, 4, and 5, which are designed for conducting the sensitivity analysis of the water-pipe cooling time. Finally, Analysis type III consists of schemes 1, 6, and 7, which are designed for conducting the sensitivity analysis of the thermal insulation layer thickness.

Tab. 7. - Temperature control schemes

Analysis type	Scheme number	Placement temperature ($^\circ\text{C}$)	Water-pipe cooling time (d)	Thermal insulation layer thickness (cm)
I	1	12	15	10
	2	15	15	10
	3	20	15	10
II	1	12	15	10
	4	12	20	10
	5	12	25	10
III	1	12	15	10
	6	12	15	5
	7	12	15	no heat preservation

Results and discussion

As the temperature field and stress field are time-varying values, the final simulation step is selected as typical time in this paper to carry out the sensitivity analysis as follows. Figure 5 shows the temperature contours of the dam block elements on the final simulation step for the seven temperature control schemes.



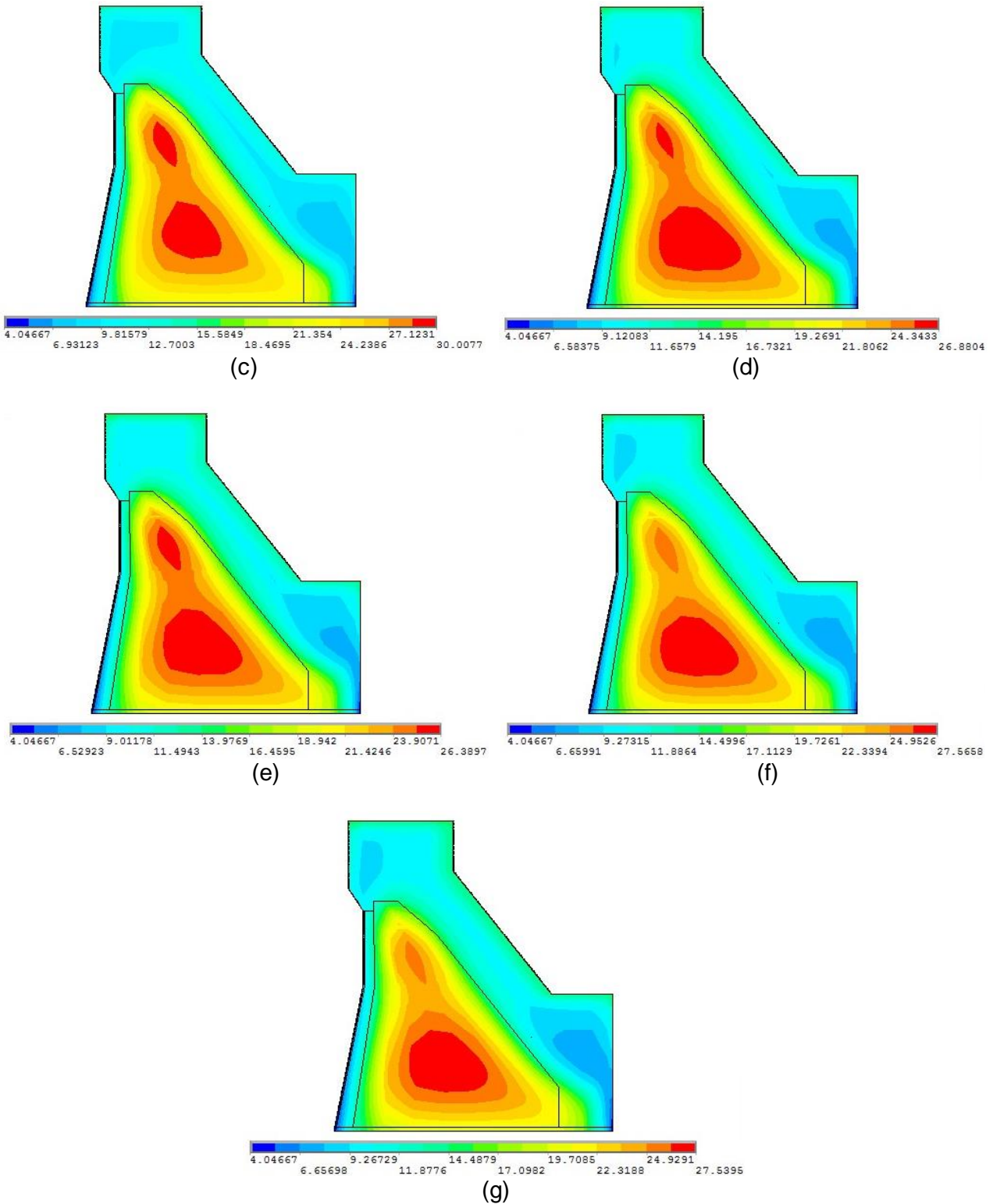


Fig. 5. - Temperature distributions of each temperature control scheme at the final simulation step (unit: °C): (a) Scheme 1, (b) Scheme 2, (c) Scheme 3, (d) Scheme 4, (e) Scheme 5, (f) Scheme 6, and (g) Scheme 7.

Sensitivity analysis of placement temperature

Schemes 1, 2, and 3 of Analysis type I employ placement temperatures of 12 °C, 15 °C, and 20 °C, respectively, as shown in Table 7. The water-pipe cooling times and thermal insulation layer thicknesses in these three schemes are fixed at 15 d and 10 cm, respectively.

From the temperature distributions of the dam block elements shown in Figures 5 (a), (b), (c), it can be seen that the maximum temperatures of schemes 1, 2, and 3 at the final simulation step are 27.61 °C, 28.26 °C, and 30.01 °C, respectively. The simulation results are listed in Tables 8. The boldfaced values in the table represent values that exceed the specification limits. When the placement temperature was increased from 12 °C to 15 °C, the maximum temperature of the dam increased by about 0.65 °C and ΔT_{IF}^1 is 0.2167. Meanwhile, the maximum tensile stress increased by about 0.2 MPa and $\Delta \sigma_{IF}^1$ is 0.067. When the placement temperature was increased from 15 °C to 20 °C, the maximum temperature increased by about 1.76 °C and ΔT_{IF}^1 is 0.35, whereas the maximum tensile stress increased by about 0.12 MPa and $\Delta \sigma_{IF}^1$ is 0.24.

The calculation results demonstrate that placement temperatures of 12 °C and 15 °C meet the requirements of temperature and stress control. When the placement temperature is increased to 20 °C, the maximum temperature and tensile stress of the dam block elements both exceed the specification limits.

According to the ΔT_{IF}^1 and $\Delta \sigma_{IF}^1$ values obtained, it can be concluded that the placement temperature has a significant influence on the maximum temperature and tensile stress of the dam, and the placement temperature cannot exceed 15 °C. For safety considerations, the placement temperature should be 12 °C.

Tab. 8. - The maximum temperatures and stresses of the dam model at the final simulation step with different placement temperatures

Scheme number	Placement temperature (°C)	Maximum temperature (°C)	ΔT_{IF}^1 (°C)	Maximum tensile stress (MPa)	$\Delta \sigma_{IF}^1$ (MPa/°C)	Allowable tensile stresses (MPa)
1	12	27.61	—	0.86	—	1.07
2	15	28.26	0.2167	1.06	0.067	1.07
3	20	30.01	0.35	1.18	0.24	1.07

Sensitivity analysis of water-pipe cooling time

Schemes 1, 4, and 5 of Analysis type II employ water-pipe cooling times of 15 d, 20 d, and 25 d, respectively, as shown in Table 7. The placement temperatures and thermal insulation layer thicknesses are fixed at 12 °C and 10 cm, respectively.

From the temperature distribution of the dam block elements shown in Figures 5 (a), (d), and (e), it can be seen that the maximum temperatures of schemes 1, 4, and 5 are 27.61 °C, 26.88 °C, and 26.39 °C, respectively. The simulation and sensitivity analysis results are listed in Table 9. The boldfaced value in the table indicates that the stress exceeds the specification limit. When the water-pipe cooling time was increased from 15 d to 20 d, the maximum temperature of the dam decreased by about 0.73 °C and ΔT_{IF}^2 is 0.146. Meanwhile, the maximum tensile stress increased by about 0.12 MPa and $\Delta \sigma_{IF}^2$ is 0.024. When the water-pipe cooling time was increased from 20 d to 25 d,

the maximum temperature decreased by about 0.49 °C and ΔT_{IF}^2 is 0.098, whereas the maximum tensile stress increased by about 0.14 MPa and $\Delta \sigma_{IF}^2$ is 0.028.

The calculation results show that water-pipe cooling times of 15 d, 20 d, and 25 d all meet the requirements of temperature control. However, the maximum tensile stress of the dam block elements exceeds the specification limit for a water-pipe cooling time of 25 d.

According to the values of ΔT_{IF}^2 and $\Delta \sigma_{IF}^2$ obtained, it can be concluded that the water-pipe cooling time has a small influence on the maximum temperature, but has a substantial influence on the maximum tensile stress of the dam, and the water-pipe cooling time cannot exceed 20 d.

Tab. 9: The maximum temperatures and stresses of the dam model and value of sensitivity indicators with different water-pipe cooling times

Scheme number	Water-pipe cooling time (d)	Maximum temperature (°C)	ΔT_{IF}^2 (°C/d)	Maximum tensile stress (MPa)	$\Delta \sigma_{IF}^2$ (MPa/d)	Allowable tensile stresses (MPa)
1	15	27.61	—	0.86	—	1.07
4	20	26.88	0.146	0.98	0.024	1.07
5	25	26.39	0.098	1.12	0.028	1.07

Sensitivity analysis of thermal insulation layer thickness

Schemes 1, 6, and 7 of Analysis type III employ thermal insulation layer thicknesses of 10 cm, no heat preservation (i.e., 0 cm), and 5 cm, respectively. The placement temperature and water-pipe cooling time are fixed at 12 °C and 15 d, respectively.

From the temperature distributions of the dam block elements shown in Figures 5(a), (f), and (g), it can be seen that the maximum temperatures of the three schemes are 27.61 °C, 27.54 °C, and 27.57 °C, respectively. The boldfaced values in the table represent stress values that exceed the specification limit. When the thermal insulation layer thickness was decreased from 10 cm to no heat preservation, the maximum temperature of the dam decreased by about 0.07 °C and ΔT_{IF}^3 is 0.014. Meanwhile, the maximum tensile stress increased by about 1.37 MPa and $\Delta \sigma_{IF}^3$ is 0.614. When the thermal insulation layer thickness was increased from no heat preservation to 5 cm, the maximum temperature increased slightly and ΔT_{IF}^3 is 0.001, whereas the maximum tensile stress decreased by about 0.85 MPa and $\Delta \sigma_{IF}^3$ is 0.381. The simulation and sensitivity analysis results are listed in Table 10.

The calculation results show that thermal insulation layer thicknesses of 10 cm, no heat preservation, and 5 cm all meet the requirements of temperature control. However, with a thermal insulation layer thickness of 5 cm or no heat preservation, the maximum tensile stress of the dam block elements exceeds the specification limit.

According to the values of ΔT_{IF}^3 and $\Delta \sigma_{IF}^3$ obtained, it can be determined that the thermal insulation layer thickness has a small influence on the maximum temperature, but has a substantial influence on the maximum tensile stress of the dam, and the thermal insulation layer thickness should be 10 cm for surface heat preservation.

Tab. 10: The maximum temperatures and stresses of the dam model and value of sensitivity indicators with different thermal insulation layer thicknesses

Scheme number	Thermal insulation layer thickness (cm)	Maximum temperature (°C)	ΔT_{IF}^3 (°C/ cm)	Maximum tensile stress (MPa)	$\Delta \sigma_{IF}^3$ (MPa/cm)	Allowable tensile stresses (MPa)
1	10	27.61	—	0.86	—	1.07
6	5	27.57	0.001	1.38	0.381	1.07
7	no heat preservation	27.54	0.014	2.23	0.614	1.07

CONCLUSIONS

An effective combination of temperature control measures is critical in the construction organization design of an RCC gravity dam. Based on the above study, the following conclusions can be drawn.

(1) An optimized temperature control scheme can be obtained by coupling 3-D FEM simulation of the thermal and stress distributions of concrete dams with the proposed sensitivity analysis method.

(2) The placement temperature has a substantial influence on the maximum temperature and tensile stress of the dam, and the placement temperature cannot exceed 15 °C.

(3) The water-pipe cooling time has a small influence on the maximum temperature, but has a substantial influence on the maximum tensile stress of the dam, and the water-pipe cooling time cannot exceed 20 d.

(4) The thermal insulation layer thickness has a small influence on the maximum temperature, but has a substantial influence on the maximum tensile stress of the dam. With a thermal insulation layer thicknesses of 10 cm, the maximum tensile stress can be controlled under the specification limit.

Taken together, according to the findings of the present study, the concrete temperature control measures are most effective when the placement temperature is 12 °C, the water-pipe cooling time is 20 d, and the thermal insulation layer thickness is 10 cm.

ACKNOWLEDGEMENTS

This research was supported by the National Natural Science Foundation of China (Grant No. 51479103), the Open Foundation of Key Laboratory of Hydropower Engineering Construction and Management of Hubei Province (Grant No. 2014KSD06). The authors thank the reviewers for useful comments and suggestions that helped to improve the paper. The authors would like to thank LetPub (www.letpub.com) for its linguistic assistance during the preparation of this manuscript.

REFERENCES

- [1] Jing X. Y., Zhou W., Liu J. and Chang, X. L., 2013. Dynamic control measures of concrete temperature in rapid construction of high RCC dams. *Engineering Journal of Wuhan University*, vol. 46: 99-104.
- [2] Zhang L., Liu Y., Li B. Q., Zhang G. X. and Zhang S. T., 2015. Study on Real-Time Simulation Analysis and Inverse Analysis System for Temperature and Stress of Concrete Dam. *Mathematical Problems in Engineering*, vol. 2015: 1-8.
- [3] Chen Y. L., Wang C. J., Li S. Y., Wang R. J. and He J., 2001. Simulation analysis of thermal stress of RCC dams using 3-D finite element relocating mesh method. *Advances in Engineering Software*, vol. 32: 677-682.
- [4] Malkawi A. I. H., Mutasher S. A. M. and Qiu T. J., 2003. Thermal-Structural Modeling and Temperature Control of Roller Compacted Concrete Gravity Dam. *Journal of Performance of Constructed Facilities*, vol. 17: 177-187.
- [5] Xie H. W., Chen Y. L., 2005. Determination of the type and thickness for impervious layer in RCC dam. *Advances in Engineering Software*, vol. 36: 561-566.
- [6] Noorzai J., Bayagoob K. H., Thanoon W. A. and Jaafar M. S., 2006. Thermal and stress analysis of Kinta RCC dam. *Engineering Structures*, vol. 28: 1795-1802.
- [7] Jaafar M. S., Bayagoob K. H., Noorzai J. and Thanoon W. A. M., 2007. Development of finite element computer code for thermal analysis of roller compacted concrete dams. *Advances in Engineering Software*, vol. 38: 886-895.
- [8] Chen S. H., Su P. F and Shahrou I., 2011. Composite element algorithm for the thermal analysis of mass concrete: Simulation of lift joint. *Finite Elements in Analysis and Design*, vol. 47: 536-542.
- [9] Teixeira De Freitas J. A., Cuong P. T., Faria R. and Azenha M., 2013. Modelling of cement hydration in concrete structures with hybrid finite elements. *Finite Elements in Analysis and Design*, vol. 77: 16-30.
- [10] Su H. Z., Li J. Y. and Wen Z. P., 2014. Evaluation of Various Temperature Control Schemes for Crack Prevention in RCC Arch Dams During Construction. *Arabian Journal for Science and Engineering*, vol. 39: 3559-3569.
- [11] Gaspar A., Lopez-Caballero F., Modaressi-Farahmand-Razavi A. and Gomes-Correia A., 2014. Methodology for a probabilistic analysis of an RCC gravity dam construction. Modelling of temperature, hydration degree and ageing degree fields. *Engineering Structures*, vol. 65: 99-110.
- [12] Zhu B. F., 2012. *Thermal Stresses and Temperature Control of Mass Concrete*, Beijing: China WaterPower Press.

GROUTING METHODS FOR THE REHABILITATION AND REINFORCEMENT OF MASONRY STRUCTURES DAMAGED BY CRACKS

Čejka Tomáš¹, Radek Zigler¹, Kroftová Klára², Markéta Šmidtová¹

- ¹ CTU in Prague, Faculty of Civil Engineering, Department of Building Structures, Prague, Thákurova 7, Czech Republic; cejka@fsv.cvut.cz, zigler@fsv.cvut.cz, smidtmr@fsv.cvut.cz
- ² CTU in Prague, Faculty of Civil Engineering, Department of Architecture, Prague, Thákurova 7, Czech Republic; klara.kroftova@fsv.cvut.cz

ABSTRACT

The article sums up the requirements for historic masonry structures whose reinforcement is based on the grouting technology application, the grouting implementation procedure in relation to the extent, type and size of masonry damage. Special focus is put on grouting agents and requirements for their characteristics.

KEYWORDS

masonry structure, historic structure, grouting, requirements

INTRODUCTION

The restoration, reconstruction and rehabilitation of historic and heritage buildings presently put great emphasis on such conservation and restoration methods which are not associated with significant damage and irreversible interventions in the historical matter. These requirements can be, to a certain extent, met by reinforcement methods using composites based on high-strength carbon or aramid and glass fibres and resin, or polymer-modified cement mixes (for specially modified fabrics) applied usually on the surface or in layers close to the surface. Another group of methods meeting the requirements above are grouting methods, which preserve or restore the original, i.e. initial characteristics of historical materials and structures. By the application of these methods, the structure - damaged by degradation processes of mostly chemical nature (at elevated moisture contents) or mechanical effects causing cracks and degrading the structure of historical materials and structures - is stabilized (its structural integrity regained).

MASONRY GROUTING METHODS, REQUIREMENTS FOR GROUTING AGENTS AND MIXES

Composites based on high-strength fibres (carbon, aramid, glass) and suitable adhesives (resin, special polymer-modified cement mixes) can be applied in the form of all-surface fabrics placed on cleaned surfaces of masonry structures damaged by tensile or shear cracks. Another option, mainly for local cracks, is the application of partial composite strips covering tensile or shear cracks in the appropriate direction. These issues have been the subject of extensive research and its results have been published e.g. [1 - 5] (Figure 1).

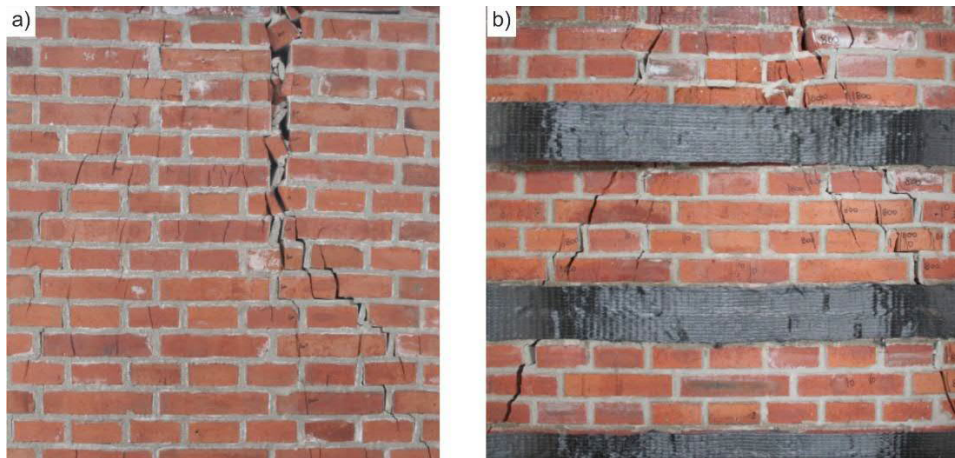


Fig. 1. - a) damaged masonry, b) masonry with carbon strips

The damage of compressed masonry pillars and walls is usually manifested by the appearance of tensile cracks whose direction corresponds to the pattern of compression trajectories and is the consequence of the low strength of masonry and its components in tension, ranging in the interval of 5 to 12 % of the strength of the masonry and its components in compression. The rehabilitation of masonry, in these cases, mostly consists of the prevention of the development of tensile cracks by the application of transverse masonry reinforcement or pre-stress. In the case of totally insufficient load-bearing capacity of masonry in compression, the masonry load-bearing capacity in compression is increased by adding a reinforcing (additional) construction. The extent and the method of masonry rehabilitation depend on the condition, type and extent of masonry damage.

The grouting of primarily multi-layer masonry for the purpose of improving its physical and mechanical characteristics is a relatively old and widely used irreversible method of masonry rehabilitation [6, 7].

The type and dimensions of cracks (inclined and vertical cracks to a width of ca 20 mm) which can be grouted, the position of grouting and inspection holes (the distance of verification holes from the crack being 150 – 300 mm), the composition of grouting mixes and grouting pressures for brick masonry damaged by earthquakes are prescribed in [8]. The verification of the masonry grouting quality is described in [9, 10]. Depending on changes in surface emissivity and potential changes in the temperature field (during the chemical reaction of grouting mixes with masonry components), thermal imaging can be used for the verification of grouting depths [9]. Ultrasound tomography helps to verify the grouting effectiveness (grouting depth) based on changes in density [10].

Masonry damaged by degradation processes can be reinforced by suitable grouting (using epoxy resin, cement, lime suspension, etc.) depending on the extent and type of masonry damage. Damaged surface layers or plasters can be reinforced by repetitive multiple coatings (sprayed) of lime water (in the case of less damaged masonry). The respective masonry rehabilitation must be assessed in terms of water vapour diffusion to avoid moisture entrapping in the masonry.

The basic grouting substances are mixes based on cement or hydraulic lime with additives such as brick dust, pozzolana, clays, etc. [6, 7, 11 - 14]. The additives are used to reduce the necessary amounts of cement, modify the major characteristics of grouting substances – rheological, volume changes, strength, grout ability [6, 7, 11, 12, 14 - 17]. An important and demanding step is the design of the grouting mix with high grout ability at low pressures to allow the penetration of the mix into the masonry, filling all cracks, caverns, cavities and filling or partially filling the pore system of original materials, forming a bond between the original materials and grouted mortar and taking into account the “roughness” effect of masonry units’ surfaces [12, 14, 15, 18].

Special emphasis in the restoration and reconstruction of historic and heritage buildings has been recently put on the usage of traditional materials based e.g. on lime, pozzolana, metakaolin.

Experimental research has pointed out that the usage of metakaolin or pozzolana led to the extension of the hardening time; after reducing the cement amount by 30% the bond between the masonry units and the grouting mix shows satisfactory characteristics [16] and low-strength masonry manifests a relatively higher increase in strength than high-strength masonry after grouting [16]. Experimental research [7] compared commercially available lime-based grouting agents. The growth in resistance and mechanical characteristics of masonry depends on the strength of the bond between the grouting mix and masonry.

The masonry made up of high-quality masonry units with insufficiently load-bearing mortar can be strengthened by pressure grouting, so-called micro grouting using epoxy- or polyurethane resin-based mortar injected through boreholes into each bed joint (under a pressure of ca 0.5 MPa). Prior to grouting, pillars may e.g. be fitted with temporary formwork of hardened paper impregnated repeatedly with alkali silicate.

Local cracks (active, passive), both tensile and shear, require securing to prevent their further development and propagation. Provided the masonry in the vicinity of local cracks is not damaged or poor-quality, so-called “**stitching**” can be performed using e.g. steel ties of round bars with higher-quality periodic surfaces (\varnothing 14 mm to \varnothing 18 mm), or ties of specially profiled high-strength steel (e.g. Helifix), properly anchored to the load-bearing masonry. When applying this method, the possibility of the appearance of new cracks must be carefully considered, particularly in the places of tie anchorage. The ties must be arranged perpendicularly to the passing crack with a sufficient overlap of e.g. min. 0.5 m on each side. The distance between the ties, which usually ranges from 0.3 to 0.6 m, will decrease to prevent further crack propagation at both ends and in the area of the largest crack width. Progressive and, at the same time, non-invasive methods include the stitching of cracks with composite strips based on high-strength fibres (carbon, aramid, glass) and suitable adhesives (resins, special polymer-modified cement mixes) (Figure 2).

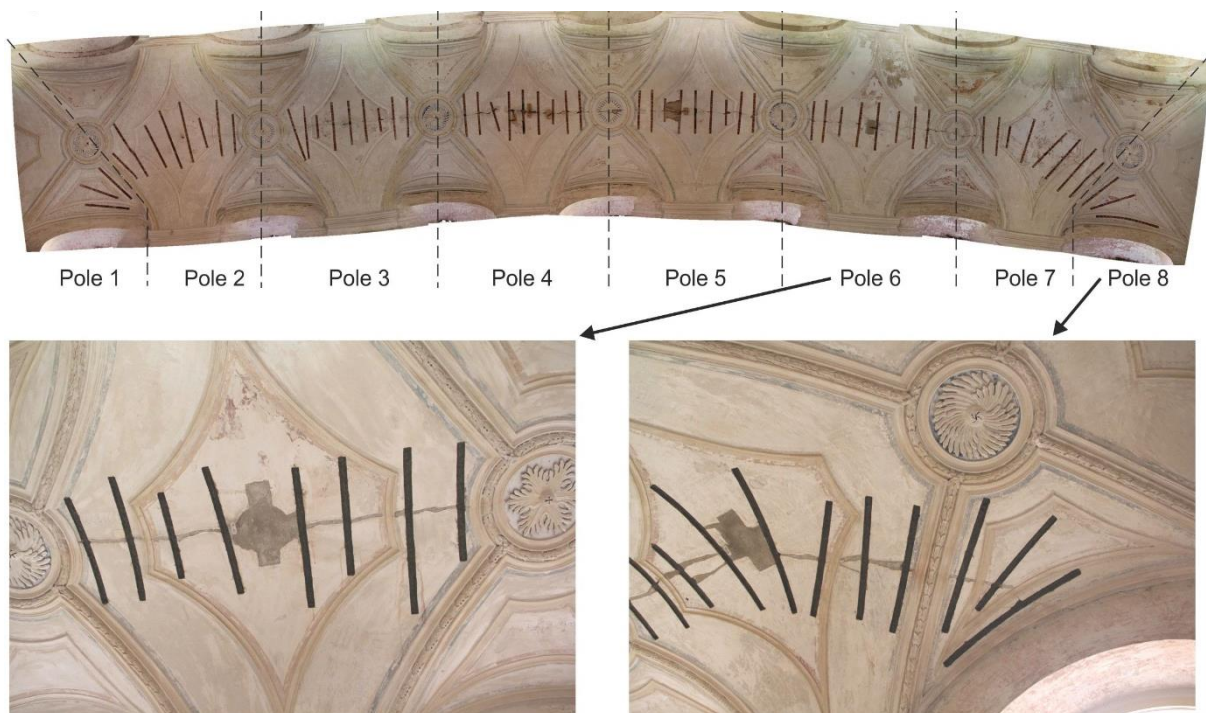


Fig. 2. - Stitching cracks on a barrel vault

After the mounting of ties in grooves and cleaning the crack with compressed air, pressure grouting is performed or deep cementing of the crack with an expansive cement mix or mortar is done. The ties must be protected from corrosion by proper backfilling of the groove and covered by

a layer of polymer-modified cement mortar sufficient in thickness and successively overlaid with a mesh and plaster.

Masonry damaged by a cluster of active cracks can be rehabilitated by overall crack grouting, preceded by deep cementing of cracks with larger width with a pressure caulking gun. The grouting of cracks up to the width of 2 mm is performed with low viscosity resins under the pressure of minimally 20 to 40 kPa. The grouting of cracks 2 to 4 mm in width is performed after their previous wedging with a mixture of resin with a filler (fine silica sand) at the pressure of 20 to 60 kPa. Cracks wider than 4 mm are filled with cement mortar, or two-stage grouting with cement mortar and resin is performed. Active cracks must be clamped with ties or pins of stainless steel before grouting, or in the case of large-scale cracking the masonry structure must be braced by steel tie rods of reinforcing steel or hoop steel embedded in bed joints, by prestressing cables embedded and anchored in a continuous groove min. 50 mm in depth, or by prestressed carbon lamellae. The cluster of active cracks rehabilitated in this way is successively covered over the whole surface with a composite based on the special fabrics and a polymer-modified cement mix.

Masonry damaged by tensile or shear cracks can be reinforced after previous wedging and local grouting of cracks wider than 2 mm by inserting steel rods (e.g. helibar) or carbon composite strips anchored by a special polymer-modified cement mix and, after flushing joints and cracks, by overall micro grouting of the masonry. To ensure the effectiveness, steel sections or composite strips based on high-strength fibers 50-60 mm in width, must be embedded deeper, and, as appropriate and depending on the extent of masonry damage, reinforced on both sides.

Masonry grouting is performed down under the protection of hardened, sufficiently compact, properly anchored and strong sheathing. Grouting pipes (packers) mounted in drilled holes are sealed by gypsum or rapid-setting mortar. The selected distance of boreholes is usually from 0.5m to 1m (exceptionally up to 2m) so that all cracks are properly filled depending on the permeability of the damaged structure and the extent of damage. Grouting can be applied only to structures which have sufficient tensile strength and are permeable (in relation to the pore system and grouting pressure) to carry the internal tensile stress induced by grouting and let the grouting agent penetrate into the masonry structure.

Prior to masonry grouting, damaged surface layers must be removed. To avoid the bleeding of suspension on the surface of a rehabilitated wall the wall surface must be properly sealed or a new sheathing plaster must be put on before grouting. The choice of the grouting procedure (single-phase, multiple-stage), the grouting agent composition and consistency depend on the masonry condition. Grouting can be complemented by e.g. reinforced plaster (gunite) anchored to the masonry by reinforcing ties, pins, etc. In numerous cases, grouting mostly helps to restore damaged masonry by filling in cavities, voids and joints between masonry units and thus to increase its load-bearing capacity. Grouting of little damaged, compact masonry, as a rule, does not significantly increase its load-bearing capacity (having relatively little effectiveness). The design of static masonry grouting can be based on the WTA 4-3-98 directive.

Cracks to a width of 1 mm are rehabilitated by epoxy resins without fillers. The temperature of the structure must be minimally +5 °C (varying for different manufacturers, but +5°C is the minimum). The cracks must be cleared of impurities, grease, dust and damaged parts. The grouting agent must comply with the requirements for low viscosity (being applicable at a grouting pressure of 20 ÷ 40 kPa), long-time workability in liquid state and fast hardening to prevent the infiltration of the grouting agent into the structure, low shrinkage, low dependence on moisture and alkalinity of the environment. The holes for grouting ca Ø 10 to 15 mm are 500 mm apart for crack widths of up to 1 mm. Other requirements include limited reactivity with metals, absence of health hazards, good adhesion, high tensile strength, potential modification of the modulus of elasticity, non-permeability, durability and dilatometric properties similar to the grouted masonry.

Cracks over 1 mm are grouted with a mixture of resin and a filler (e.g. silica flour with a max. grain size of 0.1 mm in amounts of 20 to 40 %). Prior to grouting, cracks must be wedged, sealed on the surface and grouting packers mounted. The holes for grouting ca Ø 10 to 15 mm are 600 ÷

1000 mm apart for crack widths of over 1 mm. The grouting pressure is ca 20 ÷ 60 kPa, the grouting time of one borehole is usually shorter than 20 minutes.

Cement suspensions (paste, cement milk, cement mortars with lime addition for grouting cavities, or with an admixture lowering viscosity and retarding hardening) can be used for cracks larger than 2 mm.

Density of boreholes: 2 ÷ 4 boreholes \varnothing 20 ÷ 30 mm/m², borehole depth 2/3 to 4/5 of masonry thickness, grouting pressure 50 ÷ 150 kPa. Larger cracks (over 2 mm) must be jointed on the surface before grouting. The grouting time of one borehole at a masonry thickness of 0.9 ÷ 1.2 m is approx. 30 minutes.

The rehabilitation of heritage buildings can be performed with so-called grouting anchors consisting of a steel pin of adequate length of stainless steel with a periodic surface (e.g. 2 m in length, \varnothing 12 mm, in a hole \varnothing 36 mm) mounted in bored holes and grouted with cement suspension (of e.g. Portland cement, w/c = 0.7) or special mixes based on polymers, resins, etc.

Prior to masonry **grouting**, damaged surface layers must be removed. To avoid the bleeding of suspension on the surface of a rehabilitated wall the wall surface must be properly sealed or a new sheathing plaster must be put on before grouting. The choice of the grouting procedure (single-phase, multiple-stage), the grouting agent composition and consistency depend on the masonry condition. Grouting can be complemented by e.g. reinforced plaster (gunite) anchored to the masonry by reinforcing ties, pins, etc.

Stone masonry of historic buildings of less massive and water-absorbing stones can be rehabilitated by micro grouting using epoxy resin (e.g. CHS EPOXY 1000 and 2000, or their 1:1 mixes). Prior to **overall grouting**, the masonry surface is sealed with e.g. a sheathing plaster. The grouting mix is injected into the masonry at a pressure of ca 0.2 MPa by grouting pipes 12 to 15 mm in diameter distributed in a checkerboard pattern over the whole surface of the rehabilitated masonry or divided into sections (where you always proceed from the lower section to the upper one) 0.5 m to 1.0 m apart. The grouting mix must fill in all cavities, cracks and also penetrate into the structure of porous masonry units and mortar.

In **strip grouting**, the grouting boreholes are distributed in vertical and horizontal strips approx. 1 m in width, at a mutual axial distance of 4 to 6 m. The boreholes in the strips are arranged in a checkerboard pattern, 0.5 m to 1.0 m apart. The depth of single-sided boreholes is 2/3 to 3/4 of the masonry thickness, in double-sided boreholes usually 1/3 of the wall thickness. The depth of the boreholes, the grouting procedure (single-phase, multiple-stage) and the grouting pressure must be specified based on the material and masonry condition.

The compressive strength of grouted masonry depends on the amount and quality of the grouting mix penetrated into the masonry.

The choice of the **grouting agent**, its consistency and composition depend on the width of cracks, porosity, mineralogical and chemical composition of the binder or masonry units and the degree of overall masonry degradation. Grouting can only be applied to stabilised masonry and cracks (passive cracks, cracks secured by reinforcement, braced or clamped masonry). The principal characteristics of the grouting agent include rapid setting and hardening, viscosity, strength, stability in the grouting phase, thixotropy, consistency, physical and mechanical properties and durability. A high-quality grouting design further includes the design of grouting packers and pumps, packer distribution and the depth of holes. Structures with higher moisture contents can be grouted with cement milk (mixture) or epoxy resin, while polyurethane and acrylic resin substances (gels) are used for the grouting of cracks which allow undesirable water condensation.

- **Cement suspensions** are less suitable due to their high viscosity (low stability during grouting – fast sedimentation and premature clogging of cracks smaller in width occurs), low tensile strength after hardening, low adhesion and greater shrinkage (adhesion or the cement filling in the cracks fails). Improved characteristics are added by suspensions of fast-bonding cements with a greater proportion of solid gypsum-free clinker (suitable for the rehabilitation of historic buildings with high moisture contents). The grouting cement

mix ($w : c = 1 : 1$ up to $3 : 1$) is injected into boreholes $\varnothing 30$ to 40 mm to the depth of ca $2/3$ of the masonry wall at the pressure of 0.5 to 1.2 MPa. The grouting mortar used for filling larger cracks ($c : p = 1 : 3$ up to $1 : 5$, $w = 0.5$ to 0.8) hardens in 5 to 15 hours, or in 3 to 5 hours when hardening accelerators are used.

Research into the effectiveness of cement suspensions used for the grouting of masonry with poor load-bearing capacity has manifested that the grouting cement substance fills the cracks and cavities in the masonry, improves the masonry unit's contact with mortar and thus produces a visible improvement of its strength. The investigation of cavity and crack filling after grouting can be made with radar or ultrasonic devices.

- **Epoxy resins** reach the required characteristics by the right selection of monomers, setting agents and the hardening procedure, accelerating admixtures, internal plasticisers, modifiers, fillers and extenders. They belong to the most suitable grouting mixes for the rehabilitation of damaged masonry and concrete structures.
- **Polyester resins** are characterised by low viscosity and relatively easy hardening reactions. Their disadvantage is greater shrinkage (ca 5% of volume) and lower adhesion to concrete and other building materials.
- **Polyurethane resins** possess high penetration abilities and are mostly used for the reinforcement of mortar in masonry joints, for increasing the load-bearing capacity of masonry.

STRENGTHENING OF MULTI-LAYER HISTORICAL MASONRY BY GROUTING

Grouting is often used for the reinforcement of multi-layer (three-layer) historical masonry composed of two "sheathings" and an inner core. The failure of multi-layer masonry in compression occurs by increasing the distance of layers in the transverse masonry section [11]. Using a grouting mix based on hydraulic lime does not cause layer separation under loading as this mix homogenises the masonry. Using a grouting mix based on hydraulic lime or cement and hydraulic lime increases the tensile strength of masonry [11]. The experimental verification of the reinforcement of multi-layer (three-layer) masonry by grouting manifested that by adding little amounts of cement to the grouting mix a significant increase in the strength of the fresh mix is produced. The grouting mix of hydraulic lime – pozzolana – cement in a $1:0.7:0.3$ ratio developed a strength twice higher compared to the grouting mix based on lime [6, 15]. The replacement of cement by brick dust has a positive effect on rheological properties, volume changes and strength [6]. Based on experimental verifications, empirical formulae for the prediction of grouted masonry strength were prepared [15]. At the same time, the effect of the water-cement ratio on strength for mixes based on cement and hydraulic lime was verified. After 6 months, the specimens composed of cement – lime – pozzolana with a w/c ratio of 0.8 showed the highest strength, while lower strength was found in the specimens based on hydraulic lime with a w/c ratio of 0.8 and the lowest strength in specimens on the same basis with a w/c ratio of 0.7 [15].

SPECIAL GROUTING MIXES FOR GROUTING DEGRADED MASONRY

Special grouting mixes with *Sporosarcina Pasteurii* bacteria, which positively affect the setting and hardening process of lime in degraded masonry were verified in China [19]. Modified mortar shows higher tensile strength and higher resistance to cyclic loading than traditional mortar. According to [13], the differences in compressive strength after multi-layer masonry grouting are not that significant if a grouting mix based on hydraulic lime or cement is used. Experimental research [14] confirmed the positive effect of grouting based on cement and hydraulic lime on the compressive strength of masonry, diagonal (transverse) compressive strength of masonry, the modulus of elasticity in compression (E) and in shear (G) of masonry with the growth of the above characteristics

of up to 10 % pointing out the effect of the quality of the bond between the grouting agent and original masonry units on the mechanical and physical characteristics of masonry.

Research into the rehabilitation and reinforcement of multi-layer masonry [20] revealed that masonry reinforcement with GFRP tie rods passing through the entire wall thickness in combination with masonry grouting with a mix based on lime had the greatest effectiveness with an average increase in the masonry compressive strength by up to 71%. The research also verified the failure mechanism when a displacement occurs between the outer and the inner masonry layer and a dominant vertical tensile and shear crack gradually arises.

EXPERIMENTAL RESEARCH

The NAKI DG16P02M055 project is presently in the preparation phase of research into the strengthening of historical brick, stone and mixed masonry using the grouting technology with a special focus on the reinforcement of masonry damaged by cracks due to seismic effects, including the reinforcement of masonry by grouting and by composites based on high-strength fibres and adhesives. Figure 3 presents the scheme of a masonry test piece and the designed grouting procedure. The test pieces will be “wrapped” in sealing sludge to prevent the grouting agent from escaping. The grouting boreholes are designed to pass through the maximum number of bed joints.

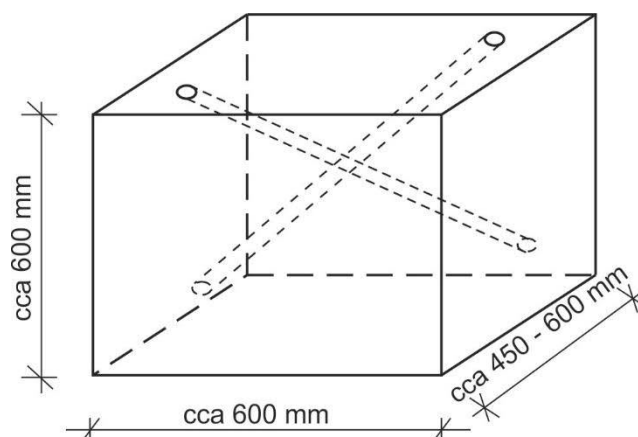


Fig. 3. - Scheme of experimental masonry specimen and proposed method of consolidation grouting

CONCLUSION

Based on a literature search study, the article sums up some principles for the grouting procedure, the grouting agents used, including some limiting and recommended requirements.

ACKNOWLEDGEMENTS

The article was written with support from the NAKI DG16P02M055 project "Research and development of materials, processes and techniques for restoration, preservation and strengthening of historic masonry structures, surfaces and systems for preventive care of heritage buildings exposed to anthropogenic and natural risks" of the Ministry of Culture of the Czech Republic.

REFERENCES

- [1] Witzany, J., et al. Strength Assessment of Historic Brick Masonry. *Journal of Civil Engineering and Management*. 2016, 22(2), s. 224-233. ISSN 1392-3730.

- [2] Witzany, J., Zigler, R. a Kroftová, K. Strengthening of compressed brick masonry walls with carbon composites. *Construction and Building Materials*. 2016, 112s. 1066-1079. ISSN 0950-0618. Dostupné z: <http://www.sciencedirect.com/science/article/pii/S0950061816303130>
- [3] Witzany, J. a Zigler, R. Stress State Analysis and Failure Mechanisms of Masonry Columns Reinforced with FRP under Concentric Compressive Load [online]. *Polymers*. 2016, 8(5), s. 1-25. ISSN 2073-4360. Dostupné z: <http://www.mdpi.com/2073-4360/8/5/176>
- [4] Witzany, J. a Zigler, R. Failure mechanism of compressed reinforced and non-reinforced stone columns. *Materials and Structures*. 2015, 48(5), s. 1603-1613. ISSN 1359-5997. Dostupné z: <http://link.springer.com/article/10.1617%2Fs11527-014-0257-z>
- [5] Witzany, J., et al. The application of carbon composites in the rehabilitation of historic baroque vaults [online]. *Polymers*. 2015, 7(12), s. 2670-2689. ISSN 2073-4360. Dostupné z: <http://www.mdpi.com/2073-4360/7/12/1540>
- [6] Papayianni, Ioanna a Vasiliki Pachta. Experimental study on the performance of lime-based grouts used in consolidating historic masonries. *Materials and Structures* [online]. 2015, 48(7), 2111-2121 [cit. 2016-04-18]. DOI: 10.1617/s11527-014-0296-5. ISSN 1359-5997.
- [7] Luso, Eduarda a Paulo B. Lourenco. Experimental characterization of commercial lime based grouts for stone masonry consolidation. *Construction and Building Materials* [online]. 2016, 102, 216-225 [cit. 2016-04-18]. DOI: 10.1016/j.conbuildmat.2015.10.096. ISSN 09500618.
- [8] City LA DBS. Crack repair of unreinforced masonry walls with grout injection. Information bulletin/ Public – building code reference NO.: Effective: 01-01-2014, DOCUMENT NO.: P/BC 2014-056
- [9] Peřina, Zdeněk, Boris Plšek a Marie Wolfová. Verification of Range of Chemical Grouting of Masonry by Non-Destructive Method Using Infrared Thermography. *Advanced Materials Research* [online]. 2014, 923, 191-194 [cit. 2016-04-18]. DOI: 10.4028/www.scientific.net/AMR.923.191. ISSN 1662-8985.
- [10] Jorne, Fernando, Fernando M.A. Henriques a Luis G. Baltazar. Evaluation of consolidation of grout injection with ultrasonic tomography. *Construction and Building Materials* [online]. 2014, 66, 494-506 [cit. 2016-04-18]. DOI: 10.1016/j.conbuildmat.2014.05.095. ISSN 09500618.
- [11] Vintzileou, Elizabeth a Androniki Miltiadou-Fezans. Mechanical properties of three-leaf stone masonry grouted with ternary or hydraulic lime-based grouts. *Engineering Structures* [online]. 2008, 30(8), 2265-2276 [cit. 2016-04-18]. DOI: 10.1016/j.engstruct.2007.11.003. ISSN 01410296.
- [12] André Filipe Melo de Almeida Figueiredo. Injection grouts for ancient masonry – adherence study. Extended abstract
- [13] Sayed Hemed. Grouting of multiple leaf-masonry walls: Application on some islamic historical monuments in Cairo, Egypt. Article in *International Journal of conservation Science*, Volume 3, Issue 4, October-December 2012: 275-288, ISSN: 2067-533X
- [14] Mojmir Uranjek, Roko Žarnić, Violeta Bokan-Bosiljkov, Vlatko Bosiljkov. Seismic resistance of stone masonry building and effect of grouting. *GRAĐEVINAR 66 (2014) 8, 715-726*, DOI: 10.14256/JCE.1031.2014
- [15] Kalagri, A., A. Miltiadou-Fezans a E. Vintzileou. Design and evaluation of hydraulic lime grouts for the strengthening of stone masonry historic structures. *Materials and Structures* [online]. 2010, 43(8), 1135-1146 [cit. 2016-04-18]. DOI: 10.1617/s11527-009-9572-1. ISSN 1359-5997.
- [16] Adami, Chryssi-Elpida a Elizabeth Vintzileou. Interventions to historic masonries: Investigation of the bond mechanism between stones or bricks and grouts. *Materials and Structures* [online]. 2008, 41(2), 255-267 [cit. 2016-04-18]. DOI: 10.1617/s11527-007-9235-z. ISSN 1359-5997.

- [17] Sepulcre-Aguilar, Alberto a Francisco Hernández-Olivares. Assessment of phase formation in lime-based mortars with added metakaolin, Portland cement and sepiolite, for grouting of historic masonry. *Cement and Concrete Research* [online]. 2010, 40(1), 66-76 [cit. 2016-04-18]. DOI: 10.1016/j.cemconres.2009.08.028. ISSN 00088846.
- [18] L. Binda, C. Modena, G. Baronial, S. Abbaneo. Repair and investigation techniques for stone masonry walls. *Construction and Building Materials*, Vol. 11, No. 3, pp. 133-142, 1997. PII: SO950-0618(97)00031-7
- [19] Yang, Zuan a Xiaohui Chenh. A performance study of high-strength microbial mortar produced by low pressure grouting for the reinforcement of deteriorated masonry structures. *Construction and Building Materials* [online]. 2013, 41, 505-515 [cit. 2016-04-18]. DOI: 10.1016/j.conbuildmat.2012.12.055. ISSN 09500618.
- [20] D.V. Oliveira, P.B. Lourenço, E. Garbin, M.R. Valluzzi, C. Modena. Experimental Investigation on the Structural Behaviour and Strengthening of Three-Leaf Stone Masonry Walls. *Structural Analysis of Historical Constructions*, New Delhi 2006.

COMPARATIVE ASSESSMENT OF RICE HUSK ASH, POWDERED GLASS AND CEMENT AS LATERITIC SOIL STABILIZERS

Adebisi Ridwan¹, Taiwo Kanmodi¹ and Olufikayo Aderinlewo¹

¹ *Federal University of Technology, School of Engineering and Engineering Technology, Department of Civil and Environmental Engineering, Akure, P.M.B. 704, Nigeria; adebisiridwanulaikayode@gmail.com, taiwoakanmodi@yahoo.com, oluade2010@gmail.com*

ABSTRACT

This paper compares the stabilizing effects of three different materials, namely: rice husk ash, powdered glass, and cement on the properties of lateritic soil. The basic properties of the lateritic soil were first obtained through colour, moisture content determination, specific gravity, particle size distribution and Atterberg limits tests. Each of the stabilizing materials was then mixed with the lateritic soil in varying percentages of 2.5%, 5%, 7.5%, 10%, 12.5% and 15% by weight of the soil. Thereafter, compaction and California bearing ratio (CBR) tests were carried out on the sample mixes to determine the effects of the materials on the lateritic soil. Chemical tests were also carried out on the samples to determine their percentage oxides composition. The compaction test showed that the highest maximum dry densities (MDD) obtained for the mixed samples were 2.32 g/cm³ (at 2.5% cement addition), 2.28g/cm³ (at 5% powdered glass (PG) addition) and 2.18 g/cm³ (at 5% rice husk ash (RHA) addition) with corresponding optimum moisture contents (OMC) of 10.06%, 14.3% and 12.31% respectively. The CBR tests showed that the CBR values increased in all cases as the materials were added with those of the cement and powdered glass giving the highest values and showing close semblance under unsoaked conditions. The chemical test showed that the significant oxides present in the cement, powdered glass and rice husk ash were CaO (53.60%), SiO₂ (68.45%) and SiO₂ (89.84%) respectively.

KEYWORDS

Stabilizing, Atterberg limits, compaction, California bearing ratio, optimum

INTRODUCTION

Lateritic soils are the most readily available and the most economical construction materials found in many tropical countries. The availability of such soils over vast areas in the tropics and the relative ease of manipulation on road surfaces make their use very economical as low-cost road sub-base and base material for lightly trafficked secondary roads. However, the major problems associated with roads constructed with laterite include cracking of the surface pavement, stripping of the surface and waviness of the pavement surface a few years after construction [1]. Hence, the need to investigate possible sub-base improvement becomes paramount.

In terms of their morphological and chemical properties, laterite is a highly weathered red sub-soil, rich in secondary oxides of iron, aluminium or both and containing large amounts of

quartz and kaolinite which are either hard or capable of hardening when exposed to wetting and drying [2]. Generally, laterite derives its colour from its mineral composition, while the various shades can be identified with various hydrated Iron Oxide content.

Improvement to soils can be achieved through stabilization which involves blending and mixing materials with the soils to either achieve a desired gradation or to make them more stable. This study seeks to comparatively assess the effects of rice husk ash (RHA), powdered glass (PG) and cement on lateritic soil. Cement is the best conventional stabilizer, however, it is expensive. Hence, there is a need to source for alternative stabilizers that are affordable and readily available from materials which would otherwise have been disposed of as waste from industries. These materials constitute a nuisance to the environment and could even be dangerous in the case of the powdered glass which is majorly non-biodegradable. Consequently, these materials are processed into suitable form, added to the soil and the resulting properties are compared to that of the soil containing cement to determine how effective they are as stabilizers.

Recently, industrial wastes have been considered for application in road construction across the world. The use of such materials is based on technical, economic and ecological criteria which are crucial for a country like Nigeria which normally provides a good environment for manufacture and importation of glass materials as well as the production/processing of rice. However, owing to a poor solid waste management system, Nigerian cities are experiencing environmental problems as the rate of solid waste generation has grown beyond the capacity of the authorities concerned. This portends a serious environmental crisis which could be forestalled or mitigated if these waste materials can be developed and suitably utilised in highway construction.

Background Literature

There are two major methods of stabilization namely mechanical and chemical methods. The mechanical methods of soil stabilization involve either compaction or the introduction of graded aggregate materials, fibrous and other non-biodegradable reinforcement to the soil without requiring chemical changes in the soil. The chemical methods involve adding chemicals or other additives to soils which react with or change the chemical properties of the soil thereby improving its engineering properties. Such chemicals include cement, lime, fly ash, bitumen, calcium chloride and resinous materials.

Compaction as a mechanical stabilization method involves artificially increasing the unit weight or density of the soil by applying pressure on it from above thereby expelling air from the soil mass and ultimately decreasing the void ratio. The other methods of mechanical stabilization involve introducing soil reinforcements in the soil such as geo-textiles and engineered plastic mesh which are designed to trap soils and help control erosion, moisture conditions and soil permeability. Likewise, larger aggregates such as gravels, stones and boulders are often introduced where additional mass and rigidity are required to prevent unwanted soil migration or to improve load-bearing properties of the soil.

Research has shown that stabilizing soils with small quantities of insoluble binders like cement, lime and bitumen and other resinous compounds greatly improved their load bearing capacity and water resistance properties which helped to reduce the rate of cracking [3]. In addition, cement stabilization has been shown as the most effective of all the methods of stabilization for the greater range of lateritic soils. However, the cost of cement is on increase. Hence, a lot of effort is being made to identify and develop alternative materials for highway construction and industrial waste products such as waste glass and rice husk are some examples.

Stabilization of soils with rice husk ash (RHA) and powdered glass (PG)

The effects of RHA on cement stabilized laterite soil with respect to compaction characteristics, California bearing ratio (CBR) and unconfined compressive strength (UCS) tests were investigated [4]. The results obtained showed a general decrease in maximum dry density (MDD) and increase in optimum moisture content (OMC), as the RHA content was increased from 2% to 8%. There was also a tremendous improvement in the CBR and UCS with increase in the RHA content at specified cement contents to their peak values at values between 4% and 6% RHA. The UCS values also improved with curing age.

The effects of rice husk ash (RHA) on some geotechnical properties (such as compaction, consistency limits and strength) of a lateritic soil classified as A-2-6 (0) or SW for sub-grade purposes were studied [5]. The RHA contents used were 5%, 7.5%, 10% and 12.5% by weight of the dry soil and the results obtained showed that an increase in RHA content heightened the optimum moisture content but decreased the maximum dry density. It was also observed that an increase in RHA content, reduced plasticity and increased volume stability as well as the strength of the soil. The optimum RHA content observed was at 10%.

Grain-size distribution, consistency, specific gravity, compaction, California bearing ratio (CBR), unconfined compression, direct shear and permeability tests were conducted on lateritic soil treated with up to 20% glass cullet content [6]. The results showed growth in grain sizes resulting in coarser soil, changes in moisture-density relationship, resulting in lower optimum moisture content (OMC) and higher maximum dry density (MDD), an increase in CBR and in unconfined compressive strength (UCS), changes in cohesion-frictional angle relationship resulting in lower cohesion (c) and higher angle of internal friction (Φ) and growth in co-efficient of permeability, k , with increased glass cullet treatment. These results showed an improvement in geotechnical properties, making glass cullet-lateritic soil blend a potentially good highway material and suggesting the suitability of the blend for embankments, structural and non-structural fill and retaining wall backfill.

The stabilizing effect of powdered glass in varying proportions namely 1%, 2%, 5%, 10% and 15% (by weight of the soil) on clay soil was assessed [7]. The compaction test showed that there was an improvement in the maximum dry density values on addition of the powdered glass with corresponding gradual increase up to 5% glass powder content after which it started to decrease at 10% and 15% powdered glass content. The highest CBR values of 14.90% and 112.91% were obtained at 5% glass powder content and 5mm penetration for both the unsoaked and soaked treated samples respectively. The maximum cohesion and angle of internal friction values of 17.0 and 15.0 respectively were obtained at 10% glass powder content

MATERIALS AND METHODS

The materials used in carrying out this study included waste rice husk, waste glass, cement, lateritic soil and water. Glass is a brittle, optically transparent and amorphous non crystalline material. The type of waste glass materials commonly found in the environment are drinking containers and window glass. Most of them are soda-lime glass composed of about 75% silica (SiO_2) plus Na_2O , CaO , and several additives [8].

Rice husk is an organic fibre containing about 75 to 90% organic matter such as cellulose and lignin while the rest of its constituents are mineral components such as silica, alkalis and trace elements. It also contains high amount of ash (about 10 to 20%) [9]. Cement is both an adhesive and cohesive material which is manufactured from a mixture of limestone, clay and shale. The mixture is burnt in a kiln at 1450°C and the resulting clinker is cooled, passed unto the mills where gypsum is added and ground to the cement powder [10]. Lastly, water which is a universal solvent, can be obtained from different sources (such as boreholes and wells) but it must be free

from suspended particles like organic matter and silt which might affect the hydration process of cement.

Collection and processing of materials

The lateritic soil used for this study was collected from a borrow pit located within the Federal University of Technology, Akure, Ondo state, Nigeria at depths ranging between 1.0m to 2.0m. The glass bottles used for this research were sourced from the discarded brown bottles at a petty trader's shop located in Ilesha East local government of Osun state, Nigeria. They were ground and subjected to sieve analysis. The fractions that passed through sieve $212\mu\text{m}$ was used. It was immediately stored in air tight containers to avoid pre-hydration during storage when left in open air.

The rice husk ash (RHA) used in this study was obtained from a local rice milling factory located in Ibadan North local government of Oyo State, Nigeria. It was burnt under normal atmospheric temperature and pressure (open air burning) to obtain the ash which was immediately stored in air tight containers. The rice husk ash was sieved through BS sieve $212\mu\text{m}$ and the fractions passing through the sieve were used throughout the tests. The cement used was ordinary Portland cement (OPC) obtained from a retailer whose shop was located at the Federal University of Technology, Akure, Ondo State, Nigeria. Figure 1 shows samples of laterite, rice husk ash, powdered glass and cement used in that order.



Fig. 1. - Samples of laterite, rice husk ash, powdered glass and cement

Laboratory tests and analysis

The tests carried out to determine the properties of the lateritic soil in its natural form are the particle size distribution, specific gravity and Atterberg limits tests while the tests to determine the effects of the stabilizing materials on the soil include compaction and California bearing ratio tests. Chemical tests were also carried out on the materials to determine their composition.

The Atterberg limits tests were carried out to determine the liquid limit (LL), plastic limit (PL), shrinkage limit (SL) and Plasticity index (PI). These parameters characterise the nature of a soil based on the water content which determines whether it exists in some of the four following states, namely: solid, semi-solid, plastic and liquid states. The compaction test was carried out in a standard proctor mould to determine the optimum moisture contents (OMC) and maximum dry densities (MDD) of the soil samples. The California bearing ratio (CBR) test is the ratio of force per

unit area required to penetrate the soil mass with standard circular piston at the rate of 1.25mm per minute to that required for the corresponding penetration of a standard material (well graded crushed stone).

ANALYSIS AND DISCUSSION OF RESULTS

The stabilizing agents in the lateritic soil were identified through chemical analysis while the soil was classified through the natural moisture content, particle size distribution, specific gravity and the Atterberg limits tests. The effects of RHA, PG and cement on the lateritic soil were assessed through the compaction and the California bearing ratio tests.

Chemical properties

The chemical properties of the materials were obtained by using a Compact Energy Dispersive X-ray Spectrometer and are as shown in Table 1.

Tab 1. - Chemical properties of the sample materials

Component	Concentration (%)		
	Cement	Powdered glass	Rice husk ash
SiO ₂	28.70	68.45	89.84
Al ₂ O ₃	13.50	5.21	8.43
Fe ₂ O ₃	2.27	14.59	16.21
CaO	53.60	13.99	12.17
MgO	2.21	4.50	1.81
Loss on ignition	2.05	9.11	17.78

It was observed that SiO₂ (silica) was the major component present in powdered glass and rice husk ash while CaO was the major component present in cement as a result of lime used in its production. The combined percent composition of SiO₂, Al₂O₃ and Fe₂O₃ in the powdered glass and rice husk ash is more than 70 which shows that they are good stabilizers [11]. However, cement has a distinctly high concentration of CaO which is responsible for its high stabilizing property.

Natural moisture content

Table 2 shows the natural moisture content of the materials used in the study.

Tab. 2. - Specific gravity of sample materials

Sample	Moisture content (%)
Laterite	7.84
Cement	1.12
Powdered glass	0
Rice husk ash	8.29

Specific gravity

Table 3 shows the specific gravity of the materials used in the study.

Tab. 3. - Percentage moisture content of sample materials

Sample	Specific gravity (g/cm ³)
Laterite	2.96
Cement	3.11
Powdered glass	2.24
Rice husk ash	1.34

Atterberg limits tests

The moisture content values obtained under the Atterberg limits tests are shown in Table 4. The liquid limit, plastic limit and plasticity index of the natural soil sample were obtained as 43.89, 41.0 and 2.89% respectively while the shrinkage limit was obtained as 11.02%.

Tab 4. - Liquid limit, plastic limit and shrinkage limit results

Liquid limit					
Test	Number of blows	Mass of wet sample (g)	Mass of dry sample (g)	Moisture (g)	M.C. %
1	40	7.3	5.3	2.0	37.74
2	30	13.5	9.5	4.0	42.11
3	21	10.2	7.0	3.2	45.71
4	14	7.8	5.2	2.6	50.00
Average M.C (%)					43.89

Plastic limit				
Test	Mass of wet sample (g)	Mass of dry sample (g)	Moisture (g)	M.C %
1	1.0	0.70	0.30	45.85
2	1.6	1.15	0.45	39.13
3	1.3	0.93	0.37	38.02
Average M.C (%)				41.00

Shrinkage limit				
Test	Initial length (L ₀) (cm)	Final length (L ₁) (cm)	Shrunked length (cm)	Shrinkage limit (%)
1	14.1	12.7	1.4	11.02

Particle size distribution

Table 5 shows the details of the particle size distribution analysis of the lateritic soil with the corresponding percentages retained on and passing through each of the sieves. Figure 2 shows the particle size distribution curve indicating that the soil comprises of 32% silt fraction and 68% sand fraction. It can be observed that the percentage passing through the no. 200 sieve (0.075mm) was 41.7% which was more than 30% indicating the soil is composed of silt and clay. Using the liquid limit, plastic limit and plasticity index values of 43.89%, 41% and 2.89%, the soil is classified as A-5 (with 'fair to poor' drainage characteristic) [12]. Hence, the soil needs to be stabilized.

Tab. 5. - Particle Size Distribution Analysis

Diameter (mm)	Mass retained (g)	% retained	% passing
14	0	0	100
9.5	2.6	0.5	99.5
4.75	33.4	6.7	92.8
2.36	56.7	11.3	81.5
1.7	29.7	5.9	75.6
1.18	43.0	8.6	67.0
0.6	38.1	7.6	59.9
0.5	24.3	4.9	54.5
0.425	2.9	0.6	53.9
0.212	39.3	7.9	46.0
0.150	12.0	2.4	43.6
0.075	9.7	1.9	41.7
Pan	1.6	0.3	0

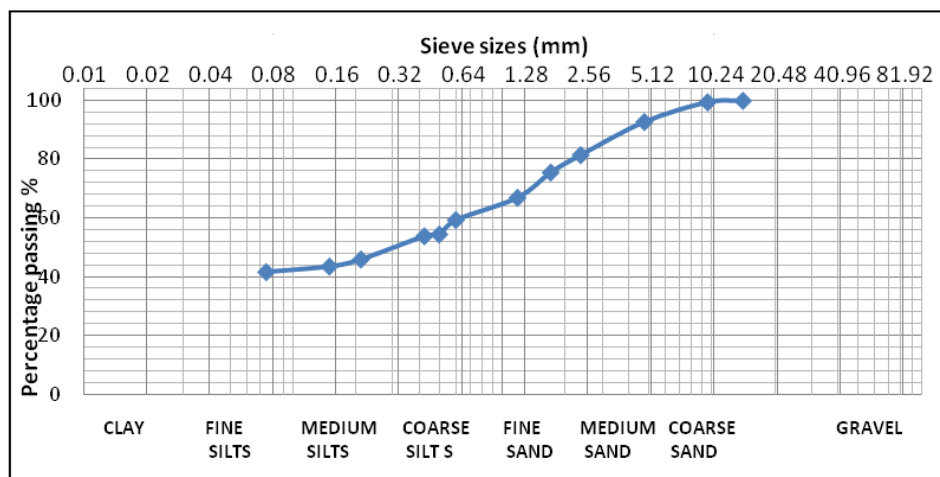


Fig. 2. - Particle Size Distribution chart for the lateritic soil

Compaction test

Compaction tests were carried out on the lateritic soil with and without the additives. The MDD and OMC of the soil in its natural form before stabilization were 2.24g/cm³ and 11.65% respectively as shown in Figure 3. Each of the additives was added to the soil in varying percentages of 2.5%, 5%, 7.5%, 10%, 12.5% and 15% by weight of the soil. Figures 4, 5 and 6 show the compaction curves for the lateritic soil with RHA, PG and cement content which indicate

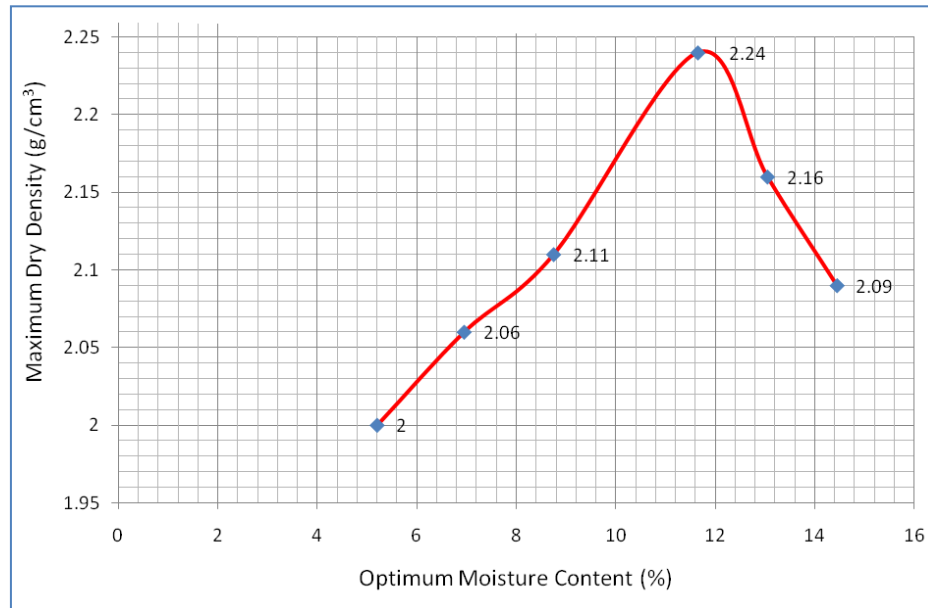


Fig. 3 - Compaction curve for the natural lateritic soil

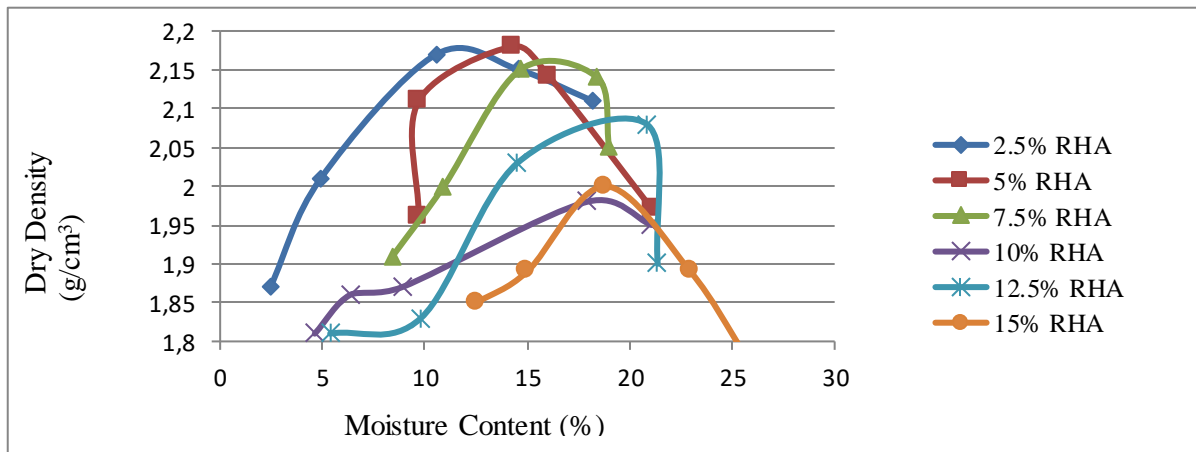


Fig. 4. - Compaction curves for the soil with varying RHA content

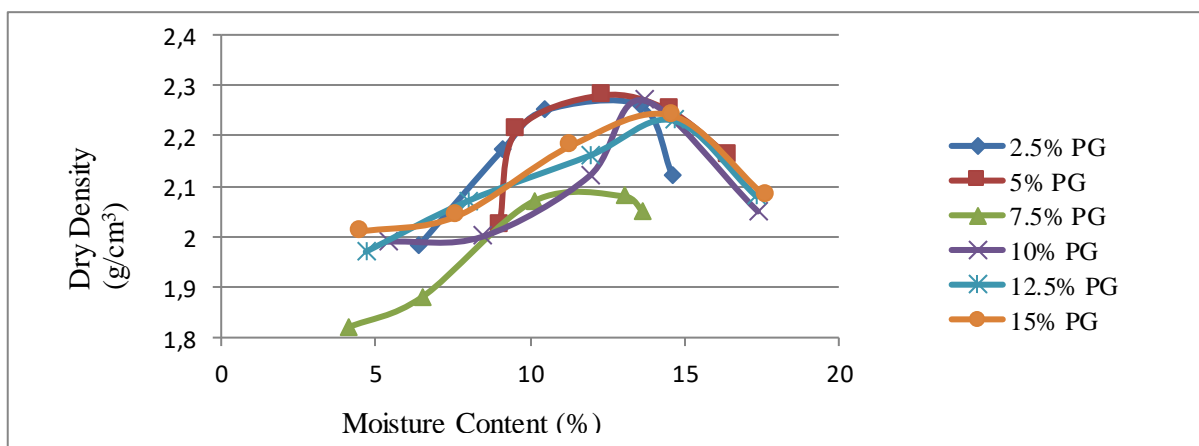


Fig. 5. - Compaction curves for the soil with varying PG content

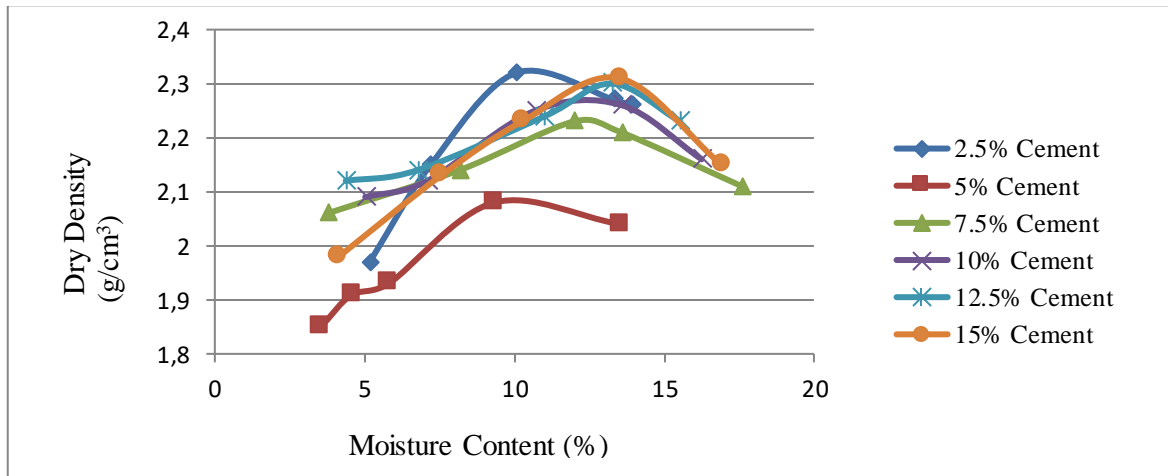


Fig. 6. - Compaction curves for the soil with varying cement content

that the MDD of the soil increased from a value of 2.24g/cm³ in the natural form to 2.28 g/cm³ (OMC = 12.31%) at 5% powdered glass content and to 2.32 g/cm³ (OMC = 10.06%) at 2.5% cement content. However, it dropped to its maximum value of 2.18 g/cm³ (OMC = 14.3%) at 5% RHA content.

California bearing ratio

Figures 7 and 8 show the unsoaked and soaked CBR graphs for the lateritic soil containing the additives in varying percentages of 2.5%, 5%, 7.5%, 10%, 12.5% and 15% by weight of the soil.

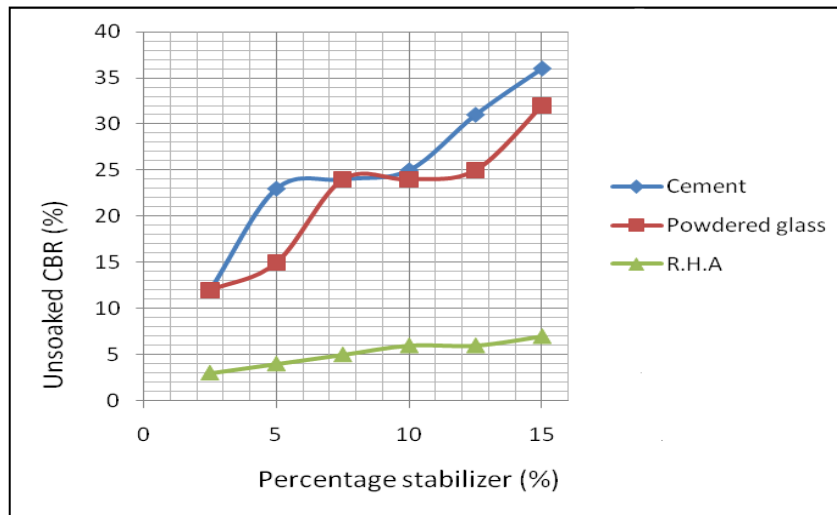


Fig. 7. - Unsoaked CBR curves for the soil with varying additives

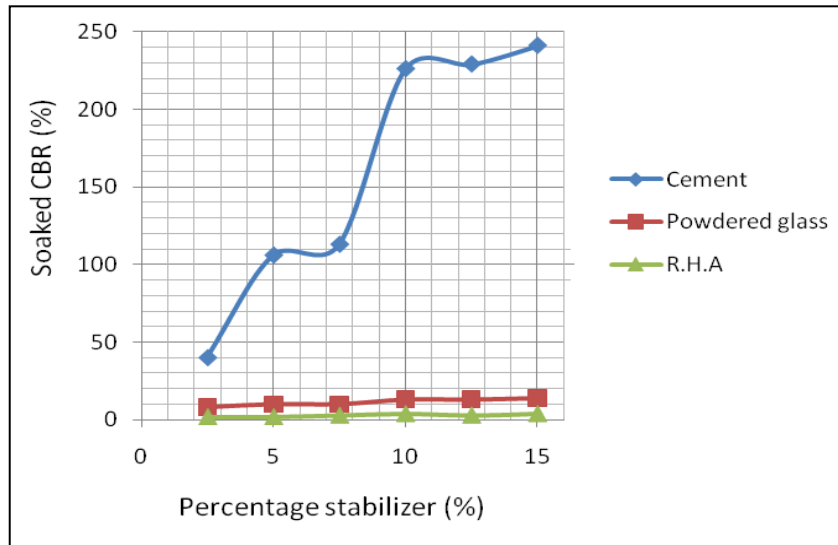


Fig. 8. - Soaked CBR curves for the soil with varying additives

The unsoaked CBR curves show that the values continued to increase as both the cement and powdered glass content were increased likewise the soil containing RHA but only slightly. The explanation for this is that cement has a very high flexural strength which translates to the high strength of the soil-cement mix. In the case of the soil-powdered glass mix, the glass acts as a pozzolana (siliceous or aluminous material) which reacts with calcium hydroxide in the presence of water at room temperature to form insoluble calcium silicate hydrate and calcium aluminate hydrate compounds which possess cementitious properties that strengthen the soil.

It can be also observed that the unsoaked CBR of the natural soil (34%) was exceeded by that of the soil with cement content (36%). In addition, the CBR values of the soil with powdered glass content (with the highest CBR value at 32%) compared favourably with those of the soil containing cement.

The soaked CBR curves show that only the cement additive has very noticeable positive effect on the CBR of the soil with its highest value at 241% which is a sharp contrast to the CBR value of the natural soil at 21%. In this case, the powdered glass and RHA produce barely noticeable positive changes in the CBR of the soil. It appears that the powdered glass loses its strength under soaked conditions.

CONCLUSION

Based on the Atterberg limits test and the particle size distribution analysis, the natural lateritic soil used for the study was classified using the AASHTO soil classification system as A-5 soil. A-5 soils are a group of soils that cannot be used as subgrade material in road construction unless they are stabilized.

The compaction tests show that the maximum dry densities are obtainable for the lateritic soil treated with cement, powdered glass and rice husk ash at OMCs of 10.06%, 14.3% and 12.31% respectively. This will ensure greater strength of the soil as well as ensure that it is less susceptible to changes in moisture content which may lead to swelling and shrinkage.

The CBR tests indicate that the CBR values of the soil treated with cement and powdered glass may further increase on increasing their percentage content beyond 15%. The CBR tests also suggest that powdered glass treated soil will only produce results comparable to cement

treated soils under dry conditions. Hence, powdered glass can be used as an alternative to cement under unsoaked conditions.

REFERENCES

- [1] Morin, W.J. and Todor, P.C. 1975. "Laterite and Lateritic Soils and other Problem Soils of the Tropics". An Engineering Evaluation and Highway Design Study for *United States Agency for International Development*. Vol. 1. Lyon Associates, Baltimore, Maryland.
- [2] Alexander, L.T. and Cady, J.G. 1992. Genesis and Hardening of Laterite Soils. *Technology Bull*, 1: 82-88.
- [3] Ola, S.A. 1983. Geotechnical Properties and Behaviour of some Nigerian Lateritic Soils in Ola, S.A. *Tropical Soils of Nigeria in Engineering Practice*. A. A. Balkema: Rotterdam, The Netherlands: 61-84.
- [4] Alhassan M., Mustapha M., 2007. Effects of Rice Husk Ash on Cement Stabilized Laterite. *Leonardo Electronic Journal of Practices and Technologies*, vol. 11: 47-58.
- [5] Okafor F.O., Okonkwo U.N., 2009. Effects of Rice Husk Ash on some Geotechnical Properties of Lateritic Soil. *Nigerian Journal of Technology*, vol. 28, no. 1: 46-52.
- [6] Eberemu A.O., Edeh J.E., Gbolokun A.O., 2013. The Geotechnical Properties of Lateritic Soil Treated with Crushed Glass Cullet. *Advance Materials Research*, vol. 824: 21-28.
- [7] Olufowobi J., Ogundoku A., Michael B., Aderinlewo O., 2014. Clay Soil Stabilisation using Powdered Glass. *Journal of Engineering Science and Technology*, vol. 9, no. 5: 541-558.
- [8] El-Kheshen A. A., 2012. Glass as Radiation Sensor. *Current Topics in Ionizing Radiation Research*, edited by Mitsuru Neno (InTech) 579-602
- [9] Kumar S., Sangwan P., Dhankhar R., Mor V., Bidra S., 2013. Utilization of Rice Husk and their Ash: A Review. *Research Journal of Chemical and Environmental Sciences*, vol. 1, no. 5: 126-129.
- [10] ELC, 2015. Cement. The Environmental Literacy Council website: <http://www.enviroliteracy.org/environment-society/materials-use/cement/> (April 22, 2016)
- [11] Tashima M.M., Silva C.A., Akasaki J.L., Barbosa M.B., 2004. The possibility of adding rice husk ash (RHA) to concrete. In: *Proceedings of the 2004 inter-national RILEM Conference on the Use of Recycled Materials in Building and Structures*. Barcelona, 778-786.
- [12] AASHTO, 1986. Standard specifications for transportation materials and methods of sampling and testing. American Association for State Highway and Transportation Officials. Washington D.C.

FINITE ELEMENT MODELLING AND ANALYSIS OF CONCRETE CONFINED BY STIRRUPS IN SQUARE RC COLUMNS

Xiang Zeng^{1,2}

¹ College of Civil Engineering and Architecture, Hainan University, No.58, Renmin Ave., Haikou 570228, China

² Institute of Development on International Tourist Destination, No.58, Renmin Ave., Haikou 570228, China
E-mail: zeng_t08@163.com

ABSTRACT

Concrete confined by stirrups with greater ductility than unconfined concrete has been used widely in reinforced concrete (RC) structures and its behavior is the classic topic. As the computer power is improving, an increasing number of modelling studies of the confined concrete using finite element (FE) methods have emerged in recent years. Aiming at developing a FE model to evaluate the behavior of concrete confined by stirrups in square RC columns, a new uniaxial compression stress-strain relation of concrete considering the confinement effect of stirrups was proposed. In the FE model, the behavior of confined concrete was described by combining the concrete damaged plasticity model with the proposed uniaxial compression stress-strain relation of confined concrete. Then, tested square RC columns confined by stirrups under axial load were simulated and the details of the FE model were described. Though the comparison between the predicted and measured curves of axial load N versus axial strain ε , the proposed uniaxial compressive model of confined concrete was verified. Finally, a parametric study of the effects of strength of stirrup and equal strength replacement of stirrups on the behavior of confined concrete was conducted.

KEYWORDS

Confined concrete; Confinement effect of stirrups; Uniaxial compression model; Finite element modelling; Parametric study

INTRODUCTION

Confined concrete with high volumetric stirrup ratio has been used widely in RC structures due to its higher strength and ductility caused by the confinement pressure of the stirrups. Many experiments on the behaviors of confined RC column under axial load have been carried out [1-4]. Based on the experimental studies, various empirical or semi-empirical formulas have been developed for describing the uniaxial compression stress-strain relation of stirrup-confined concrete by using the regression analysis or simplified theoretical studies [5-11]. As shown in Figure 1, those formulas describe the same characteristics of confined concrete, namely, higher peak stress and peak strain and much gentler descending branch of the stress versus strain relation than those of unconfined concrete. Most of the formulas are very practical.

With the advancement of the computer power, an increasing number of modeling studies of the confined concrete using FE methods have emerged in recent years [12-17]. Most of such

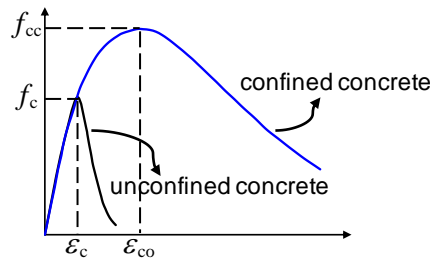


Fig. 1. - Uniaxial stress–strain curve of confined concrete based on experiments

studies have put the emphasis on the development of the constitutive model of confined concrete [12-15] and some of them investigated the effect of certain confinement arrangements on the behaviour of confined concrete [15-17]. As a matter of fact, high fidelity numerical simulation is a powerful means to investigate the mechanism of confining effects of stirrups and influential parameters and it is able to give more details about the mechanical responses of the confined concrete members under different loads. Now, FE modelling using the general-purpose simulation tools, which is much simpler and more accessible than using the complete program code compiled by the investigator self, has been popular in various research fields. So, developing the FE model of confined concrete based on the general-purpose simulation tools is very significant. However, few researchers have paid great attention to the topic [15-16].

Aiming at evaluating the behavior of confined concrete in square RC columns using a FE model based on the general-purpose simulation tool ABAQUS, a new uniaxial compression stress-strain relation of concrete with the confinement of stirrups was proposed in this study. Then, a FE model of RC column with consideration of the confinement effect of stirrups was developed. In the FE model, the behavior of confined concrete was described using the concrete damaged plasticity model into which the proposed uniaxial compression stress-strain relation of confined concrete was introduced. In order to verify the developed FE model, a comparison between the simulation and experimental results of the stirrup-confined RC columns under axial load was carried out. Finally, a parametric study of the effects of strength of stirrup and equal strength replacement of stirrups on the behavior of confined concrete was conducted.

BRIEF DESCRIPTION OF EXPERIMENT

In the paper, three RC columns with volumetric stirrup ratio ρ_v between 0.8% and 2.39% from the experiment conducted by Sheikh and Uzumeri [1] were simulated to verify the following FE model. The length of the test region of the columns, in which the stirrups were placed at specified spacing, was about 533 mm (Figure 2). The scheme of the stirrups in the test region and details of test specimens are presented in Figure 2. To ensure that the failure would occur in the test region, the tapered ends of the column were further confined with the help of welded boxes. In

Tab. 1. - Properties of tested columns

Specimen	Cylinder strength of concrete f_c (Mpa)	Longitudinal steel			Stirrup			
		Number and size	Diameter (mm)	Yielding strength f_y (Mpa)	Diameter (mm)	Spacing (mm)	Yielding strength f_{hy} (Mpa)	Volumetric ratio ρ_s
2A1-1	37.5	8-No. 5	16	372	4.8	57	400	0.8%
4A4-8	40.8	8-No. 7	22	385	4.8	29	400	1.6%
2A5-14	31.5	8-No. 5	16	403	9.5	76	400	2.4%

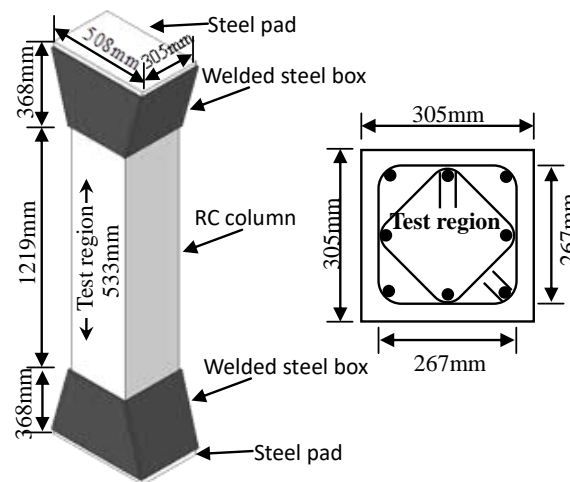


Fig. 2. - Details of test specimens

Table 1, the properties of tested columns were given in detail. All the specimens were applied on a concentric load. More details about the experiment could be seen in the paper by Sheikh and Uzumeri [1].

MATERIAL MODELLING OF CONCRETE

Concrete damaged plasticity model in ABAQUS was used to describe the behaviour of concrete [18]. The model is composed of plasticity model and linearly damaged model. The linearly damaged model can describe the stiffness degradation and stiffness recovery effects associated with stress reversals of concrete under cyclic loading. If no damage parameter is defined, the model is equal to a plasticity model. Under monotonic load, it is unimportant to use the damaged model. So, only the plasticity model is used under monotonic load in this study. The plasticity model is able to consider the strength improving at the state of triaxial loading by the definition of the yielding surface, and the description of the plastic behaviour is related to the equivalent stress-strain relationships of concrete, so taking the empirical or semi-empirical stress-strain relations of confined concrete based on experiments shown in Figure 1 as the equivalent uniaxial compression stress-strain relation in the concrete damaged plasticity model will predict the behaviour of confined concrete incorrectly. It seems that it is difficult to predict reasonably the post-peak behaviour of passively confined concrete in ABAQUS using the stress-strain relation of unconfined concrete [19]. By now, there is no proper uniaxial compression stress-strain relation for simulating the behaviour of stirrup-confined concrete in concrete damaged plasticity model in ABAQUS. Thus, a suitable equivalent uniaxial compressive stress-strain relation of stirrup-confined concrete is important. The author proposed a new equivalent uniaxial compressive stress-strain relation described in the following section. The basic innovation of the proposed compressive stress-strain relation is that it revised the peak strain and descending branch of the stress-strain relation of unconfined concrete by considering the confinement effect of stirrups and it is suitable for simulating the behaviour of stirrup-confined concrete in the concrete damaged plasticity model.

In the material model, the modulus of elasticity of concrete is assumed to be constant for an effective numerical implementation in ABAQUS and is equal to $4730f_c^{0.5}$ determined according to the building code compiled by ACI committee 318 [20], where f_c (N/mm²) means the cylinder strength of concrete. The Poisson's ratio of concrete is deemed to be constant and is equal to 0.2 [21]. The plastic parameters in the material model for the unconfined and confined concrete including dilation angle, eccentricity, ratio of the biaxial compression strength to uniaxial compression strength of concrete, the ratio of the second stress invariant on the tensile meridian to

that on the compressive meridian and viscosity parameter are 30°, 0.1, 1.16, 0.667, 0.0001, respectively.

A new equivalent uniaxial compressive stress-strain relation of stirrup-confined concrete

A new equivalent uniaxial compressive stress-strain relation of confined concrete in prototype column (as shown in Figure 3) is proposed by the author as following:

$$y = \begin{cases} \alpha_a \cdot x + (3 - 2\alpha_a)x^2 + (\alpha_a - 2)x^3 & (x \leq 1) \\ \frac{x}{\alpha_d \cdot (x - 1)^2 + x} & (x > 1) \end{cases} \quad (1)$$

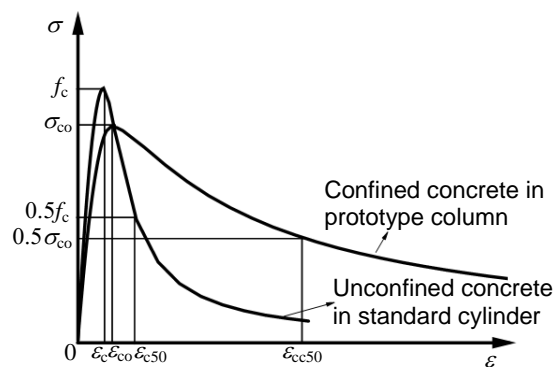


Fig. 3. - Stress-strain relation of confined concrete

In Eq. 1, $x = \epsilon / \epsilon_{c0}$ and $y = \sigma / \sigma_{co}$, σ_{co} is the peak strength of confined concrete and $\sigma_{co} = 0.85f_c$ N/mm² by considering a strength-reduction factor related to the column shape, size and the difference between the strength of in situ concrete and the strength determined from standard cylinder tests [4, 9]. ϵ_{c0} is the peak strain of confined concrete, which is expressed as

$$\epsilon_{c0} = \epsilon_c + 800 \cdot I_e^{0.2} \cdot 10^{-6} \quad (2)$$

$$I_e = \rho_{se} f_h / \sigma_{co} \quad (3)$$

where ϵ_c is the peak strain of unconfined concrete and its value is taken from *Fib Model Code for Concrete Structures 2010* [21]. I_e is the effective confinement index evaluated at ϵ_{c0} . f_h is the stress in confinement reinforcement at peak strength of confined concrete. f_h proposed by Le'geron and Paultre [9] is shown as follows:

$$f_h = \begin{cases} f_h = f_{hy} & \kappa \leq 10 \\ f_h = \min(f_{hy}, \frac{0.25\sigma_{co}}{\rho_{se}(\kappa - 10)}) & \kappa > 10 \end{cases} \quad (4)$$

$$\rho_{se} = k_e A_{sh} / sc \quad (5)$$

$$\kappa = \sigma_{co} / (\rho_{se} E_s \epsilon_c) \quad (6)$$

where f_{hy} is the yield strength of stirrups. ρ_{se} is the effective sectional ratio of confinement reinforcement and κ is a parameter used to determine if yielding of transverse reinforcement occurs at peak strength of confined concrete. In Eq. 5, s and c are the spacing of stirrups and the diameter of the core measured centre-to-centre of hoops, respectively; A_{sh} is the total cross section

of stirrups in the one direction perpendicular to one side of the square column within spacing s . In Eq. 6, E_s is the modulus of elasticity of transverse reinforcement. k_e is the geometrical effectiveness coefficient of confinement, which represents the ratio of the smallest effectively confinement concrete area at midway between two layers of stirrups to the nominal concrete core area. k_e is proposed by Mander et al. [7]:

$$k_e = \frac{(1 - \frac{\sum w_i^2}{6c_x c_y})(1 - \frac{s'}{2c_x})(1 - \frac{s'}{2c_y})}{1 - \rho_c} \quad (7)$$

As shown in Figure 4, w_i in Eq. 7 is the i th clear distance between adjacent longitudinal bars. s' is the clear spacing of transverse reinforcement. ρ_c is the ratio of area of longitudinal steel to area of core section. c_x and c_y are the core dimensions to the centrelines of perimeter stirrups in two directions along the two sides of a RC column, respectively, and they are equal to c for square RC column.

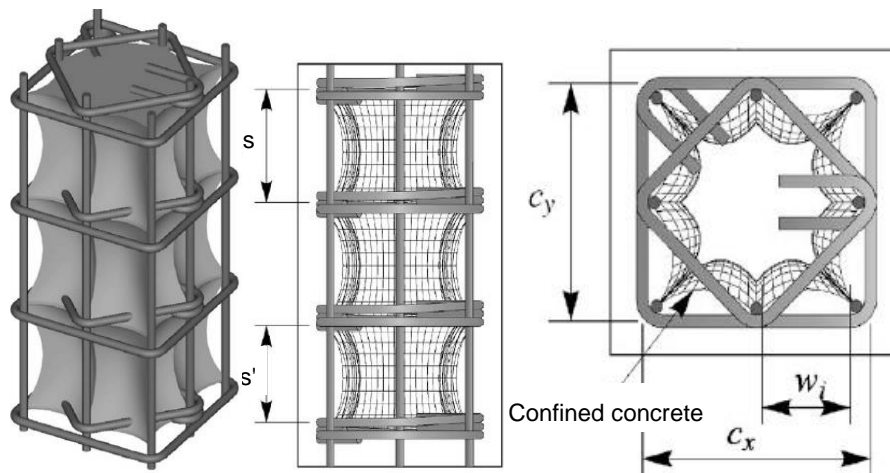


Fig. 4. - Diagram of partial parameters [22]

In Eq. 1, α_a and α_d control the slope of the ascending and descending branches of stress-strain curve. The expressions of α_a and α_d are shown as follows:

$$\alpha_a = 2.4 - 0.0125\sigma_{co} \quad (8)$$

$$\alpha_d = \frac{\varepsilon_{cc50} / \varepsilon_{co}}{(\varepsilon_{cc50} / \varepsilon_{co} - 1)^2} \quad (9)$$

where ε_{cc50} is the post-peak axial strain in confined concrete when capacity drops to 50% of confined strength. Based on the expression of ε_{cc50} proposed by Le'geron and Paultre [9], the modified expression of ε_{cc50} is suggested as:

$$\varepsilon_{cc50} = \varepsilon_{c50} (1 + 80I_{e50}) \quad (10)$$

$$I_{e50} = \rho_{se} f_{hy} / \sigma_{co} \quad (11)$$

in Eq. 10, ε_{c50} is post-peak axial strain of unconfined concrete when capacity drops to 50% of unconfined strength and $\varepsilon_{c50} = 0.004$ according to the proposal by Le'geron and Paultre [9]. I_{e50} is the effective confinement index evaluated at ε_{cc50} .

Uniaxial compression stress-strain relations of cover concrete and concrete confined by steel box

When the two effective confinement indexes I_e and I_{e50} are set to be zero, the Eq. 1 presents the uniaxial compressive stress-strain relation of unconfined concrete, which is used to simulate the behaviour of the cover concrete of RC column.

The uniaxial compression stress-strain relation of concrete confined by steel box presented by Han et al. [23], which considers the confinement effect of the steel tube on the plastic behaviour of concrete, is used to simulate the behaviour of confined concrete at the end of the specimens in Figure 1.

Uniaxial tensile behaviour

The tensile behaviour of concrete is assumed to be linear elastic until the tensile strength [18]. The post failure behaviour is specified by applying a fracture energy cracking criterion. The fracture energy is specified directly as a material property in the model and a linear loss of strength after cracking is assumed. The value of fracture energy G_F in N/m is determined by the expression proposed by the *Fib Model Code for Concrete Structures 2010* [21],

$$G_F = 73f_c^{0.18} \quad (12)$$

where f_c is the compressive strength in MPa.

MATERIAL MODELLING OF STEEL REBAR AND STEEL PAD

Isotropic elastic-plastic model was used to describe the behaviour of the rebar. The stress-strain relation for steel rebar consists of two linear stages (i.e. elastic and hardening) and the hardening modulus was $0.01E_s$, where E_s is the modulus of elasticity of steel rebar. The modulus of elasticity E_s is acquired from the material tests.

The steel pad is considered the elastic material with an elastic modulus of 2.06×10^5 MPa.

FE MODELLING OF CONFINED RC COLUMNS

The FE model was established based on the general-purpose FE software ABAQUS and the module of ABAQUS/Explicit is used to solve the static nonlinear problem.

The steel rebar is modelled using 2-node linear 3-D truss element (T3D2). Both the steel plate and the concrete were modelled as 8-node brick elements (C3D8R). The approximate global mesh size of 50 mm for the concrete body and the approximate global mesh size of 10 mm for the steel cage can provide precise simulation result. The FE model mesh is illustrated in Figure 5.

Embedded region constraint was employed in the FE model to embed the steel reinforcement cage (embedded elements) within the concrete block (host elements). That means the translational degrees of freedom of the embedded node are constrained to the interpolated values of the corresponding degrees of freedom of the host element, but these rotations are not constrained by the embedding [18].

As shown in Figure 5, one-half model with symmetry boundary on the X-Y plane was used to reduce the computation cost. The kinematic coupling constraint is used to constrain the motion of the end surface of the specimen to the motion of a reference point. The axial load was applied to the top reference point with translational degrees of freedom in the direction Y and Z and rotational degrees of freedom like spherical hinge. Pinned support boundary condition was set on the bottom reference point. The boundary conditions in FE model were chosen according to the real experimental boundary conditions.

General contact combining penalty friction formulation for the tangential behaviour and a contact pressure model in the normal direction was used to simulate the interaction between the

contact surfaces of steel boxes and the ends of concrete columns. A tie constrain was used to define the interaction between the steel pad at the end of the column and the corresponding end surface.

VERIFICATION

Figures 6 (a), (b) and (c) show the comparison of the axial load (N) versus the axial strain (ε) relations from the experiment and simulation. Here, the axial strain is an average value of the strain in the test region of specimens. It can be seen that the developed FE model is able to evaluate well the N - ε curves of RC columns with different volumetric ratio ρ_v varying in a range of 0.8%~2.39%.

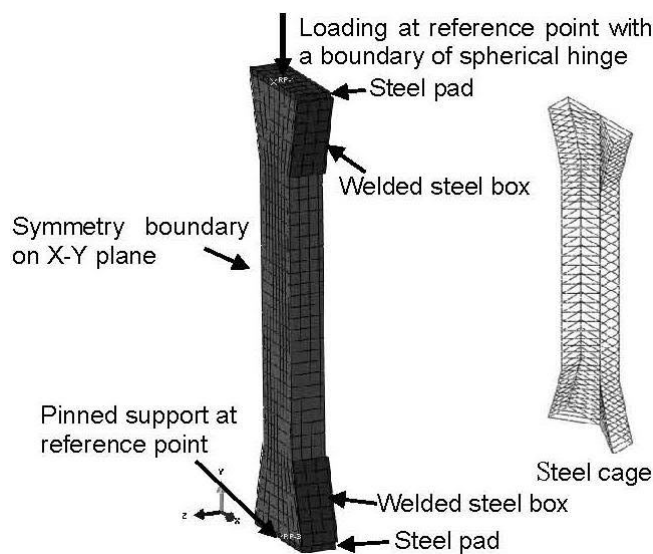


Fig. 5. - Boundary conditions and FEM meshes

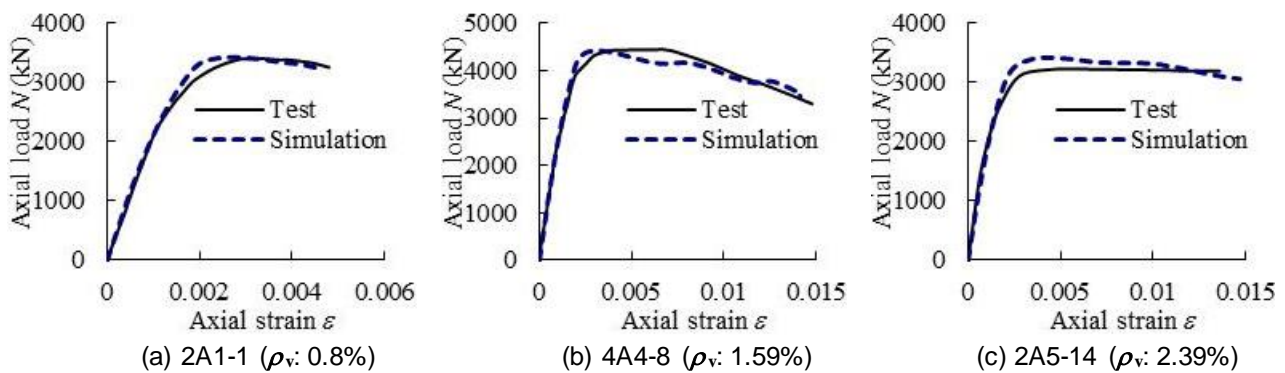


Fig. 6. - Comparison between experimental and predicted N - ε curves

EFFECTS OF STRENGTH AND EQUAL STRENGTH REPLACEMENT OF STIRRUPS

A parametric study was conducted based the verified FE model to investigate the effects of strength and equal strength replacement of stirrups. The details of all the specimens here are the same with the test specimens shown in Figure 2 except the investigated parameters illustrated in Table 2. As shown in Table 2, all specimens have the identical arrangement of longitudinal steel (8-No. 5) with the same yielding strength (400 MPa) and size (16 mm in diameter). The titles of the

specimens indicate the varied parameters. The alphanumeric characters in the titles of the specimens (e.g., C3S6-57R) have the following significance. The first letter C represents concrete and the number after the first letter indicates the cylinder strength of the concrete f_c . Number 3 and 6 represent 30 MPa and 60 MPa in cylinder strength of concrete, respectively. The second letter S refers to the stirrup and the following number represents the yielding strength of stirrup. Number 3 and 6 represent 300 MPa and 600 MPa in yielding strength of stirrup, respectively. The last two numbers are the spacing of stirrups. Numbers 57 and 29 mean 57 mm and 29 mm in spacing of stirrups, respectively. The last letter R shows the equal strength replacement of stirrups, which means that there is no change of spacing of stirrups and the product of the section area and yielding strength of steel bar retains the same when new steel rebar is instead of the old steel rebar. For example, specimen C3S6-57R represents the equal strength replacement of stirrups of specimen C3S6-57.

Tab. 2: Details of parameters

Specimen	Longitudinal steel			Stirrup				f_c (Mpa)
	Number and size	Diameter (mm)	Yielding strength f_y (Mpa)	Diameter (mm)	Spacing (mm)	Yielding strength f_{hy} (Mpa)	Volumetric ratio ρ_s	
C3S3-57	8-No. 5	16	400	4.8	57	300	0.8%	30
C3S6-57	8-No. 5	16	400	4.8	57	600	0.8%	30
C3S6-57R	8-No. 5	16	400	6.8	57	300	1.6%	30
C6S3-57	8-No. 5	16	400	4.8	57	300	0.8%	60
C6S6-57	8-No. 5	16	400	4.8	57	600	0.8%	60
C6S6-57R	8-No. 5	16	400	6.8	57	300	1.6%	60
C3S3-29	8-No. 5	16	400	4.8	29	300	1.6%	30
C3S6-29	8-No. 5	16	400	4.8	29	600	1.6%	30
C3S6-29R	8-No. 5	16	400	6.8	29	300	3.2%	30
C6S3-29	8-No. 5	16	400	4.8	29	300	1.6%	60
C6S6-29	8-No. 5	16	400	4.8	29	600	1.6%	60
C6S6-29R	8-No. 5	16	400	6.8	29	300	3.2%	60

Figure 7 (a) and (b) show that the increase in strength of stirrups has little influence on the strength of core concrete, but it increases the ductility of the specimens indicated by the much gentler descending curves of $N-\varepsilon$. There exists a reasonable explanation for the phenomenon. The behaviour of confined concrete is related to the confinement stress from stirrups that is determined by the extent of lateral dilation of core concrete under axial load. It is found in the FE analysis that the stress of stirrups in specimens with varied strength of stirrups is close to each other at the peak axial loads, which leads to slight difference in strength of core concrete between the two contrasting specimens. That is because little lateral dilation of core concrete happens in the stage and limited stress of stirrups is produced leading to weakly exerting the high strength of stirrup. However, the extent of lateral dilation of core concrete increases with the axial deformation of column increasing in the descending stage of loading. Thus, higher stress in stirrups is produced for high strength stirrup, which causes higher confinement stress and the ductility of columns is improved. The high strength of stirrups is exerted considerably in this stage.

As shown in Table 2, the equal strength replacement of stirrup using the low strength steel in replacement of high strength steel (e.g., C3S6-57 and C3S6-57R) increases the volumetric ratio due to the size of the stirrups increasing. That improves the confinement effect of stirrups on core

concrete at peak axial load and gives rise to higher peak axial load, which can be observed in Figure 8. It appears that the smaller spacing of stirrups produces higher increase in peak axial load after the equal strength replacement of stirrup. Figure 8 (a) and (b) depict the reduction of ductility after the equal strength replacement of stirrup indicated by the steeper descending curves of $N-\varepsilon$.

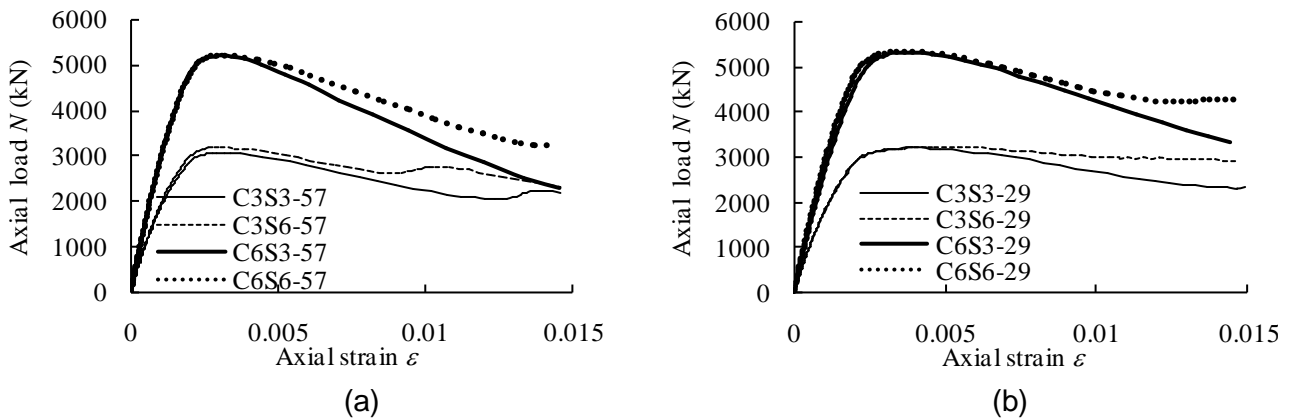


Fig. 7. - Effect of strength of stirrup

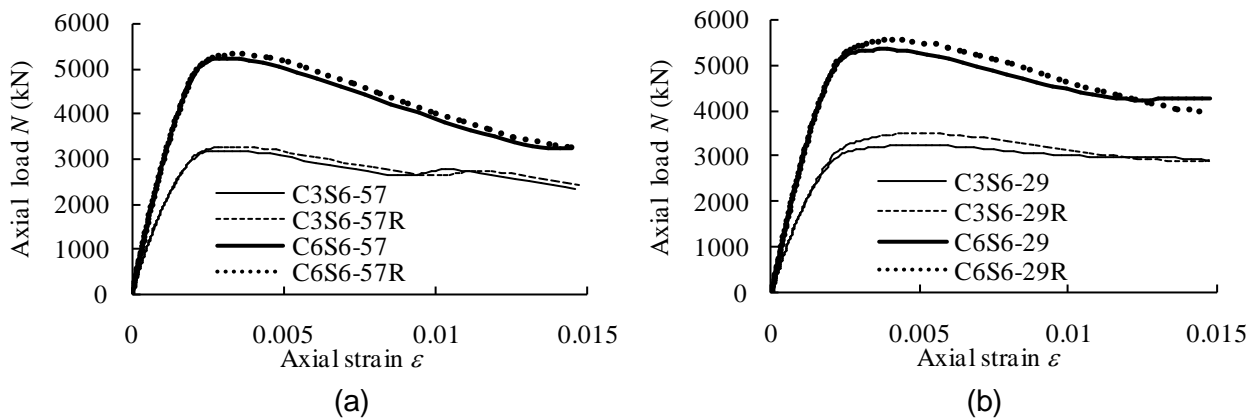


Fig. 8. - Effect of equal strength replacement of stirrup

CONCLUSION

In this paper, a new uniaxial compressive stress-strain relation of concrete confined by stirrups in square RC column was proposed to describe the behaviour of the confined concrete in three-dimension FE model by combining the concrete damaged plastic material model in ABAQUS. Based on the material model, a FE model for square confined RC columns under axial compression was developed. The FE model evaluates the $N-\varepsilon$ curves of tested confined RC columns well. Thus, the proposed uniaxial compressive stress-strain relation in conjunction with the concrete damaged plasticity model has the capability to evaluate the behaviour of concrete confined by stirrups and can be used to further investigate the behaviour of square confined RC members under different types of load.

A further parametric study shows that increasing the strength of stirrups has little effect on the strength of confined concrete, but it improves the ductility of the confined concrete. The equal strength replacement of stirrups using the low strength steel in replacement of high strength steel increases the strength of core concrete, but reduces the ductility of confined concrete.

ACKNOWLEDGEMENTS

The research reported in the paper is supported by the National Natural Science Foundation of China (No. 51608156), the Project of the Natural Science Foundation of Hainan Province (No. 20165208), the Scientific Research Starting Foundation of Hainan University (No. kyqd1534). All these sources of financial support are highly appreciated.

REFERENCES

- [1] Sheikh S.A., Uzumeri S.M., 1980. Strength and ductility of tied concrete columns. *Journal of the Structural Division*, 106(ST5): 1079-1102.
- [2] Scott B.D., Park R., Priestley M.J.N., 1982. Stress-strain behavior of concrete confined by overlapping hoops at low and high strain rates. *ACI Journal Proceedings*, 79(1): 13-27.
- [3] Moehle J.P., Cavanagh T., 1985. Confinement effectiveness of cross-ties in RC. *Journal of Structural Engineering*, 111(10): 2105-2120. [http://dx.doi.org/10.1061/\(ASCE\)0733-9445\(1985\)111:10\(2105\)](http://dx.doi.org/10.1061/(ASCE)0733-9445(1985)111:10(2105)).
- [4] Chung H.S., Yang K.H., Lee Y.H., Eun H.C., 2002. Strength and ductility of laterally confined concrete columns. *Canadian Journal of Civil Engineering*, 29(6): 820-830. <http://dx.doi.org/10.1139/I02-084>.
- [5] Park R., Priestley M.J.N., Gill W.D., 1982. Ductility of square confined concrete columns. *Journal of Structural Engineering*, 108(4): 929-950.
- [6] Sheikh S.A., Uzumeri S.M., 1982. Analytical model for concrete confinement in tied columns. *Journal of the Structural Division*, 108(12): 2703-2722.
- [7] Mander J.B., Priestley M.J.N., Park R., 1988. Theoretical stress-strain model for confined concrete. *Journal of Structural Engineering*, 114(8): 1804-1826. [http://dx.doi.org/10.1061/\(ASCE\)0733-9445\(1988\)114:8\(1804\)](http://dx.doi.org/10.1061/(ASCE)0733-9445(1988)114:8(1804)).
- [8] Saatcioglu M., Razvi S.R., 1992. Strength and ductility of confined concrete. *Journal of Structural Engineering*, 118(6): 1590-1607. [http://dx.doi.org/10.1061/\(ASCE\)0733-9445\(1992\)118:6\(1590\)](http://dx.doi.org/10.1061/(ASCE)0733-9445(1992)118:6(1590)).
- [9] Le'geron F., Paultre P., 2003. Uniaxial confinement model for normal- and high-strength concrete columns. *Journal of Structural Engineering*, 129(2): 241-252. [http://dx.doi.org/10.1061/\(ASCE\)0733-9445\(2003\)129:2\(241\)](http://dx.doi.org/10.1061/(ASCE)0733-9445(2003)129:2(241)).
- [10] Bousalem B., Chikh N., 2007. Development of a confined model for rectangular ordinary reinforced concrete columns. *Materials and Structures*, 40(6): 605-613. <http://dx.doi.org/10.1617/s11527-006-9172-2>.
- [11] Samani A.K., Attard M.M., 2012. A stress-strain model for uniaxial and confined concrete under compression. *Engineering Structures*, 41: 335-349. <http://dx.doi.org/10.1016/j.engstruct.2012.03.027>.
- [12] Liu J., Foster S.J., 2000. A three-dimensional finite element model for confined concrete structures. *Computers & Structures*, 77(5): 441-451. [http://dx.doi.org/10.1016/S0045-7949\(00\)00007-9](http://dx.doi.org/10.1016/S0045-7949(00)00007-9).
- [13] Kwon M., Spacone E., 2002. Three-dimensional finite element analyses of reinforced concrete

columns. *Computers & Structures*, 80(2): 199-212. [http://dx.doi.org/10.1016/S0045-7949\(01\)00155-9](http://dx.doi.org/10.1016/S0045-7949(01)00155-9).

[14] Yu T., Teng J.G., Wong Y.L., Dong S.L., 2010. Finite element modeling of confined concrete-I: drucker-prager type plasticity model. *Engineering Structures*, 32(3): 665-79. <http://dx.doi.org/10.1016/j.engstruct.2009.11.014>.

[15] Zeng X., Xu B., 2014. Numerical simulation on the dynamic behavior of short RC columns subjected to concentric rapid loading considering confinement effect of stirrups. *Engineering Mechanics*, 31, 190-197.

[16] Song Z.H., Lu Y., 2011. Numerical simulation of concrete confined by transverse reinforcement. *Computers and Concrete*, 8(1): 23-41. <http://dx.doi.org/10.12989/cac.2011.8.1.023>.

[17] Faria R., Pouca N.V., Delgado R., 2004. Simulation of the cyclic behaviour of R/C rectangular hollow section bridge piers via a detailed numerical model. *Journal of Earthquake Engineering*, 8(5): 725-748. <http://dx.doi.org/10.1080/13632460409350507>.

[18] Dassault Systemes Simulia Corp., 2014. Abaqus Version 6.14 Documentation- ABAQUS Theory Guide (Dassault Systemes Simulia Corporation).

[19] Tao Z., Wang Z.B., Yu Q., 2013. Finite element modelling of concrete-filled steel stub columns under axial compression. *Journal of Constructional Steel Research*, 89: 121-131. <http://dx.doi.org/10.1016/j.jcsr.2013.07.001>.

[20] ACI Committee 318, 2008. Building code requirements for structural concrete (ACI 318-08) and commentary (American Concrete Institute) 109 pp.

[21] Fib, 2013. Fib Model Code for Concrete Structures 2010 (Ernst & Sohn).

[22] Paultre P., Légeron F., 2008. Confinement reinforcement design for reinforced concrete columns. *Journal of Structural Engineering*, 134(5): 738-749. [http://dx.doi.org/10.1061/\(ASCE\)0733-9445\(2008\)134:5\(738\)](http://dx.doi.org/10.1061/(ASCE)0733-9445(2008)134:5(738)).

[23] Han L.H., Yao G.H., Tao Z., 2007. Performance of concrete-filled thin-walled steel tubes under pure torsion. *Thin Walled Structures*, 45(1): 24-36. <http://dx.doi.org/10.1016/j.tws.2007.01.008>.

RESEARCH ON DYNAMIC SIMILARITY MODEL TEST OF DAMAGE DETECTION FOR TRANSMISSION TOWER

Zhou Ling¹, Li Ying-tao¹, Yang Chao-shan¹, Deng Zhi-ping¹, Chen Jin¹

¹ *Department of Civil Engineering, Logistical Engineering University, Chongqing, 401311, P.R.China*

ABSTRACT

In order to explore the dynamic similarity model test method different from atmospheric boundary layer wind tunnel and shaking table model test, in accordance with dynamic similar theory, an elastic model of a transmission tower with 1/35 scale and 5.2m height has been designed and manufactured with thin-walled circular pipes of high-density polyethylene. The model has been tested in the laboratory for time and frequency domain responses under suddenly unloading, essential dynamic characteristic of the scale model is also analysed and compared with that of its prototype tower, the dynamic similarity of the two is confirmed. By the mathematical deduction of Wigner-Ville Distribution (WVD) signal terms of structural free vibration response, the new damage detection index with clear physical signification is forwarded for damage detection for transmission tower, the damage detection test of the scale model of transmission tower is then carried out, totally three damage cases, related with chord rod weakening, flank rods failure, different damage degrees and positions, are tested to validate the proposed damage detection index.

KEYWORDS

Dynamic similarity, Model test, Damage detection, Transmission tower

1. INTRODUCTION

Transmission tower is the main structure of the power transmission project, the safety of which is the basis of the large scale regional power system reliability, but the engineering failures of transmission tower at home and abroad occasionally have happened in recent decades. Existing research [1-4] indicates that the vibration of transmission tower with so much members is more complex than general civil engineering, and dynamic characteristics are influenced much by environment condition, incitation factor, tower-line coupling and stiffness changing point, which lead many present proposed damage detection methods and indexes difficult to be applied [5-8]. As the two-dimensional function of time and frequency, the Wigner-Ville Distribution (WVD) has almost all the expected mathematical properties of damage detection, which has been successfully applied in the field of mechanical fault detection [9-10], it is also a very effective method for the damage detection of transmission tower.

Up to now, the researches of transmission tower are mainly focused on the structural dynamic response under wind load and earthquake. The few atmospheric boundary layer wind tunnel and shaking table model test of transmission tower are the application research, which regard the practical project as the research background, mainly measure the structural dynamic characteristics and response, in order to test the rationality of dynamic calculation model and its analysis method,



and ensure the safety and construction of the specific project [11-12]. Meanwhile, the researches on damage detection for transmission tower are still at preliminary stage, even the research on model test of damage detection for transmission tower has not been reported yet.

Therefore, to explore the dynamic similarity model test method different from atmospheric boundary layer wind tunnel and shaking table model test, in accordance with dynamic similar theory, an elastic model of a transmission tower with 1/35 scale and 5.2m height has been designed and manufactured with thin-walled circular pipes of high-density polyethylene. The model has been tested in the laboratory for time and frequency domain responses under suddenly unloading, essential dynamic characteristic of the scale model is also analysed and compared with that of its prototype tower, the dynamic similarity of the two is confirmed. The damage detection test of the scale model of transmission tower is then carried out, totally three damage cases, related with chord rod weakening, flank rods failure, different damage degrees and positions, are tested to validate the proposed damage detection index.

2. DYNAMIC SIMILARITY CRITERION

The similarity of physical process or phenomenon is expressed by the similarity of various physical characteristics in physical process or phenomenon. There is a certain relationship between the various physical characteristics in the similar physical phenomena, which is the similarity condition of the two similar physical phenomena, is also the principle of the model test. Four similar conditions should be satisfying for general mechanic's phenomena: the similarity of material, the similarity of geometry, the similarity of kinematic and the similarity of dynamic.

The model test takes the transmission tower as the structure prototype, the dynamic characteristics and the free vibration response of the structural system is mainly simulated, and the free vibration equation of the whole quantity form can be expressed in a general manner:

$$\mathbf{M}\mathbf{a} + \mathbf{C}\mathbf{v} + \mathbf{K}\mathbf{y} = 0 \quad (1)$$

where, \mathbf{M} , \mathbf{C} and \mathbf{K} is respectively mass, damping and stiffness matrix, \mathbf{a} , \mathbf{v} and \mathbf{y} is respectively acceleration, velocity and displacement vector.

Due to the structural damping theory is still not perfect, the damping mechanism is not fully reflected by the viscous damping and hysteretic damping theory, the structural damping parameter is difficult to be controlled in the design and manufacture of the model. Thus, the free vibration equation of the prototype of the n -degree structural system without quantitative damping is simplified as:

$$\mathbf{M}_p \mathbf{a}_p + \mathbf{K}_p \mathbf{y}_p = 0 \quad (2)$$

To the model:

$$\mathbf{M}_m \mathbf{a}_m + \mathbf{K}_m \mathbf{y}_m = 0 \quad (3)$$

Set:

$$C_M = \frac{M_{im}}{M_{ip}}, C_K = \frac{K_{im}}{K_{ip}}, C_a = \frac{a_{im}}{a_{ip}}, C_L = \frac{y_{im}}{y_{ip}}, i = 1, \dots, n \quad (4)$$

where, subscript i is i th degree, subscript p and m is respectively prototype and model, C_M , C_K , C_a and C_L is respectively similar coefficient of mass, stiffness, acceleration and geometry.

By equation (4) and decoupling, the equation (2) is deformed as:

$$\frac{C_K C_L}{C_M C_a} \mathbf{M}_m \mathbf{a}_m + \mathbf{K}_m \mathbf{y}_m = 0 \quad (5)$$

Only:
$$\frac{C_K C_L}{C_M C_a} = 1 \quad (6)$$

The phenomena of model and prototype are the same physical phenomena, in which the basic equations describing the relationship between physics in model and prototype and are the same.

The essence of similarity index is to maintain the similarity between the elastic restoring force and the inertia force, according to the dimensional analysis method, the equation (6) is deformed as:

$$\frac{C_E C_t^2}{C_\rho C_L^2} = 1 \quad (7)$$

where, C_E , C_ρ and C_t is respectively similar coefficient of elastic modulus, density and time. The similarity conditions of the model are mainly derived from the similarity of geometry, elastic modulus and density, the similarity coefficient of time determines the similarity of velocity, acceleration, frequency and other physical variables. Thus, the selection of geometry and material of model is particularly important and key.

3. DAMAGE DETECTION INDEX

Under initial displacement condition, the acceleration response of free vibration at position k of non-damping structural system with n degrees of freedom is:

$$a_k(t) = \sum_{i=1}^n \varphi_{ki} \cdot \varphi_i^T \mathbf{M} \mathbf{y}_0 \cdot \cos(\omega_i t + \theta_i) \quad (8)$$

Where, φ_i is i th mode shape, \mathbf{M} is mass matrix, \mathbf{y}_0 is initial displacement condition, ω_i is i th natural frequency, and θ_i is i th initial phase of acceleration response.

After $a_k(t)$ is transformed to analytic signal $z_k(t)$ by Hilbert transform, the Wigner-Ville Distribution (WVD) signal terms of $a_k(t)$ can be deduced as:

$$W_k^{signal}(t, f) = \sum_{i=1}^n (\varphi_{ki} \varphi_i^T \mathbf{M} \mathbf{y}_0)^2 \cdot \delta(f - \frac{\omega_i}{2\pi}) = \sum_{i=1}^n A_k(t) \cdot \delta(f - \frac{\omega_i}{2\pi}) \quad (9)$$

Can be seen from analytic expression, the signal terms in WVD of free vibration response are as follows: n impulse functions located at frequency $f_i = \omega_i / 2\pi$ in time-frequency plane.

If frequency parameter f_i of a signal term is determined, while the i th natural frequency ω_i is easy to be acquired by frequency spectrum or time-frequency analysis, then the time-decaying amplitude $A_k(t) = (\varphi_{ki} \varphi_i^T \mathbf{M} \mathbf{y}_0)^2$ can be determined, the response function of i th mode shape at test point k also can be acquired, by analogy with $k = 1, 2, \dots, n$, the response function of i th mode shape at one time point ($t = t_0$) can be obtained at any test point, finally the i th mode shape can be acquired:

$$\varphi_i = [\sqrt{A_1(t)}, \dots, \sqrt{A_k(t)}, \dots, \sqrt{A_n(t)}]^T = (|\varphi_{1i}|, \dots, |\varphi_{ki}|, \dots, |\varphi_{ni}|)^T \cdot |\varphi_i^T \mathbf{M} \mathbf{y}_0| \quad (10)$$

The positive and negative relations between mode shape components can be determined by the phase relationship of cross-power spectrum at test points, with same direction as positive and different direction as negative.

The structural damage generally will bring changes in physical parameters (such as mass, stiffness and so on), and then results in that structural vibration mode also will change, so the damage message is inevitably contained in the change of mode shape. Meanwhile, the response function relation between WVD signal terms amplitude of free vibration response and mode shape has been revealed. To determine the specific position of structural damage, the key features of damage information can be extracted by WVD signal terms amplitude. Therefore, based on the principle that

quadratic index is more sensitive to small change in mode shape and can find the mutation of damage position, the index WAC is proposed for damage detection for transmission tower:

$$WAC(i) = \frac{|C^d(i) - C^u(i)|}{\sum_{i=1}^n |C^d(i) - C^u(i)|} \quad (11)$$

where, $C^u(i)$ and $C^d(i)$ is respectively amplitude curvature of signal terms in WVD at test point i before and after damage, which can be calculated by central difference method:

$$C(i) = \frac{\sqrt{W_{i-1}^{signal}(t, f)} + \sqrt{W_{i+1}^{signal}(t, f)} - 2\sqrt{W_i^{signal}(t, f)}}{2l_i^2} \quad (12)$$

where, l_i is the space between test points.

4. MODEL DESIGN, MANUFACTURE AND TEST

At present, there are two kinds of transmission tower model design and manufacture methods, which are concentrated stiffness method and discrete stiffness method. The concentrated stiffness method is that the stiffness distribution of prototype is simulated by stiffness distribution along height of the mandrel made with appropriate elastomer, although the design and manufacture of model is simplified, this method has some obvious deficiencies, such as structure stress transmitting path distortion and so on. The discrete stiffness method requires all the members of model to be stiffness similar, the main difficulty of this method is the material and manufacture, because thin-wall steel tubes and angles of transmission tower prototype are scaled down, according to the geometric similar coefficient, the wall of members is very small, which cannot be finished in the actual manufacture.

However, according to the mechanic characteristics of transmission tower, the tower structure can be regarded as the spatial truss structure composed of two force bars by ignoring local bending of the bar, so the simulation of stiffness is only required to meet the similarity of tensile stiffness. The model regards a transmission tower with 181.8m height as structural prototype, the members of model are manufactured with thin-wall circular pipes of high-density polyethylene, a small amount of thin-wall steel angles are replaced according to the principle of equal section area, the density and elastic modulus are respectively 0.958g/cm^3 and 0.7GPa . The model similar coefficients are shown in Table 1, Figure 1 is the photo of transmission tower model in laboratory, and Figure 2 is the position of acceleration sensors and simulated damages.

Tab.1 Model similar coefficients

Similar coefficient	Symbol	Value
Dimension	C_L	1/35
Mass	C_m	1/351324
Tensile stiffness	C_{EA}	1/351750
Frequency	C_f	$\sqrt{35}$
Displacement	C_y	1/35
Velocity	C_v	$1/\sqrt{35}$
Acceleration	C_a	1



Fig. 1. - Model of transmission tower

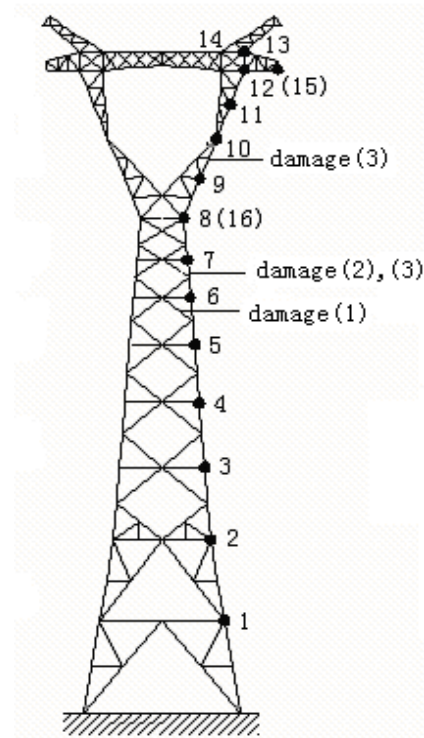


Fig. 2. - Position of sensors and damages

Totally sixteen micro acceleration sensors are used, the test point No.1 to No.14 sensors testing x direction (line direction) acceleration are in turn attached on the surface of chords from tower foot to tower head, the No.15 and No.16 sensors testing y direction (traverse direction) acceleration are respectively attached on the side of chord of tower body and tower head. Considering the test sequence feasibility of different simulated damage states, two types of structural damages of chord rod weakening and flank rod failure are simulated by directly creating damage on the model pipes, as shown in Figure 3. Totally three simulated damage states related with damage type, damage degree and damage position are set up: (1) Single flank rod failure, located at 6th segment of tower body, (2) Single chord rod cross-section weakening 30%, located at 7th segment of tower body, (3) Two chord rod cross-section weakening 30% and 50%, located at 7th segment of tower body and tower head.



(a)



(b)



(c)

Fig. 3. - Damage simulation: (a) flank rod failure (b) chord rod cross-section weakening of tower body (c) chord rod cross-section weakening of tower head

The suddenly unloading incitation is exerted by cutting the tensile wire (diameter 0.2mm) along the horizontal direction, incentive point is located at the bottom of tower head and middle of crossarm, which is respectively load case (1) and (2), the incentive amplitude is the weight (500g) hanged to the wire through the pulley.

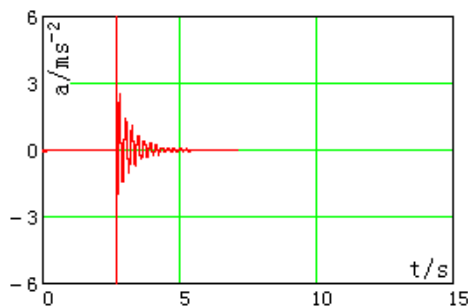
5. RESULTS AND DISCUSSIONS

Figure 4 and Figure 5 are respectively the model typical acceleration response of x and y direction under suddenly unloading incitation, it is shown that the vibration response of the model fade very fast because of the damping effect, the acceleration responses of the model are mainly the low frequency components. Figure 6 and Figure 7 are the model typical acceleration spectrum of x and y direction under suddenly unloading incitation, it is shown that the first order modal response is absolutely dominant in the dynamic response for high rise structures such as transmission tower, and the structural dynamic analysis of the first three order modal components is sufficiently accurate.

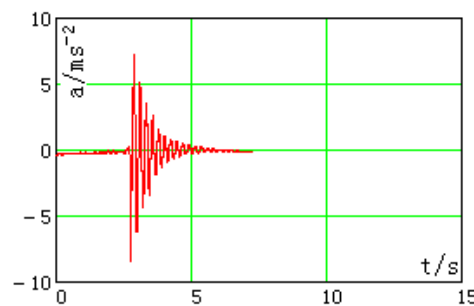
Table 2 is the natural frequency of transmission tower model; the model expectation value comes from prototype theory valve according to the frequency similar coefficient. It can be seen that the model test valve is well identical with the expectation valve, indicating that the design and manufacture of transmission tower model based on dynamic similarity criterion is successful.

Tab.2. - Natural frequency of transmission tower model

No.	Prototype theory valve		Model expectation valve		Model test valve	
	x direction	y direction	x direction	y direction	x direction	y direction
1	0.7526	0.7134	4.4524	4.2205	4.3950	4.1660
2	2.0071	1.6724	11.8742	9.8941	11.719	9.7660
3	3.2628	3.0118	19.3030	17.8180	19.0430	17.5780

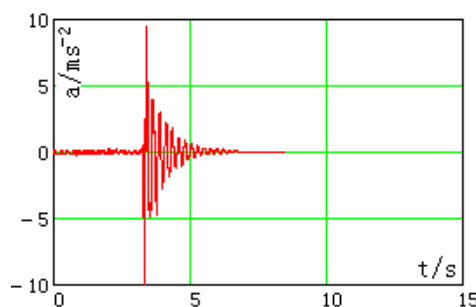


(a) Test No.6

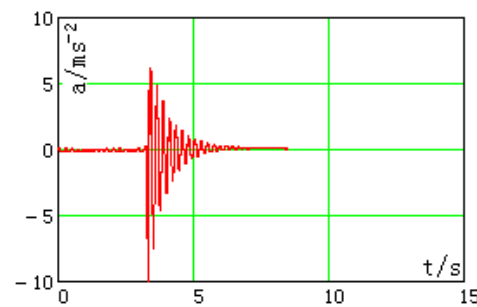


(b) Test No.8

Fig.4. - Acceleration response of x direction



(a) Test No.15



(b) Test No.16

Fig.5. - Acceleration response of y direction



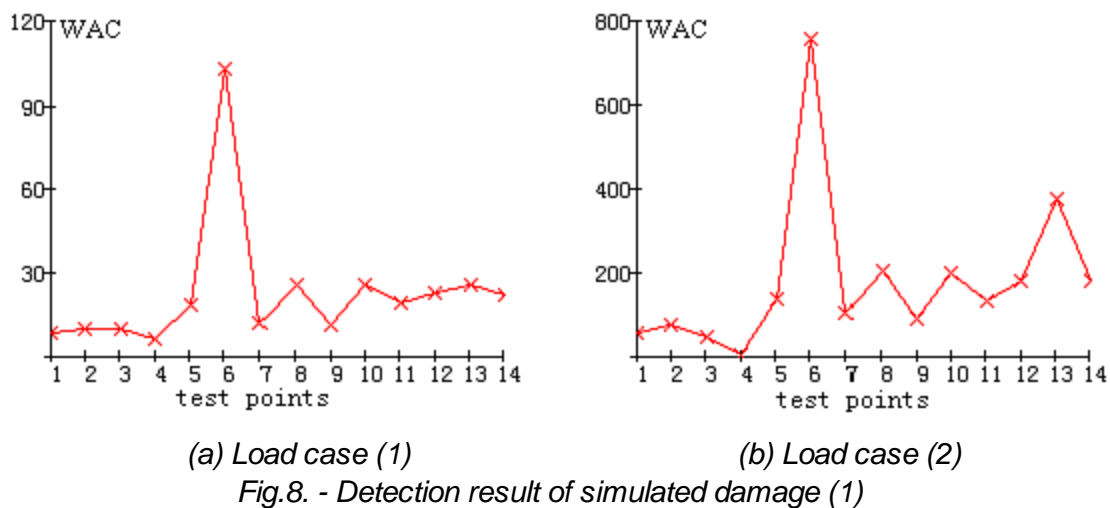
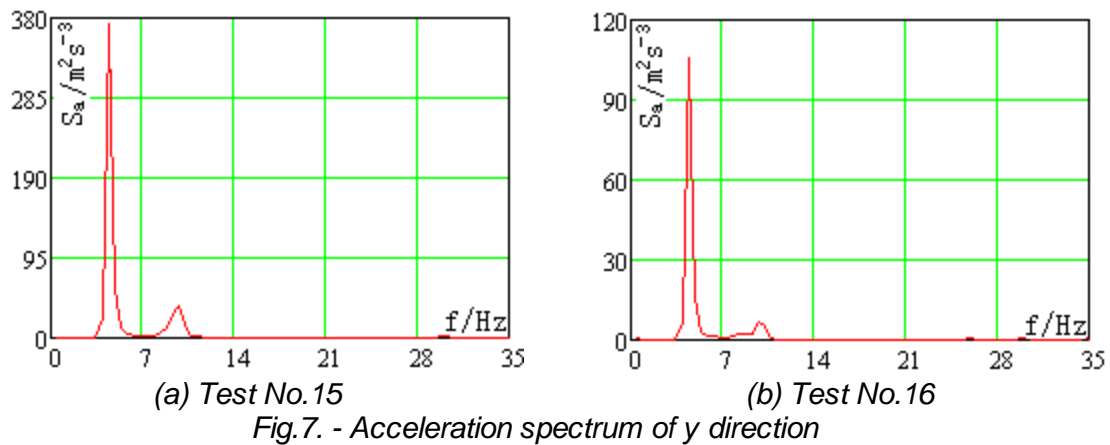
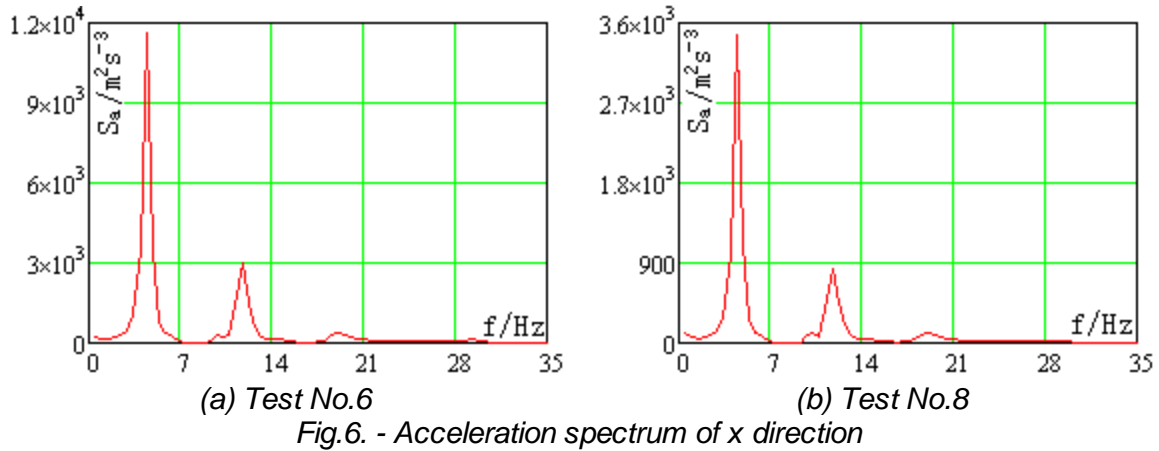


Figure 8 is the detection result of index WAC for simulated damage (1), it is seen that the value of WAC is as a single peak at test point No.6 under two load cases, accurately showing the position of local damage from flank rod failure. The WAC small peak values at junction of tower body and head (test point No.8), middle of tower head (test point No.10) as well as crossarm (test point No.13) are caused by structural itself stiffness mutation.

Figure 9 is the detection result of index WAC for simulated damage (2), it is seen that the value



of WAC is as an independent single peak at test point No.7 under two load cases, clearly displaying the position of local damage from chord rod cross-section weakening of tower body.

Figure 10 is the detection result of index WAC for simulated damage (3), it is seen that the value of index WAC at test point No.7 and test point No.10 under two load cases are as two single peaks, indicating the damage position of tower body and tower head. But the index fails to quantify the relative relationship of two damage degrees at different position.

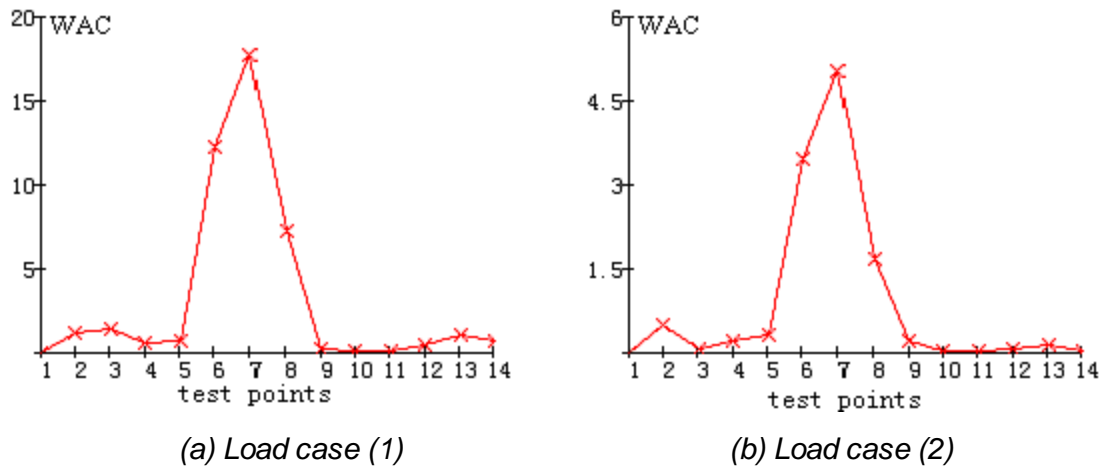


Fig.9. - Detection result of simulated damage (2)

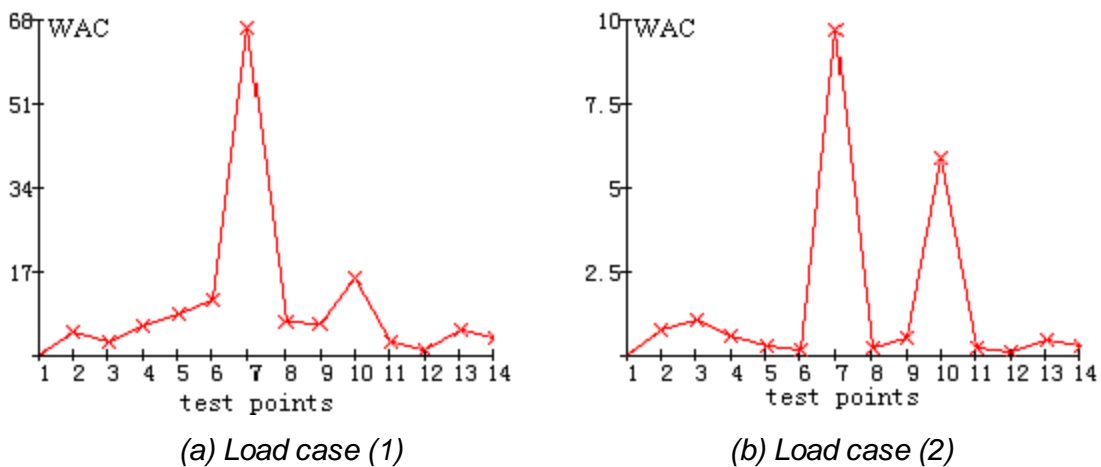


Fig.10. - Detection result of simulated damage (3)

6. CONCLUSIONS

To explore the dynamic similarity model test method different from atmospheric boundary layer wind tunnel and shaking table model test, in accordance with dynamic similar theory, an elastic model of a transmission tower with 1/35 scale and 5.2m height has been designed and manufactured with thin-walled circular pipes of high-density polyethylene.

The model has been tested in the laboratory for time and frequency domain responses under suddenly unloading, essential dynamic characteristic of the scale model is also analyzed and compared with that of its prototype tower, the dynamic similarity of the two is confirmed.

By the mathematical deduction of Wigner-Ville Distribution (WVD) signal terms of structural free



vibration response, the new damage detection index with clear physical signification is forwarded for damage detection for transmission tower, the damage detection test of the scale model of transmission tower is then carried out, totally three damage cases, related with chord rod weakening, flank rods failure, different damage degrees and positions, are tested to validate the proposed damage detection index.

ACKNOWLEDGEMENTS

This work was financially supported by the Chongqing Foundation and Advanced Research Program (cstc2013jcyjA30013).

REFERENCES

- [1] Deng Hong-zhou, Zhu Song-ye, Wang Zhao-min, 2004. Study on dynamic behavior and wind-induced vibration response of long span transmission tower. *Building Structure*, Vol.34(7):25-28
- [2] Dong Dai, Hou Jiang-guo, Xiao Long, 2013. Development of calculation program for identifying main failure modes of transmission tower system. *Engineering Mechanics*. Vol.30(8):180-185
- [3] Xiong Tie-hua, Liang Shu-guo, Zou Liang-hao, 2009. Dominant failure modes of a transmission tower and its ultimate capacity under wind load. *Engineering Mechanics*. Vol. 26(12):100-104
- [4] Liu Chun-cheng, Sun Xian-he, Mou Xue-feng, 2011. Reliability analysis of high voltage transmission tower under icing load. *Water Resources and Power*. Vol. 29(5):156-158
- [5] Li Hong-nan, Bai Hai-feng, 2007. State-of-the-art review on studies of disaster resistance of high-voltage transmission tower-line systems. *Civil Engineering*. Vol. 40(2):39-46
- [6] Lam Heung-fai, Yin Tao, 2011. Dynamic reduction-based structural damage detection of transmission towers: practical issues and experiment verification. *Engineering Structures*. Vol. 33(5):1459-1478
- [7] Liu Gang, Yang Pu, Qin Yang, 2012. Detecting damage location of cup-towers. *Journal of Vibration, Measurement & Diagnosis*. Vol.32(3): 471-476
- [8] Benedikt Weber, Patrick Paultre, 2010. Damage identification in a truss tower by regularized model updating. *Journal of Structural Engineering*. Vol.136(3):307-316
- [9] Climente-Alarcon.V, Antoino-DAviu.J.A, Riera-Guasp.M, 2012. Application of the Wigner-Ville distribution for the detection of rotor asymmetries and eccentricity through high-order harmonics. *Electric power systems research*. 91:28-36
- [10] Ma Hui, Zhao Xin, Zhao Qun-chao, 2007. Application of time-frequency analysis to rotation machinery fault diagnosis. *Journal of Vibration and Shock*, Vol.26(3):61-63
- [11] He Min-juan, Liang Feng, Ma Ren-lei, 2010. Shaking table test for a super high steel TV tower. *Journal of Vibration and Shock*. Vol.33(1):77-80
- [12] Zhao Gui-feng, Xie Qiang, Liang Shu-guo, 2009. Wind tunnel test on wind resistant design of high-voltage transmission tower-line coupling system. *High Voltage Engineering*. Vol.35(5):1206-1213

EXPERIMENTAL RESEARCH INTO DYNAMIC PROPERTIES OF MASONRY BARREL VAULTS NON-REINFORCED AND REINFORCED WITH CARBON COMPOSITE STRIPS

Zigler Radek¹, Witzany Jiří¹, Makovička Daniel², Urushadze Shota³, Pospíšil Stanislav³, Kubát Jan¹, and Kroftová Klára⁴

1. CTU in Prague, Faculty of Civil Engineering, Department of Building Structures, Prague, Thákurova 7, Czech Republic; zigler@fsv.cvut.cz, witzany@fsv.cvut.cz, jan.kubat.2@fsv.cvut.cz
2. CTU in Prague, Klokner Institute, Prague, Šolínova 7, Czech Republic; daniel.makovicka@klok.cvut.cz
3. The Institute of Theoretical and Applied Mechanics AS CR, v. v. i, Prague, Prosecká 809/76, Czech Republic; urushadze@itam.cas.cz, pospisil@itam.cas.cz
4. CTU in Prague, Faculty of Civil Engineering, Department of Architecture, Prague, Thákurova 7, Czech Republic; klara.kroftova@fsv.cvut.cz

ABSTRACT

The study of dynamic behaviour of vaults of historic buildings reveals new knowledge which can be used for the local analysis and stabilisation and rehabilitation designs of damaged vaulted structures. The analysis of the results of dynamic loading brings objective background material for the identification and localisation of failures according to MAC or COMAC criteria [1, 2] and the assessment of serviceability and structural reliability of vaulted structures of historic buildings.

KEYWORDS

Rehabilitation, Strengthening, Masonry vaults, FRP fabrics, Dynamic load, Static load

INTRODUCTION

Barrel vaults belong to the basic vaulted structures. They have been used (to a greater or lesser extent) in all architectural styles starting from Romanesque architecture and they are found in nearly every historic and heritage building. Their shape, derived from the basic cylindrical shape, is the point of departure for a whole group of vaulted structures starting from the cross vault. Barrel vaults were used for roofing buildings with square, rectangular as well as irregular plans, for roofing staircases (straight, sloping, spiral, rising) and other premises for both representative and everyday use.

At the onset of Romanesque architecture in the Czech lands, barrel vaults formed a ceiling swollen to a semi-cylindrical shape which fully sits on, “merges” with vertical masonry. In its secondary, rudimentary, purely structural function, the barrel vault survived the whole Middle Ages. Artistically treated barrel vaults can be found in single cases of two-nave and three-nave halls of townspeople’s Mazhouses in South Bohemia (Český Krumlov, Zlatá Koruna) and in gothic castles (e.g. Točnick, Švihov). From the Renaissance to the end of the 19th century, barrel vaults were commonly used for roofing both small and large spaces.

The restoration of historic buildings is frequently connected with reconstructions and rehabilitations of barrel vaults damaged mostly by the effects of induced deformations. In regions with the occurrence of natural seismicity, the failures of vaults are caused by their inelastic response to dynamic effects (Figure 1).

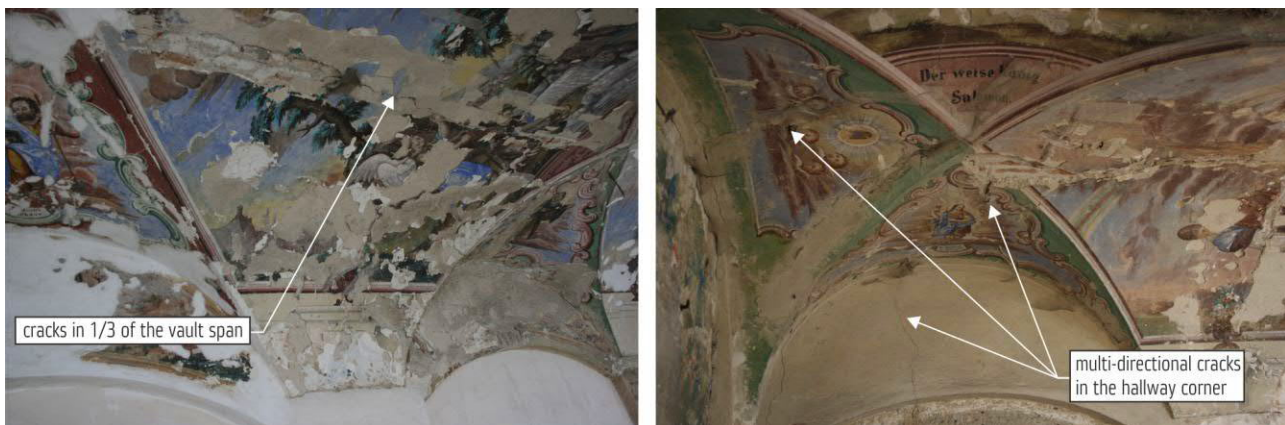


Fig. 1. - Vault in Loretto near Bor u Tachova

Vault failure mechanisms

The vaults failure mechanism arising by exceeding the ultimate strength (deformation) of vault masonry in tension differs from the failure mechanism of masonry pillars. The failure mechanism of vaults (curved masonry) is applied in cases where the thrust line describing the position of the origin of the internal compression force R in all vault cross sections (being the resultant curve of the loading acting on the vaults, vault supporting reactions and potential changes in vault embedding) does not pass through the inside third of the vault cross-section's height.

Vaulted structures are characterised by their high sensitivity to deformations of the supporting structure and, as a result, their response to dynamic effects causing displacements of the supporting structure (supporting system) can be the cause of an appearance of the mechanical failures or a complete failure of the vaulting system. Numerical analyses manifested high sensitivity of vaults to the deformation of the supporting structure (supports) where is, above all, the horizontal displacement (deformation) of the supports in low-order of magnitude values (mm) that can be the cause of the appearance of tensile stresses in corresponding vault sections and their successive failure due to tensile cracking. In this context, the deformations of the vault supporting structure induced by subsoil vibrations due to seismic effects may be extremely severe.

The vault failure process is very complex, including two significant mechanisms – changes in a shape, both local and of the whole vaulting system, and the vault masonry failure itself due to the action of tensile and compressive normal stresses reaching, in origins of tensile cracks where the plastic hinges appeared, ultimate values of masonry load bearing capacity in compression. The total vault failure (collapse) is, therefore, usually the result of two correlated parallel processes. It is characterised by the vault buckling together with its local failure, followed by mechanical masonry disintegration and the vault collapse. Both of the processes above are simultaneous and inseparable from each other. The vault stress state during its loading and its failure is accurately described by the thrust line pattern in individual phases of the vaulting system's action. The vault failure mechanism and reaching the vault ultimate load-bearing capacity is dramatically affected by the type of loading, particularly its potential asymmetry, its shape and geometric deflections and

imperfections and, last but not least, the stiffness and stability of the supports (Figure 2).



Fig. 2. - Vault collapse due to the supporting system's failure (horizontal displacement of supports)

The use of FRP materials in the reinforcement and stabilisation of historic, mostly masonry structures, brings numerous advantages, particularly in terms of their low weight, high effectiveness and potential reversibility [3]. The application of FRP materials in the area of historic and heritage buildings to-date has been primarily focused on the stabilisation of vertical load-bearing and vaulted structures to withstand the effects of horizontal loading induced by technical and natural seismicity [4,5].

The [NAKI I] project included extensive experimental research into the strengthening of masonry, stone, brick and mixed masonry pillars, walls and barrel vaults with composites based on high-strength, mainly carbon and glass, fibres and epoxy adhesives or polymer-modified cement mixes [7-13].

Experimental research into the response of barrel vaults to dynamic loading

Experimental research into segmented barrel vaults was performed on test pieces fabricated in a 1:1 scale – segmented masonry barrel vault sections 0.75 m in width, with a span of 3 m, with a rise of 0.75 m and a vault masonry thickness of 0.15 m, made of bricks of P15 quality and MVC 2 mortar (Table 1, Figure 3).

The objective of experimental research was the verification of the response and dynamic characteristics of segmented masonry barrel vaults exposed to repetitive static loading and dynamic loading in the horizontal and vertical direction. Nowadays, the dynamic response is very often used for the identification of potential damage to structures which need not be detectable by other means. The principle of such tests is the comparison of dynamic characteristics of structures exposed to low-level dynamic (i.e. non-destructive) excitation. The investigated characteristics are most often resonant frequencies and corresponding oscillation shapes. A change in frequency, most often its drop, may indicate the appearance of internal cracks in the tested specimen. A change in the oscillation shape, in turn, indicates its global failure.

Tab. 1. - Material characteristics of vault masonry

Vault	Mean compressive strength of bricks f_b [Mpa]	Mean compressive strength of mortar f_m [Mpa]	Mean tensile strength of mortar f [Mpa]
K 34 NZ	13.84	1.86	0.846
K 35 Z	12.18	1.16	0.586
K 36 Z	14.22	0.79	0.429

Legend:

Modulus of elasticity of bricks 2400-3600 MPa

Modulus of elasticity of mortar 400-500 MPa

Composite strips (Tyfo SCH 41 carbon fabric and Tyfo S epoxy resin) - modulus of elasticity 95800 MPa

tensile strength 986 MPa

maximum elongation 1%

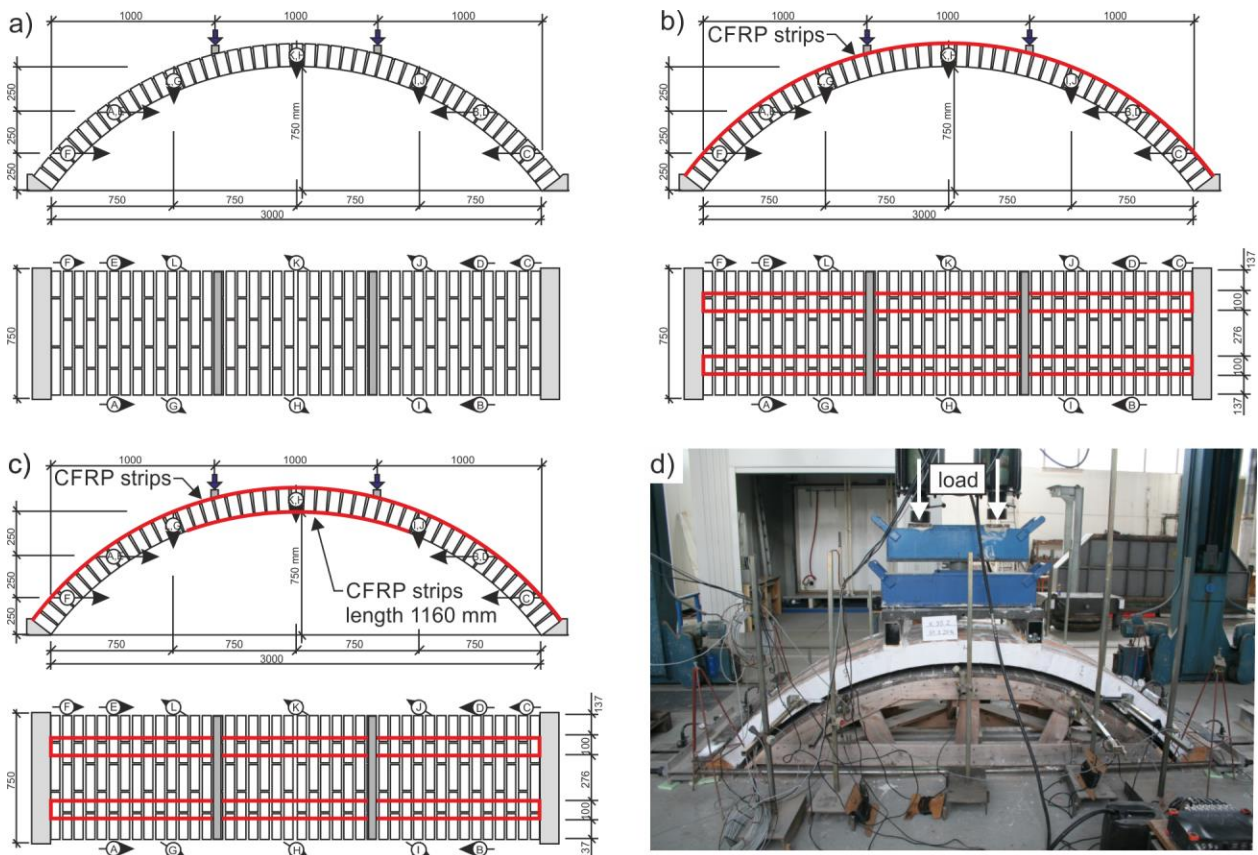


Fig. 3. - a) Scheme of vault K34 – non-reinforced, b) Scheme of vault K35 – reinforced at the extrados, c) Scheme of vault K36 – reinforced at the extrados and on the soffit, d) Test setup example

Experimental tests dealt with the verification of dynamic properties of masonry barrel vaults for the following cases:

- K34 – non-reinforced vault,
- K35 – reinforced vault, reinforcement at the extrados (upper surface) with 2 strips of the Tyfo SCH 41 carbon fabric glued with the Tyfo S epoxy resin. The strips

are 100 mm in width, the composite thickness for the calculation is 1 mm, the strips cover the whole length of the extrados. The strips (strip edges) are placed 137 mm from the vault edges.

- K36 – reinforced vault, reinforcement at the extrados (upper surface) and on the soffit (lower surface) always with 2 carbon fabric strips (see K35). The strips are 100 mm in width, the composite thickness for the calculation is 1 mm. The strips on the upper surface (extrados) again cover the whole length of the extrados, while the strips on the lower surface (soffit) are placed at the vault crown, the length of strips being 1180 mm. The strips (strip edges) are placed 137 mm from vault edges.

The experimental tests followed the procedure specified in Table 2.

Tab. 2. - Phases of dynamic and static tests of segmented barrel vaults

Phase	Tests
A – initial state	- Identification of dynamic characteristics – impact test - Performance of the static test (2x24 kN)
B – state after the first static test (2x24 kN)	- Identification of dynamic characteristics – impact test - Performance of the dynamic test in the vertical direction (Vault K34 – non-reinforced: 5Hz – 3000 oscillations; 25.96Hz – 15580 oscillations; 50Hz – 30000 oscillations, Vault K35 – reinforced at the extrados: 5Hz – 3000 oscillations; 18.44Hz – 11070 oscillations; 50Hz – 30000 oscillations, Vault K36 – reinforced at the extrados and on the soffit: 5Hz – 3000 oscillations; 19.59Hz – 6500 oscillations*)
C – state after the first dynamic loading in the vertical direction	- Identification of dynamic characteristics – impact test - Performance of the static test (2x24 kN)
D – state after the second static test (2x24 kN)	- Identification of dynamic characteristics – impact test - Performance of the dynamic test in the horizontal direction (Vault K34: 5Hz – 3000 oscillations; 20.08Hz – 12050 oscillations; 50Hz – 30000 oscillations, Vault K35 – reinforced at the extrados: 5Hz – 3000 oscillations; 24.08Hz – 14500 oscillations; 50Hz – 30000 oscillations)
E – state after the second dynamic loading in the horizontal direction	- Identification of dynamic characteristics – impact test - Performance of the static test (until failure)
F – state after the third static test (vault collapse)	

Legend: *failure of the loading device

Response of barrel vaults to static loading

The static loading of segmented barrel vaults was carried out with the help of two synchronised hydraulic actuators applying individual, monotonously rising steps of 2x 3kN. Partial results of the behaviour of barrel vaults symmetrically loaded in one third of their span with a pair of vertical forces (see Figure 3) are summarised in Table 3 and graphically displaced in Figures 4 and 5.

Tab. 3. - Experimentally identified deformation values and ultimate loading of segmented masonry barrel vaults

		K34 NZ (unreinforced)		K35 Z (CFRP, upper surface, full length)		K36 Z (CFRP, upper surface, full length, lower surface in length of 1160 mm)	
		$\delta_y^{1/2}$ [mm]	δ_x [mm]	$\delta_y^{1/2}$ [mm]	δ_x [mm]	$\delta_y^{1/2}$ [mm]	δ_x [mm]
1st static loading, load = 2 x 24 kN	$\delta_{TOT,1}$	1,43	-0,41	2,20	-0,26	1,19	0,36
	$\delta_{tot}/\delta_{TOT,1}$	100%	100%	100%	100%	100%	100%
2nd static loading, load = 2 x 24 kN	$\delta_{TOT,2}$	1,24	-0,21	1,66	-0,32		
	$\delta_{tot}/\delta_{TOT,1}$	87%	51%	75%	123%		
3rd static loading, load = 2 x 24 kN	$\delta_{TOT,3}$	1,23	-0,45	1,68	-0,21		
	$\delta_{tot}/\delta_{TOT,1}$	86%	110%	76%	81%		
3rd static loading, load-bearing capacity	$N_{u,m}$	2 x 67,7 kN (100%)		2 x 81,05 kN (120%)			
	δ_{MAX}	7,19	-3,08	16,01	-7,75		

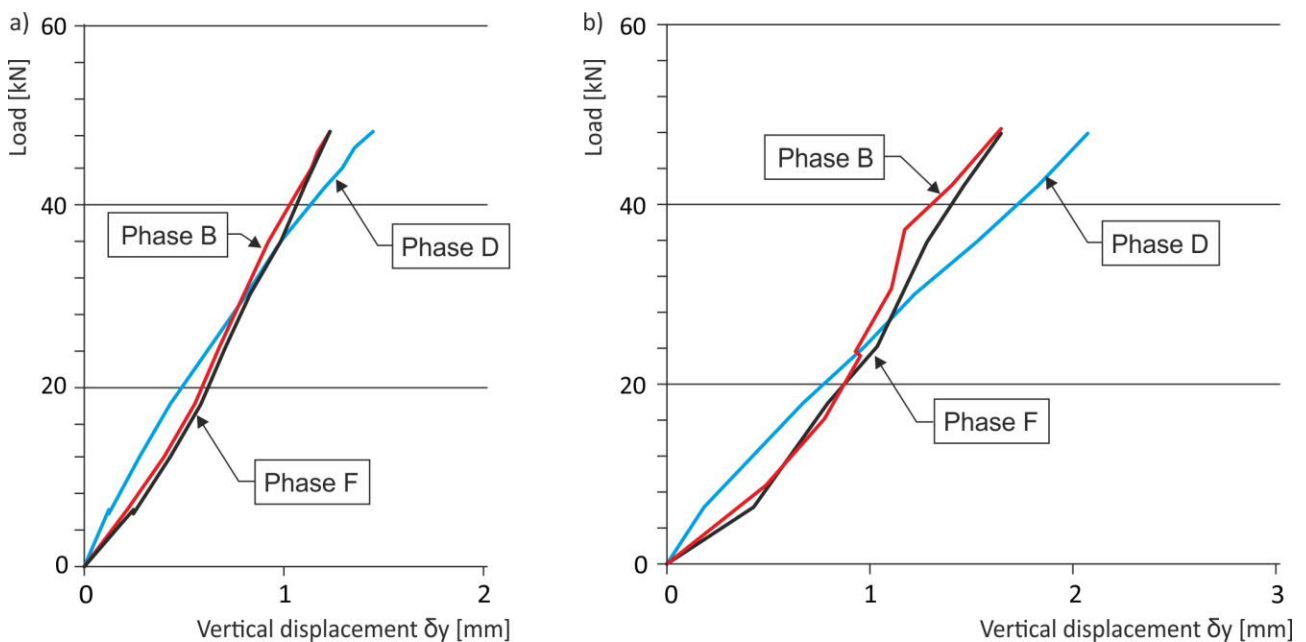


Fig. 4. - a) Pattern of vertical deformations $\delta_y \times L$ of a non-reinforced vault (K34) under static loading (2x24 kN) in individual loading phases, b) Pattern of vertical deformations $\delta_y \times L$ of a vault reinforced on the extrados (K35) under static loading (2x24 kN) in individual loading phases

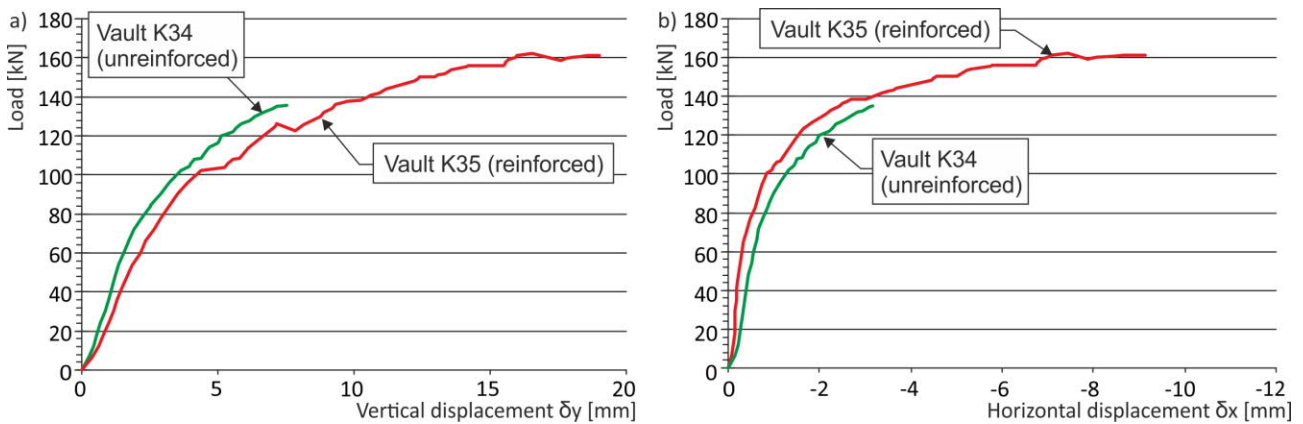


Fig. 5. - a) Overall working diagrams of vertical deformations $\delta y \times L$ of segmented barrel vaults under loading until failure, b) Overall working diagrams of horizontal deformations $\delta x \times L$ of segmented barrel vaults under loading until failure

The results of experimental values obtained from the investigation of the response of vaulted structures to static loading imply (comparison of vault deformation values from the second and third static phase – see Table 2) that the effect of dynamic loading results in the “stabilisation” (consolidation, “strengthening”) of the vaulted structure. We may presume that some portion of non-elastic deformations occurred during the first dynamic test (additional pushing of bed joints, stabilisation of the supporting system, etc.). These values can be experimentally measured (during dynamic loading) with difficulty. This issue will be the subject of further experimental verification.

Response of barrel vaults to dynamic loading

Dynamic loading in both the vertical and horizontal direction was applied with the TIRAvib electrodynamic exciter, type TV5550/LS with a weight of 550 kg. Its operating frequency range is from 0 up to 3 kHz and the maximum rated travel of mobile mass is 100 mm. The exciter was fixed to the vault and adapted to vertical and horizontal oscillations (Figure 6a). The vertical response was measured with five Wilcoxon accelerometers, model CMMS 793L, with an output sensitivity of 51 mV/ms^{-2} . One of them was positioned on the mobile part of the exciter to read the mass motion. Other sensors were positioned on the vault (Figure 6b).

Following each (partial) static loading, the vaults were exposed to dynamic loading. It was after the first static test in the vertical direction, after the second static test in the horizontal direction to verify the influence of dynamic effects on the gradual failure of a non-reinforced and reinforced vault (reduced stiffness) and to obtain findings about the effect of vault reinforcement with composites in terms of increased vault’s resistance to dynamic loading.

A total of 6 vault states were produced:

- A – initial undamaged state
- B – state after the first static test (including transition into non-linear state)
- C – state after the first dynamic loading in the vertical direction
- D – state after the second static test
- E – state after the second dynamic loading in the horizontal direction
- F – state after the third static test (until structure’s failure)

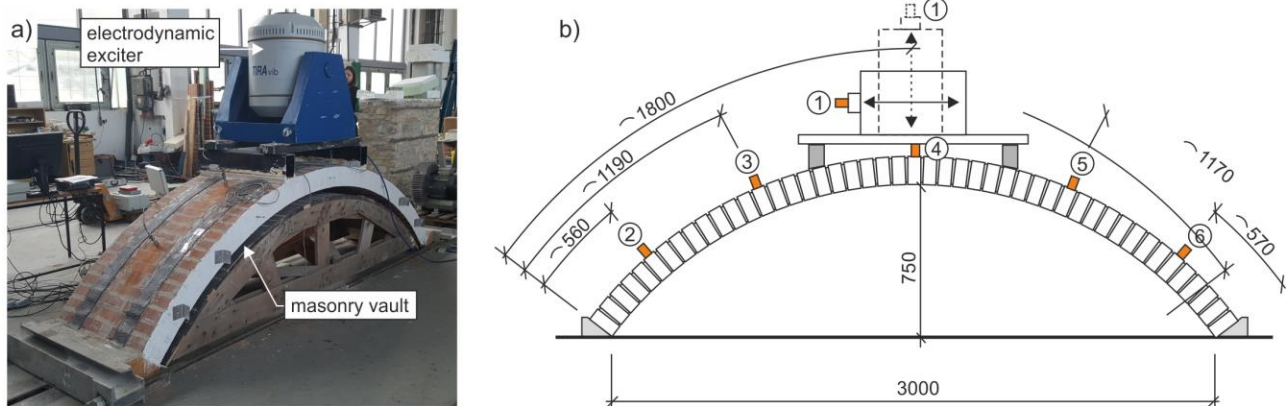


Fig. 6. - a) Mounting of the TIRAvib electrodynamic exciter on the vault, b) Distribution of sensors on the vault

Prior to each loading, the identification impact test had been performed and resonant frequencies were identified from it. The identification test had been performed with a hammer with a rubber head. The induced vault oscillations (its response) were transformed into frequency spectra from which frequency peaks were read.

Dynamic loading effects were performed both at the first resonant frequency (ca 18Hz) and outside resonant frequencies, namely at frequencies of 5Hz and 50 Hz, which characterise common external loading in buildings or traffic-induced dynamic loading.

Following each loading step, especially after static loading, there was a drop in the effective vault stiffness, which was manifested by a drop in the natural frequencies and, in some cases, by increased internal damping, most likely due to the appearance of microcracks over the whole vault cross section. Changes in stiffness and geometry after each loading step were manifested by the changes in the dynamic characteristics during the monitoring of changes in the vault's state. Frequencies were also detected on a numerical model (Figures 7 – 10) comparing theoretical and experimental oscillation shapes corresponding to the 1st to 6th natural frequencies. The obtained patterns show satisfactory agreement of theoretically and experimentally identified oscillation shapes. Successive harmonic loading occurred in the vicinity of such identified resonant frequencies with the objective of identifying also resonant oscillation shapes.

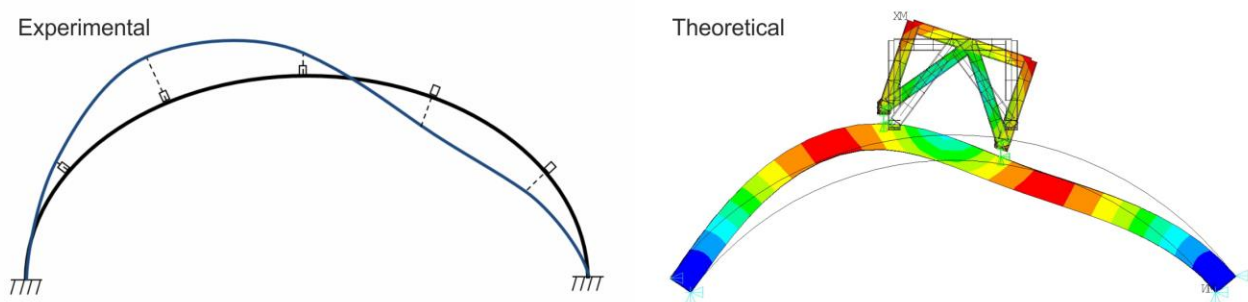


Fig. 7. - Oscillation shapes, theoretical and obtained from experiments, corresponding to the first natural frequency (see Tables 1 - 3)

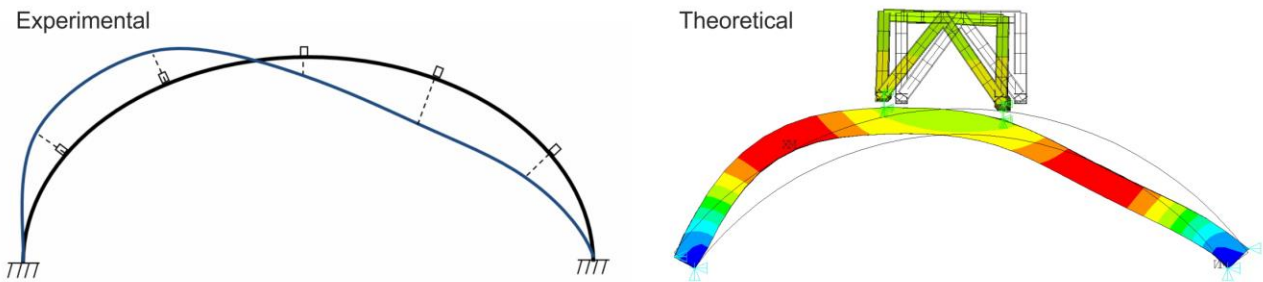


Fig. 8. - Oscillation shapes, theoretical and obtained from experiments, corresponding to the second natural frequency (see Tables 1- 3)

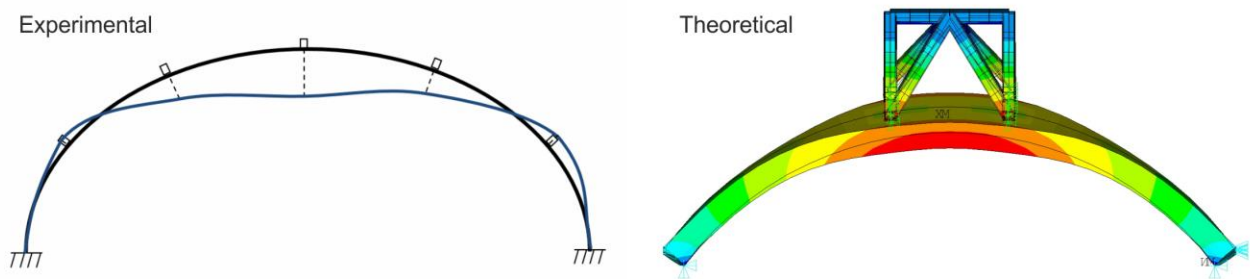


Fig. 9. - Oscillation shapes, theoretical and obtained from experiments, corresponding to the fifth natural frequency (see Tables 1 - 3)

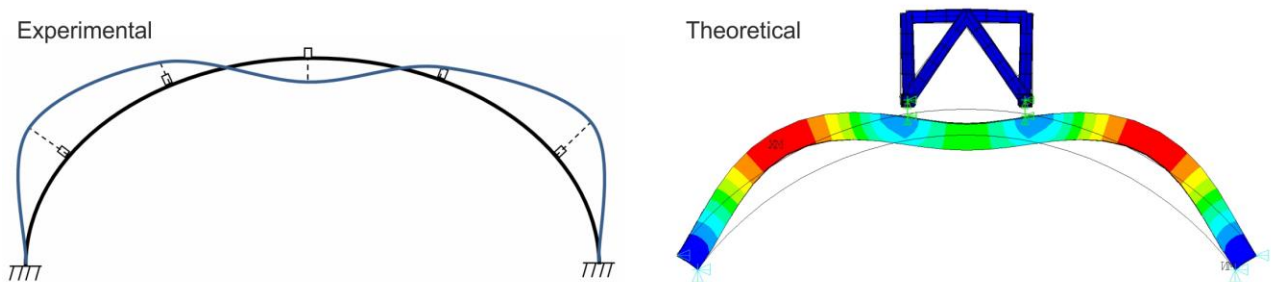


Fig. 10. - Oscillation shapes, theoretical and obtained from experiments, corresponding to the sixth natural frequency (see Tables 1 - 3)

Tables 4-6 present frequencies before loading (see Table 2) and after individual loading steps. As was assumed there is a visible drop in frequencies connected with the progressive damage of the vaulted structure. This is due to the decrease in its stiffness, which is evident mainly in non-reinforced vaulted structures. In the case of a reinforced vault, K35, there was a re-growth in frequencies detected after the second static test applying to all oscillation shapes – all frequency peaks. This is most likely caused by the cross-section's consolidation, i.e. the closing of cracks where the upper vault reinforcement probably plays a positive role. In the case of vault K34, this phenomenon is not so distinctive, the frequencies only rise in the first resonant shape, which is dominant, i.e. very important for the detection of damage.

Tab. 4. - Selected frequencies measured after different types of loading for vault K34_NZ

Loading	Frequencies [Hz]								
	1	2	3	4	5	6	7	8	9
Before loading	17.55	28.26	32.20	50.66	65.61	69.27	82.70	105.1	113.2
After 1 st static test	17.85	27.62	31.89	50.05	62.1	65.16	--	98.42	106.7
After 1 st static test + 1 st dyn. loading	13.58	27.62	32.2	--	--	--	--	93.99	--
After 2 nd static test	14.04	24.72	28.69	43.03	59.81	--	--	93.99	107.4
After 2 nd stat. test + 2 nd dyn. loading	14.04	24.72	28.69	41.45	--	66.53	73.85	92.47	107.1

Tab. 5. - Selected frequencies measured after different types of loading for vault K35_Z

Loading	Frequencies [Hz]								
	1	2	3	4	5	6	7	8	9
Before loading	19.23	29.75	33.26	47.76	56.3	66.53	72.63	105.1	110.3
After 1 st static test	14.42	23.19	29.68	41.35	50.58	63.4	72.25	103.8	107.0
After 1 st static test + 1 st dyn. loading	13.43	19.53	28.53	36.01	49.59	62.87	69.58	97.05	--
After 2 nd static test	15.87	24.72	29.91	--	50.96	62.87	74.16	97.6	103.8
After 2 nd stat. test + 2 nd dyn. loading	13.28	22.28	28.08	--	48.68	62.56	74.92	89.42	103.3

Tab. 6. - Selected frequencies measured after different types of loading for vault K36_Z

Loading	Frequencies [Hz]								
	1	2	3	4	5	6	7	8	9
Before loading	19.99	32.04	34.71	51.19	64.47	86.98	100.0	105.6	110.8
After 1 st static test	--	24.41	31.89	49.9	--	69.27	96.74	102.2	105.1

Legend: The test was interrupted for the reason of the electrodynamic exciter's failure.

CONCLUSION

Experimental results represent very important background material for numerical modelling during a repetitive validation of the computational model, but also a significant source of information for the selection of effective rehabilitation procedures for vaulted structures. The results are of major importance particularly for vaults of historic buildings situated in the seismically active



regions or in places with intensive technical and induced seismicity (mining, stone quarrying, traffic).

ACKNOWLEDGEMENTS

The article was written with support from the NAKI II DG16P02M055 project "Research and development of materials, processes and techniques for restoration, preservation and strengthening of historic masonry structures, surfaces and systems for preventive care of heritage buildings exposed to anthropogenic and natural risks" of the Ministry of Culture of the Czech Republic.

REFERENCES

- [1] M. Pimer, S. Urushadze. " Structural damage assessment using dynamic response, Acta technica , CSAV 47, 2002, pp. 445-466.
- [2] M. Pimer, S. Urushadze: Dynamic response as a tool for damage identification, Applied Mechanics, International research Journal, Timoshenko Institute of Mechanics, Kiev, Ukraine, ISSN 0032-8243, App. Mech., 2004, Vol. 40, N 5, 1-144, Editor: A.N. Guz, pp.3-29.
- [3] Bruggi, M., Milani, G., Taliercio, A., Design of the Optimal Fiber-Reinforcement for Masonry Structures via Topology Optimization, International Journal of Solids and Structures 2013, doi: <http://dx.doi.org/10.1016/j.ijsolstr.2013.03.007>
- [4] Luccioni B, Rougier VC, In-plane retrofitting of masonry panels with fibre reinforced composite materials, Construction and Building Materials 2011;25:1772–1788
- [5] Grande E, Imbimbo M, Sacco E, Finite element analysis of masonry panels strengthened with FRPs, Composites: Part B 2013;45:1296–1309
- [6] Výzkumný projekt Ministerstva kultury ČR NAKI DF12P01OVV037 "Progresivní neinvazivní metody stabilizace, konzervace a zpevnování historických konstrukcí a jejich částí kompozitními materiály na bázi vláken a nanovláken", vedoucí řešitel prof. Ing. Jiří Witzany, DrSc. dr.h.c.
- [7] Witzany, J., Zigler, R., Kroftová, K. Strengthening of compressed brick masonry walls with carbon composites (2016) Construction and Building Materials, 112, pp. 1066-1079. DOI: 10.1016/j.conbuildmat.2016.03.026
- [8] Witzany, J., Zigler, R. Stress state analysis and failure mechanisms of masonry columns reinforced with FRP under concentric compressive load (2016) Polymers, 8 (5), art. no. 176, . DOI: 10.3390/polym8050176
- [9] Witzany, J., Zigler, R. Failure mechanism of compressed reinforced and non-reinforced stone columns (2015) Materials and Structures/Materiaux et Constructions, 48 (5), pp. 1603-1613. DOI: 10.1617/s11527-014-0257-z
- [10] Witzany, J., Brožovský, J., Čejka, T., Kroftová, K., Kubát, J., Makovička, D., Zigler, R. The application of carbon composites in the rehabilitation of historic baroque vaults (2015) Polymers, 7 (12), pp. 2670-2689. DOI: 10.3390/polym7121540
- [11] Witzany, J., Čejka, T., Zigler, R. Failure mechanism of compressed short brick masonry columns

confined with FRP strips, (2014) Construction and Building Materials, 63, pp. 180-188.
DOI: 10.1016/j.conbuildmat.2014.04.041

[12] Witzany, J., Zigler, R. The analysis of the effect of strengthening compressed masonry columns with carbon fabric (2014) Proceedings of the 7th International Conference on FRP Composites in Civil Engineering, CICE 2014.

[13] Witzany, J. - Čejka, T. - Zigler, R.: Experimental research on strengthening of masonry vaults using FRP. In FRP Composites in Civil Engineering. Duebendorf, Švýcarsko: EMPA, 2008, p. 149. ISBN 978-3-905594-50-8.